DESIGN AND SIMULATION OF NOVEL ARRAYED WAVEGUIDE GRATING BY USING THE METHOD OF IRREGULARLY SAMPLED ZERO CROSSINGS

A Thesis

Submitted to the Faculty

of

Purdue University

by

Sai Hu

In Partial Fulfillment of the

Requirements for the Degree

of

Master of Science in Electrical and Computer Engineering

December 2002

TABLE OF CONTENTS

Page

LIST OF TABLES iv

LIST OF FIGURES v

ABSTRACT viii

1. CONVENTIONAL ARRAYED WAVEGUIDE GRATING DEVICE 1
    1.1 Introduction 1
    1.2 Materials and Fabrications 4
    1.3 Operations and Properties 5
2. METHOD OF IRREGULARLY-SAMPLED ZERO-CROSSINGS 23
    2.1 One-Image-Only Digital Holography 23
    2.2 Virtual Model 24
    2.3 Algorithm of Irregularly-Sampled Zero-Crossings 28
    2.4 Discussion of Irregular Sampling 29
3. SIMULATIONS AND DISCUSSION 35
    3.1 Simulation Techniques 35
    3.2 Results and Discussion 35
4. DESIGN AND SIMULATION OF R-AWG IN *BEAMPROP* 55
    4.1 Design Method for R-AWG 55
    4.2 Simulation Techniques and Results 61
5. ANALYSIS AND APPLICATION IN THREE-DIMENSIONAL GEOMETRY... 75
    5.1 Dispersion Relations 75
    5.2 Method of Irregularly-Sampled Zero-Crossings Method in 3D 78
    5.3 Simulation Results 79
6. SUMMARY AND FUTURE RESEARCH 87

Page
LIST OF REFERENCES.. 89

APPENDICES

APPENDIX A.. 93
APPENDIX B.. 96

LIST OF TABLES

Table Page

Table 1.1. Periodical frequency assignments for N×N operation of AWG (from [27])....9

Table 1.2. Experimental Performance of Fabricated Demultiplexers (from [12])..........11

Table 1.3. Comparison of different causes of path-length errors (from [40])...............13

Table 3.1. Crosstalk Deviation due to Path Length Error....................................38

LIST OF FIGURES

Figure Page

Fig. 1.1. Optical WDM system configurations (modified from [6])........................15

Fig 1.2. Fabrication process of silica-based planar lightwave circuits........................16

Fig 1.3. Typical InP based waveguide structures..17

Fig. 1.4. Schematic configuration of AWG demultiplexer....................................18

Fig. 1.5. Enlarged view of the second slab region..19

Fig. 1.6. An experimental result of transmission spectrum (from [12])....................20

Fig.1.7. Approximation graphs of field distribution on the image plane for four wavelengths and the corresponding transmission spectrum, in which central insertion loss, nonuniformity and FSR are shown (from [29])........................21

Fig. 2.1. The 2D schematic diagram for the virtual model....................................33

Fig. 2.2. Part of output star coupler and the image plane......................................34

Fig. 3.1. Total field distribution on the X-Z plane (m=129)..................................39

Fig. 3.2. Normalized field intensity on the image plane (X-Y plane at $z=z_o$, x is variant, y is constant, m=129)...40

Fig. 3.3. Arrayed waveguide distribution (m=129)...41

Fig. 3.4. Transmission spectrum (wavelength response), m=129...........................42

Fig. 3.5. Dispersion relation (a) Δx vs. $\Delta\lambda$ (m=129) and (b) Δx vs. δ ($\propto m$)................43

Fig. 3.6. Combination of Fig. 3.1 and 3.2, same parameters used...........................44

Fig. 3.7. RandX=0.5 (other parameters are same as those used in Fig. 3.6)................45

Fig. 3.8. RandX=0.25 (other parameters are same as those used in Fig. 3.6)..............46

Fig. 3.9. RandX=0 (other parameters are same as those used in Fig. 3.6)..................47

Figure Page

Fig. 3.10. M=200, DX=10μm, m=64.5 (other parameters are same as those used in Fig. 3.6)........48

Fig. 3.11. M=50, DX=40μm, m=258 (other parameters are same as those used in Fig. 3.6)........49

Fig. 3.12. M=200, Max_X=4mm, m=129 (other parameters are same as those used in Fig. 3.6)........50

Fig. 3.13. M=50, Max_X=1mm, m=129 (other parameters are same as those used in Fig. 3.6)........51

Fig. 3.14. Transmission spectrum for 32 channels with 0.8nm spacing (m=64.5)........52

Fig. 3.15. Transmission spectrum for 64 channels with 0.4nm spacing (m=64.5)........53

Fig. 3.16. Transmission spectrum for 128 channels with 0.2nm spacing (m=64.5)........54

Fig. 4.1. Rowland Circle Geometry........64

Fig 4.2. Examples of Layout Methods for Array Waveguides........65

Fig. 4.3. Layouts for Arrayed Waveguides........66

Fig. 4.4. Array Design for Full Layout........67

Fig. 4.5. Array Design for Full Layout........68

Fig. 4.6. Equivalent phase transfer from virtual model to real structure........69

Fig. 4.7. Layout design for 64-channel regular AWG (m=40) Input star coupler, arrayed waveguides, output star coupler........70

Fig. 4.8. Layout design for 64-channel random AWG (m=40) Input star coupler, arrayed waveguides, output star coupler........71

Fig 4.9. Simulation result for the regular AWG in Fig. 4.7 (m=40)........72

Fig 4.10. Simulation result for the random AWG in Fig. 4.8 (m=40)........73

Fig 5.1. 3D model image plane: dispersion in x-direction (exact phase method, m_x=64.5, m_y=0)........80

Fig 5.2. 3D model image plane: dispersion in y-direction (exact phase method, m_x=0, m_y=64.5)........81

Fig 5.3. 3D model image plane: dispersion in both directions (exact phase method, m_x=64.5, m_y=32.25)........82

Figure Page

Fig 5.4. 3D model image plane: dispersion in x-directions (4 quantization levels, m_x=64.5, m_y=0)........83

Fig 5.5. 3D model image plane: dispersion in x-directions (16 quantization levels, m_x=64.5, m_y=0)........84

Fig 5.6. 3D model image plane: dispersion in x-directions (256 quantization levels, m_x=64.5, m_y=0)........85

Appendix Figure Page

Fig. A.1. A truncated circular core fiber........99

Fig. A.2. Waves incident normally upon a truncated fiber........99

ABSTRACT

Hu, Sai. M.S.E.C.E., Purdue University, December 2002. Design and Simulation of Novel Arrayed Waveguide Grating by Using the Method of Irregularly Sampled Zero Crossings. Major Professor: Okan K. Ersoy

Arrayed waveguide grating (AWG) is playing an increasingly important role in dense wavelength division multiplexing (DWDM) system. The regular AWG device consists of an arrayed waveguide region where all the individual waveguides are equally spaced on the Rowland circle and the adjacent ones have constant length difference. The regularity of their positions and lengths leads to the phenomenon that a portion of the Rowland circle is occupied by the adjacent (undesired) order focused beams of the operation wavelength channels. The repetitions of the same wavelengths at different locations affect the device potential capacity.

The method of irregularly sampled zero-crossings is discussed in a virtual model first and then extended into the arrayed waveguide grating application. It has proven to be able to solve the abovementioned problem of regular AWG by reducing the undesired order focused beams with only the desired ones left. Therefore, those places on the image plane occupied and useless before are freed now for accommodating new wavelength channels. By employing the BeamPROP software, we implement the layout design and BPM simulation for the new device based on this method. It is shown that the new device can significantly increase the channel capacity compared to the regular device provided similar structural parameters. The random characteristic of such structure also results in better phase error tolerance. The main tradeoff lies in the degraded noise performance. However, the crosstalk between adjacent channels can be reduced by increasing the channel spacing since the limitation due to free spectral range is removed.

1. CONVENTIONAL ARRAYED WAVEGUIDE GRATING DEVICE

1.1 Introduction

The fast and global spread of Internet and multimedia communications is accelerating the growth of optical communication networks. Research and commercial interests in optical networks based on wavelength division multiplexing (WDM) systems are rapidly increasing [1]-[4]. WDM provides a new dimension for solving capacity and flexibility problems in the telecommunication network. It offers a huge transmission capacity and allows for novel network architectures that are more flexible than traditional networks. Typical optical network started from point-to-point WDM transmission systems, and now is evolving to the ring architecture [5], which is schematically shown in Fig. 1.1[6].

Various optical devices and components have been developed to realize WDM-based optical networks, and some of them have already been installed in the commercial communication system. Among them, key components are the wavelength multiplexer and demultiplexer, which work to combine and separate various frequency channels. Many principles have been proposed and reported for realization of multiplexers and demultiplexers. It is worth mentioning that multiplexing and demultiplexing are essentially the same except the direction of lightwave propagation. More discussion is usually focused on demultiplexing, which can be also applied to multiplexing due to the reciprocity of lightwave beam propagation. In the following, several major types of demultiplexers will be described.

The thin-film interference filter is composed of more than two Fabry-Perot (F-P) cavities separated by dielectric layers, and each cavity contains a multi-layer structure with more than 50 layers [7]. Thin-film filters with different wavelengths are cascaded in series for demultiplexing. Each WDM signal passing through one filter is received by an output fiber with a focusing lens. The number of desired WDM channels determines the number of filters and lens as needed in the demultiplexing system.

The phenomenon known as photosensitivity [8] has been used to fabricate fiber Bragg gratings (FBG) [9] and long-period gratings (LPG) [10]. The FBG can be combined either with a directional coupler according to the Mach-Zehnder interferometer structure, or with a circulator to form a functional unit that splits one wavelength signal from others. Furthermore, the demultiplexer can be constructed by cascading the functional units. Again, the number of such units is dependent on the number of the WDM channels [11].

The MZ interferometer configuration can also be realized in planar lightwave circuits (PLCs). PLCs are waveguide devices that integrate fiber-matched optical waveguides on silicon or glass substrate to provide an efficient means of interaction for the guided-wave optical signals [12]. In [18], a 10GHz-spaced 1×16 demultiplexer is constructed by combining one, two, four, eight asymmetric MZ interferometers in series, with respective frequency spacings of 10, 20, 40, 80G Hz.

The three types of demultiplexers described above have similar problems. Several demultiplexing stages need to be cascaded, thus, the insertion loss is accumulated at each stage. It is rather difficult to reduce the wavelength spacing and increase the port count, which cannot meet the demands for a large number of channels.

Since early 1990, research interests are increasingly focused on the monolithic integrated wavelength demultiplexers. Two main types of monolithic integrated wavelength demultiplexers are distinguished, namely, reflection grating spectrometer devices and arrayed waveguide gratings. Both are imaging devices, i.e., they image the field of an input waveguide consisting of multiple wavelength signals onto an array of output waveguides, respectively.

The grating-based demultiplexers have been demonstrated in SiO_2/Si [19], InGaAs/AlGaAs/GaAs [20], and InGaAsP/InP [21][22]. In grating-based demultiplexers, a vertically etched reflection grating provides the dispersive and focusing properties required for demultiplexing. They are usually operated at low order, offering typically more than 50nm free spectral range (FSR) for the demultiplexing of a large number of wavelength channels [23][24]. However, the losses depend critically on the quality of the vertically etched reflection grating mirror. Chemically-assisted ion beam etching (CAIBE) or reactive ion etching (RIE) are usually employed to achieve the verticality and smoothness of the deeply etched grating facets.

More recently, demultiplexers based on PLC-type arrayed waveguide gratings (AWG) have been extensively investigated. This is due to the fact that they are compatible with conventional waveguide technology, suitable for large-scale integration, more fabrication tolerant and better for mass production. They are usually operated at higher orders with smaller free spectral range compared to the grating-based demultiplexers. The array waveguide grating (AWG), which is also called phased array (PHASAR) or waveguide grating router (WGR), was proposed in 1988 by Smit [13]. Then, Vellekoop and Smit reported the first devices operating at short wavelengths such as 632nm[14][15]. The first devices operating at long wavelengths (1300nm and 1550nm bands) were reported by Takahashi in 1990 [16][17]. Dragone extended the concept of phased array from 1×N to N×N devices [25][26], which offers more freedom and capacity in multiwavelength network applications [12][27][29].

AWG is the main topic of this thesis. In the remaining part of this chapter, the principles, properties and related issues of conventional AWG are discussed. Our proposed device, irregular-sampling zero-crossing arrayed waveguide grating (ISZC-AWG) is described in Chapter 2 by introducing our irregular-sampling zero-crossing (ISZC) method and analyzing the corresponding model. Theoretical analysis and simulation results are given in Chapter 3. In Chapter 4, the algorithm is realized in terms of the waveguide layout design and the beam propagation method (BPM) simulation via BeamPROP, a research and development software from Rsoft Inc. Then the problems related to device performance are investigated. Chapter 5 covers topics involving extension of our method from 2-dimension to 3-dimension and future research proposals are discussed in Chapter 6. Part of the work is done in close collaboration with Ying Lu.

1.2 Materials and Fabrications

Devices reported so far can be divided into two main types: silica-based devices and InP-based devices. Silica-based optical waveguides are fabricated on silicon or silica substrate by a combination of flame hydrolysis deposition (FHD) and reactive ion etching (RIE) [28]. The waveguide fabrication process is shown schematically in Fig. 1.2. The first step is to use FHD to deposit two successive glass particle layers that serve as the under-cladding and the core of the waveguide. After deposition, the wafer with these two porous glass layers is heated to high temperature for consolidation. The waveguide core ridges are then formed by photolithography and RIE according to designed circuit pattern. Finally the core ridges are covered with over-cladding layer and consolidated again. This type of waveguide structure has low index contrast, which is also called fiber-matched. The advantages include low propagation loss and high coupling efficiency to optical fiber. However, low index contrast requires large bending radii of the fiber-matched waveguides. Consequently, the silica-based devices have relatively large dimensions, which make them less suitable for large-scale integration. Moreover, the passive character of silica limits its potential of integration with active components.

In contrast, the InP-based devices have their main advantages including the potential of monolithic integration of active components, such as semiconductor lasers, detectors, amplifiers, modulators and switches, and the potential to integrate a large number of components on a single chip due to the relatively smaller bending radii available for the layout. The integration enables us to obtain compact device with high functionality. The buried waveguide structure and rib waveguide structure were investigated. While recently the air-cladding raised-stripe (deep ridge) waveguide structure is getting more attention (refer to Fig. 1.3). The fabrication processes for semiconductor AWG include molecular beam epitaxy (MBE) [30][31] or metal-organic chemical vapor deposition (MOCVD) [32][33], combined with various lithography and etching methods. However, such type of high index structure suffers from the higher propagation losses, higher fiber-coupling losses and higher sensitivity to polarization modes. Up to now the best performance of AWG is still achieved by means of the mature Silicon-based technology.

1.3 Operations and Properties

This section explains the theory of regular AWG in detail, especially the demultiplexing properties and the frequency (wavelength) relation between input and output ports. Those important parameters related to device performance, such as free spectral range (FSR), spectral transmission response, on-chip loss, and channel crosstalk are also briefly discussed.

1.3.1 Waveguide layout and basic principles

Fig. 1.4 shows a schematic waveguide layout of the N×N AWG. It consists of N input waveguides, N output waveguides, two focusing slab regions that are also called free propagation region (FPR), and an array of waveguide gratings that is made of M uncoupled waveguides. All of them are integrated on the same substrate. The locations of the I-O waveguides and the arrayed waveguides are usually based on the Rowland circle construction as used in concave reflection gratings.

The operation of the device can be explained as follows [29]. When the beam propagation through the input waveguides enters the slab region, it is no longer laterally confined and becomes divergent. On arriving at the input end of the waveguide array, the beam is coupled into the arrayed waveguides and then propagates through individual arrayed waveguides to the output aperture. The lengths of the waveguides are chosen to make sure that the optical path length difference between adjacent waveguides equals an integer multiple of the center wavelength of the demultiplexer. For this center wavelength, the fields in individual waveguides will get to the output aperture with equal phase (an integer multiple of 2π is neglected). Therefore the field distribution at the input end is reproduced at the output end. The divergent beam is thus transformed into a convergent beam with equal field and phase distribution, and the image of input field at the object plane will be formed at the image plane. In other words, the combination of the arrayed waveguides and the two slab waveguides construct a 1:1 imaging system. The dispersion of the AWG is due to the linearly increasing lengths of the arrayed waveguides, which cause linear phase changes induced by a small change of the wavelength. As a consequence, the outgoing beam is tilted and the focal point shifts along the image plane. Accordingly, the light field (of some frequency) at the entrance of one input waveguide is transferred to the appropriate output waveguide with little deformation. The theoretical derivation is given in the next subsection.

Furthermore, each arrayed waveguide is directed perpendicular to the center of the input and output waveguide curvatures, respectively, at its two ends. The apertures at either end are also widened (with a taper structure) to reduce the slab-channel coupling loss. There should be a sufficient number of arrayed waveguides so that more of the light beam diffracted in the slab region can be collected.

1.3.2 Focusing and dispersion

Before going deep into the derivation details, I would give a brief explanation of the parameters and notations used throughout this thesis. The constant path length difference between neighboring waveguides is ΔL, which is related to the diffraction order of the grating m. In the input slab region, D_1 is the input waveguide spacing, d_1 is the spacing of the arrayed waveguide at the input end that follows a curvature with a radius of f_1, and the distance measured in clockwise direction from the center input is x_1, which corresponds to an angular distance θ_1. In the output slab region, D is the output waveguide spacing, d is the spacing of the arrayed waveguide at the output end that follows a curvature with a radius of f, and the distance measured in clockwise direction from the center output is x, which corresponds to an angular distance θ. Fig. 1.5 gives an enlarged view of the second slab region. The index numbers for the input, output, and arrayed waveguides are represented by i, j, k, respectively. Route (i, j) means from i-th input waveguide to j-th output waveguide. Most of the notations and derivations used here refer to [12].

Considering the beam passing through the k-th and (k-1)th arrayed waveguides, the grating equation is given by Eq. (1.1), based on the phase matching conditions:

$$\begin{aligned}\beta_s(\lambda_0)(f_1 - d_1 \sin\theta_1) + \beta_c(\lambda_0)[L_c + (k-1)\Delta L] + \beta_s(\lambda_0)(f + d\sin\theta) = \\ \beta_s(\lambda_0)(f_1 + d_1\sin\theta_1) + \beta_c(\lambda_0)[L_c + k\Delta L] + \beta_s(\lambda_0)(f - d\sin\theta) - 2m\pi\end{aligned} \qquad (1.1)$$

In the above equation, β_s and β_c donate the propagation constants in slab region and array waveguide, λ_0 is the center wavelength, and L_c is the minimum array waveguide length. Subtracting common terms, we obtain Eq.(1.2):

$$\beta_s(\lambda_0)d_1\sin\theta_1 + \beta_c(\lambda_0)\Delta L - \beta_s(\lambda_0)d\sin\theta = 2m\pi \qquad (1.2)$$

From the definitions, the following equations are obvious:

$$\theta_1 = x_1 / f_1 = i \bullet \Delta x_1 / f_1 \qquad \theta = x / f = j \bullet \Delta x / f \tag{1.3}$$

Substituting Eq. (1.3) into Eq. (1.2), we get:

$$\beta_s(\lambda_0)\frac{d_1 x_1}{f_1} + \beta_c(\lambda_0)\Delta L - \beta_s(\lambda_0)\frac{dx}{f} = 2m\pi \tag{1.4}$$

Under the condition of $\beta_c(\lambda_0)\Delta L = 2m\pi$ (1.5)

Or $\lambda_0 = \frac{n_c \Delta L}{m}$ (1.6)

where n_c is the effective refractive index of the arrayed waveguide ($n_c=\beta_c/k$, k is the wave number in free space), the light input position x_1 and output position x satisfy the following equation:

$$\frac{d_1 x_1}{f_1} = \frac{dx}{f} \tag{1.7}$$

The dispersion of the output focal position x with respect to the wavelength for the fixed input position x_1 is obtained by differentiating Eq. (1.4) with respect to wavelength λ as

$$\frac{\Delta x}{\Delta \lambda} = \frac{n_g f \Delta L}{n_s d \lambda_0} \tag{1.8}$$

where n_s is the effective index of the slab waveguide, n_g is the group index of the effective index n_c of the arrayed waveguide ($n_g = n_c - \lambda dn_c/d\lambda$). Similarly, the dispersion of the input position x_1 with respect to the wavelength for the fixed output position x is obtained by differentiating Eq. (1.4) with respect to wave length λ as

$$\frac{\Delta x_1}{\Delta \lambda} = \frac{n_g f_1 \Delta L}{n_s d_1 \lambda_0} \tag{1.9}$$

When Δλ is set to the wavelength channel spacing, the Δx and Δx_1 should be the output and input waveguide separations D and D_1, respectively. Generally the input slab and output slab are identical, that is, D_1=D, d_1=d, f_1=f. Then we get:

$$\Delta L = \frac{n_s d D \lambda_0}{n_g f \Delta \lambda} \tag{1.10}$$

The angular dispersion, which is the relation between diffraction angle θ and frequency f can be also obtained by combining Eq. (1.3) and (1.10):

$$\frac{d\theta}{df} = -\frac{m\lambda_0^2 n_g}{n_s d c n_c} \qquad (1.11)$$

The spatial separation of the m-th and (m+1)-th order focused beams for the same wavelength is obtained from Eq. (1.2) as

$$X_{FSR} = \frac{\lambda_0 f}{n_s d} \qquad (1.12)$$

X_{FSR} is the free spatial range of the AWG. Number of available wavelength channels M is thus determined by dividing X_{FSR} with the output waveguide separation D as

$$M = \frac{X_{FSR}}{D} = \frac{\lambda_0 f}{n_s d D} \qquad (1.13)$$

1.3.3 Periodical assignment and free spectral range

The analysis in subsection 1.3.2 is focused on the 1×N properties of AWG, which could be extended to N×N operation. From Eq. (1.2),(1.3),(1.5),(1.6), it is shown that the center wavelength λ_0 is actually the pass wavelength for the route (i, j)=(0, 0), which is from the center input port to the center output port. It is well known that only N frequencies are logically required for the N×N connection. In such case, the periodicity of the AWG must be utilized by making sure each route has periodical pass frequencies, the spacing of which is referred to as the free spectral range (FSR). The FSR should be equal to N×Δf in order to complete the period of pass frequencies. The periodical frequency assignment is illustrated in Table 1.1.

Eq. (1.2) can also be written in another form as Eq. (1.14):

$$n_s d_1 \sin\theta_1 + n_c \Delta L + n_s d \sin\theta = m\frac{c}{f} \qquad (1.14)$$

For the order of m+1, Eq. (1.14) is changed into Eq. (1.15) below:

$$(n_s + \Delta n_s) d_1 \sin\theta_1 + (n_c + \Delta n_c)\Delta L + (n_s + \Delta n_s) d \sin\theta = (m+1)\frac{c}{f + FSR} \qquad (1.15)$$

where $n_s+\Delta n_s$ and $n_c+\Delta n_c$ are the effective indices of the slab and channel waveguides, respectively, at the frequency of f+FSR. The index change is approximated by:

$$\Delta n_c = \frac{dn_c}{df} FSR = -\frac{c}{f^2}\frac{dn_c}{d\lambda} FSR \qquad (1.16a)$$

$$\Delta n_s = \frac{dn_s}{df} FSR = -\frac{c}{f^2}\frac{dn_s}{d\lambda} FSR \tag{1.16b}$$

From Eq. (1.14)(1.15)(1.16), the FSR is given as

$$FSR = \frac{c}{(n_c - \lambda \frac{dn_c}{d\lambda})\Delta L + (n_s - \lambda \frac{dn_s}{d\lambda})(d_1 \sin\theta_1 + d\sin\theta)} \tag{1.17}$$

It is apparent that different input-output route has different FSR.

Table 1.1
Periodical frequency assignments for N×N operation of AWG
Column: Input; Row: Output (from [27])

	-8	-7	…	-1	0	1	…	6	7
-8	f_0	f_1	…	f_7	f_8	f_7	…	f_2	f_1
-7	f_{-1}	f_2	…	f_8	f_7	f_6	…	f_1	f_0
:	:	:		:	:	:		:	:
-1	f_7	f_8	…	f_2	f_1	f_0	…	f_5	f_6
0	f_8	f_7	…	f_1	f_0	f_1	…	f_6	f_7
1	f_7	f_6	…	f_0	f_1	f_2	…	f_7	f_8
:	:	:		:	:	:		:	:
6	f_2	f_1	…	f_5	f_6	f_7	…	f_4	f_3
7	f_1	f_0	…	f_6	f_7	f_8	…	f_3	f_2

1.3.4 Frequency response

Frequency response of the transmission coefficient of a demultiplexer is a very important factor in determining its application feasibility. Take the 1×N case for example, the light of each operation wavelength is diffracted in the input slab, coupled into the arrayed waveguides and passed through them, focused in the output slab, and coupled into one certain output waveguide. The focal point where the corresponding output waveguide is located is dependent on the optical frequency. If light with a wavelength other than the operation wavelengths comes in, it also gets focused also on the image plane of the output slab. There is, however, no output waveguide at its focal point to couple it out. It thus cannot travel through the AWG. Each route has its own frequency response. In the literature, the transmission spectrum is usually shown by simultaneously displaying the frequency response of N routes, which are from the center input waveguide to N different output waveguides. An example of experimental result is shown in Fig. 1.6. For the convenience of discussion, the approximation graphs of field distribution on the image plane for four different wavelengths and the transmission spectrum are schematically shown in Fig. 1.7.

The far-field envelope is a Gaussian profile, which can be explained as follows. The excited electric field amplitude in each array waveguide is ϕ_{1k} (k=1..M, M is the number of arrayed waveguide). The amplitude profile for the ϕ_{1k}'s is usually a Gaussian distribution (please refer to Appendix A). After the propagation through arrayed waveguides, the amplitude profile of the field out of array into the output slab ϕ_k is also approximated as a Gaussian distribution. The field profile $\Phi(x)$ at the output plane of AWG is the summation of the far-field patterns of ϕ_k's. That is, $\Phi(x)$ is the summation of the spatial Fourier transform of ϕ_k's. Summation and Fourier transform can be exchanged in order in a linear system. Therefore $\Phi(x)$ is the spatial Fourier transform of the entire field profile at the array-slab interface (the summation of ϕ_k's). Since the Fourier transform of a Gaussian distribution is also a Gaussian distribution, it can be concluded that the far-field intensity follows a Gaussian distribution given as Eq. (1.18):

$$I(\theta) = I_0 e^{-2\theta^2/\theta_0^2} \tag{1.18}$$

where θ_0 is the width of the equivalent Gaussian far field:

$$\theta_0 = \frac{\lambda}{n_s}\frac{1}{w_e\sqrt{2\pi}} \tag{1.19}$$

w_e being the effective width of the modal field of the arrayed waveguide. The derivation for Eq. (1.19) is given in Appendix A. In [25] and [38], a similar frequency response is obtained by using numerical simulations. The calculation is based on the summation of complex exponential terms (with amplitude and phase), which is essentially the same as the analysis above.

Based on Eq. (1.18) and (1.19), some simple analytical equations for estimating insertion loss L_0, channel nonuniformity L_u and bandwidth B can be derived [29]. Here the derivation details are not included, while their definitions are schematically shown in Fig. 1.7, and their typical values in several fabricated Silicon-based AWG's are listed in Table 1.2. Those parameters are especially important to device performance. In the rest of this chapter, we will discuss them in more detail.

Table 1.2
Experimental Performance of Fabricated Demultiplexers
( )...Designed Values by Beam Propagation Method (from [12])

Parameters	Experimental and Theoretical Results				
Number of Channels N	8	16	32	64	128
Center Wavelength λ_0 (designed value) in μm	1.299 (1.30)	1.5521 (1.552)	1.5498 (1.550)	1.5496 (1.550)	1.5494 (1.550)
Channel spacing $\Delta\lambda$ in nm	50	2	0.8 (100 GHz)	0.4 (50 GHz)	0.2 (25 GHz)
Path difference ΔL in μm	2.8	50.3	63	63	63
Slab Arc Length f in mm	3.58	5.68	11.35	24.2	36.3
Diffraction Order m	3	47	59	59	59
Number of Arrayed-Waveguides M	28	60	100	160	388
On-chip Loss for λ_0 in dB	2.2	2.3	2.1	3.1	3.5
3-dB Bandwidth (BPM simulation) in nm	27.4 (28.6)	0.74 (0.75)	40 GHz (37 GHz)	19 GHz (21 GHz)	11 GHz (9.5 GHz)
Channel Crosstalk in dB	<-26	<-29	<-28	<-27	<-16

1.3.5 Insertion Loss

Naturally, low fiber-to-fiber insertion losses are preferred. Typically the commercially available devices guarantee loss below 7dB between the center and outer ports. For peaked Gaussian passbands between center ports, this loss may decrease to 4.5dB. Research groups have reported losses that range from 2.3 to 2.7 dB. Several sources of the loss are briefly analyzed as follows.

One source is the fiber to waveguide coupling loss. Low losses or higher transmissions occur when the eigen modes look similar (refer to Appendix A). An overlap integral of the two fields gives the field's transmission coefficient. The loss may come from propagating along curved waveguides. This "pure bending loss" decreases exponentially with increasing radius [41]. In addition, some fields radiate not only from the bend itself, but also from the junction. If the transition is abrupt, the loss is related to the overlap integral between straight waveguide and curved waveguide. Also, the material's intrinsic loss may introduce some additional loss as in [42].

A significant source of loss occurs at the transition between the star coupler and the grating arms, especially for SiO_2-based AWG. From a theoretical point of view, it is due to the diffraction loss in the first slab region and the imperfect focusing loss in the second slab region. Both of them are caused by two factors. One is the finite number of arrayed waveguides, and the other is the waveguide gap between arrayed-waveguides at the slab-array interface that is determined by the mask process. At the discontinuity between slab and array, the field coming out of the array shows a modulation that is dependent on the gap and on the confinement of the field in the waveguide. Due to the ripples in the field pattern, a considerable fraction of power diffracts into adjacent orders and is lost. The Gaussian-shaped output field profile with reduced ripples is desired for efficient coupling to the output waveguides. It can be obtained by reducing the gap (widening the arrayed waveguide at the ends) or by reducing the confinement of the waveguide. The first method requires a better lithography process. The latter approach has some disadvantages, e.g., lower confinement will increase the minimum bend radius and degrade the crosstalk performance discussed next.

The theoretical analysis of the field mode coupling is briefly discussed in Appendix A. The comparison for different causes of equivalent optical path error is given in Table 1.3 on the next page.

1.3.6 Crosstalk

In order to expand the application field in dense WDM systems, high crosstalk suppression is required. This is an especially serious problem in an AWG with narrow wavelength spacing. In the literature on WDM devices, it is common to characterize the crosstalk performance by specifying the single channel crosstalk figure, i.e., the maximum crosstalk value that is measured with one active input channel. Under operating conditions, the crosstalk will be higher than this value because all active channels will contribute to it. Several sources that produce crosstalk are discussed in [29], which includes receiver crosstalk, truncation, mode conversion, coupling in the array, phase errors and background radiation. The first four can be kept low by proper AWG design. Whereas, the following two are mainly determined by fabrication imperfections and are thus difficult to reduce.

Phase errors are caused by any deviation from the ideal value of the optical path length of the arrayed-waveguide region. The reasons include the small deviation in the effective index due to local variation in composition, film thickness or waveguide width, or by inhomogeneous filling in of the gap near the apertures of the phased array, or the photomask resolution in real device fabrication. A comparison of the influences of the above three factors is shown in Table 1.3. Background radiation is due to the light scattered out of the waveguides at the junctions or rough wave guide edges.

Table 1.3
Comparison of different causes of path-length errors
(from [40])

Causes	Influence	Maximum equivalent path-length error (nm)
Index fluctuation	2.7×10^{-5}	≅1.7 (for ΔL=42μm)
Waveguide width/height	4.5×10^{-4}/μm (index change)	≅4 (assuming 0.2μm maximum error on width/height)
Photomask resolution	25nm-100nm	≅25-100

Since the focused beam field profile is the spatial Fourier transform of the field in the array waveguides, the sidelobes and background scattered light are attributed to the phase and amplitude fluctuations in the total electric field profile at the interface of the output slab and the array. Slowly varying fluctuations cause passband width broadening and sidelobes. On the other hand, random fluctuations generate background scattered light. Therefore, the adjacent channel crosstalk and background crosstalk are mainly attributed to the slowly varying phase fluctuation and rapid phase fluctuation, respectively.

Fourier transform spectroscopy method [44] and optical low coherence method [45] are proposed to measure the AWG's phase error distribution. The phase control method of thermo-optic thin film heaters is discussed in [46]. More recently, phase compensation is achieved by using the photo-induced refractive index change produced under UV irradiation through a metal mask in order to reduce slowly varying component [47].

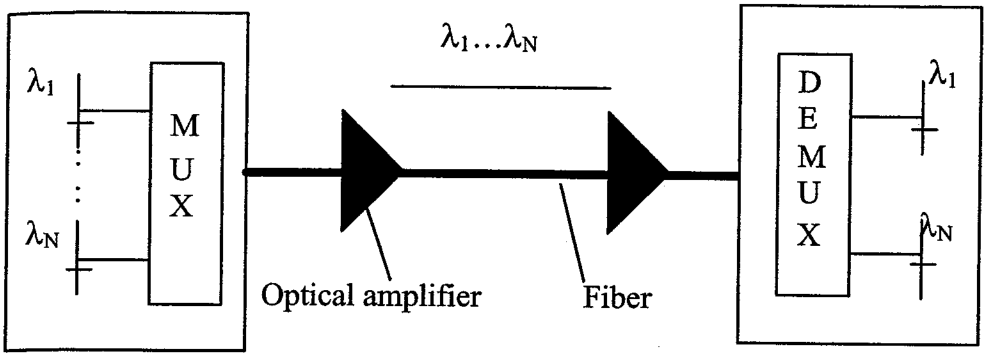

(a) Point-to-point WDM transmission

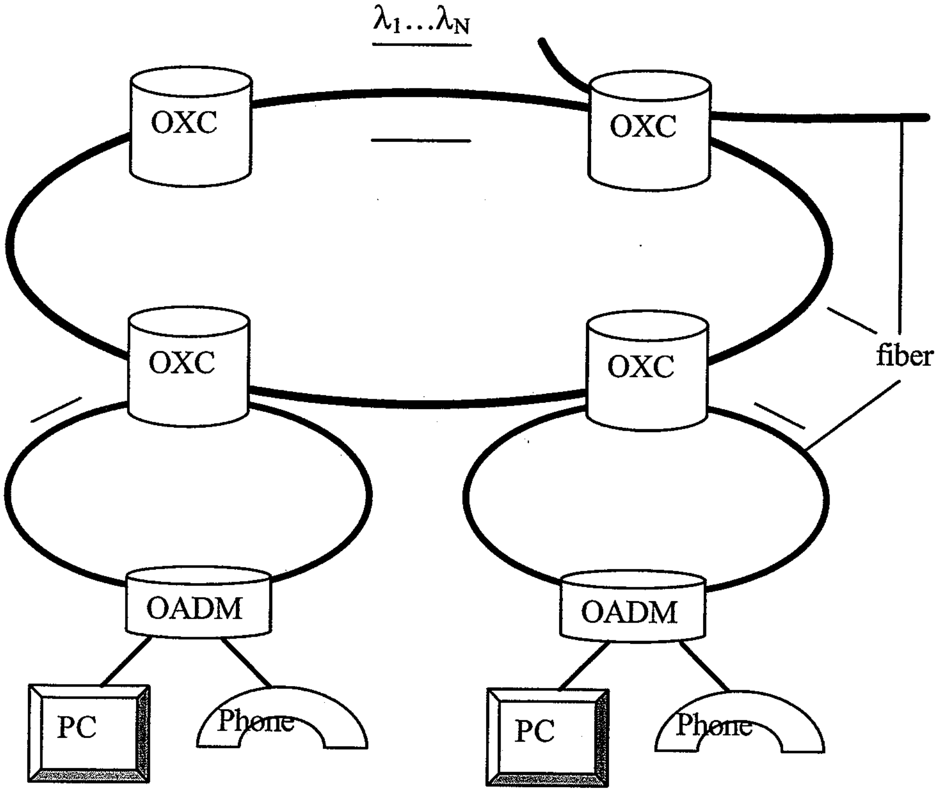

(b) Photonic network

Fig. 1.1. Optical WDM system configurations
MUX/DEMUX: WDM multi/demultiplexer
OXC: Optical crossconnect
OADM: Optical add/drop multiplexer
(modified from [6])

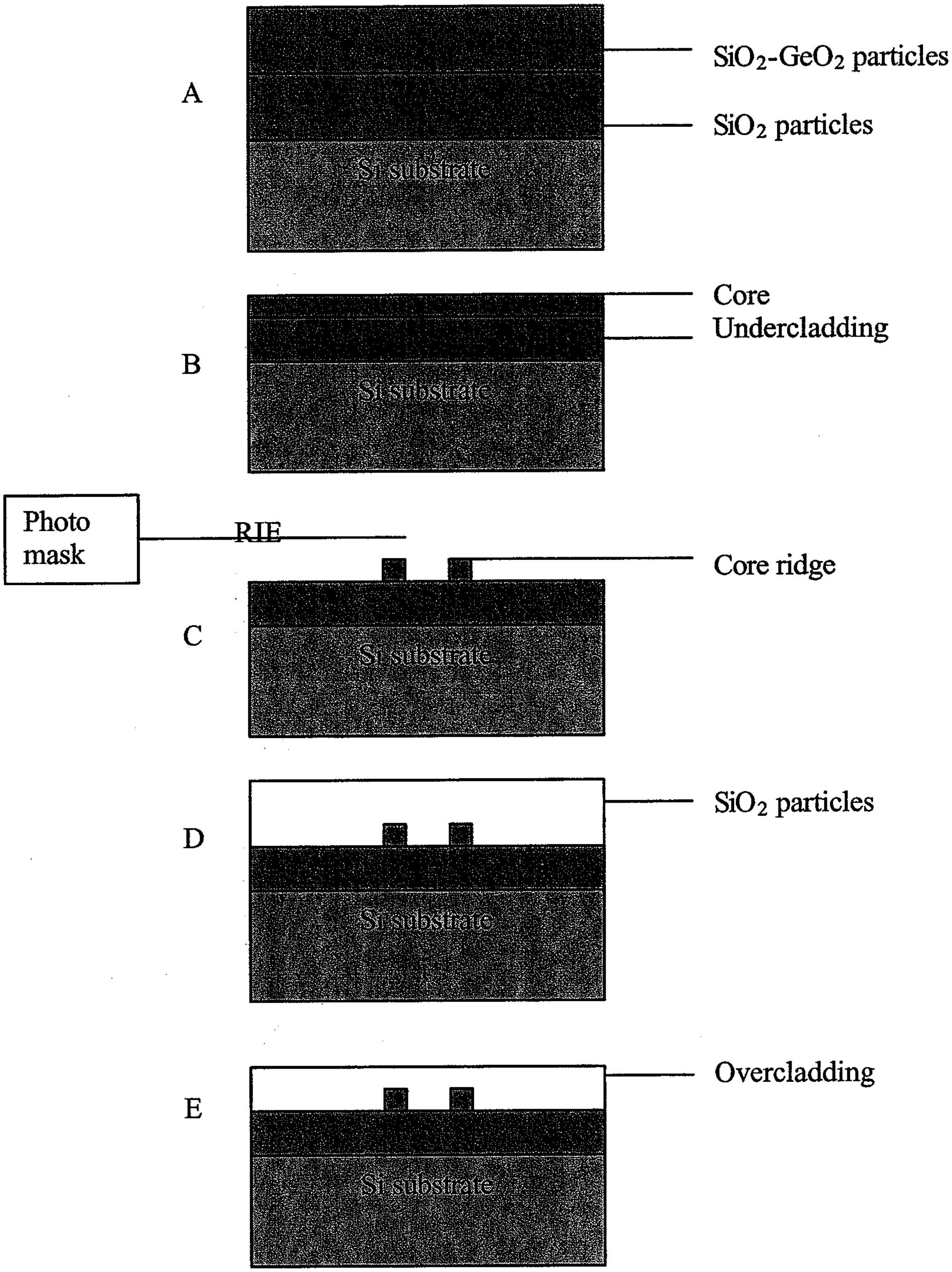

A: FHD
B: Consolidation
C: Photolithography
D: FHD
E: Consolidation

Fig 1.2. Fabrication process of silica-based planar lightwave circuits

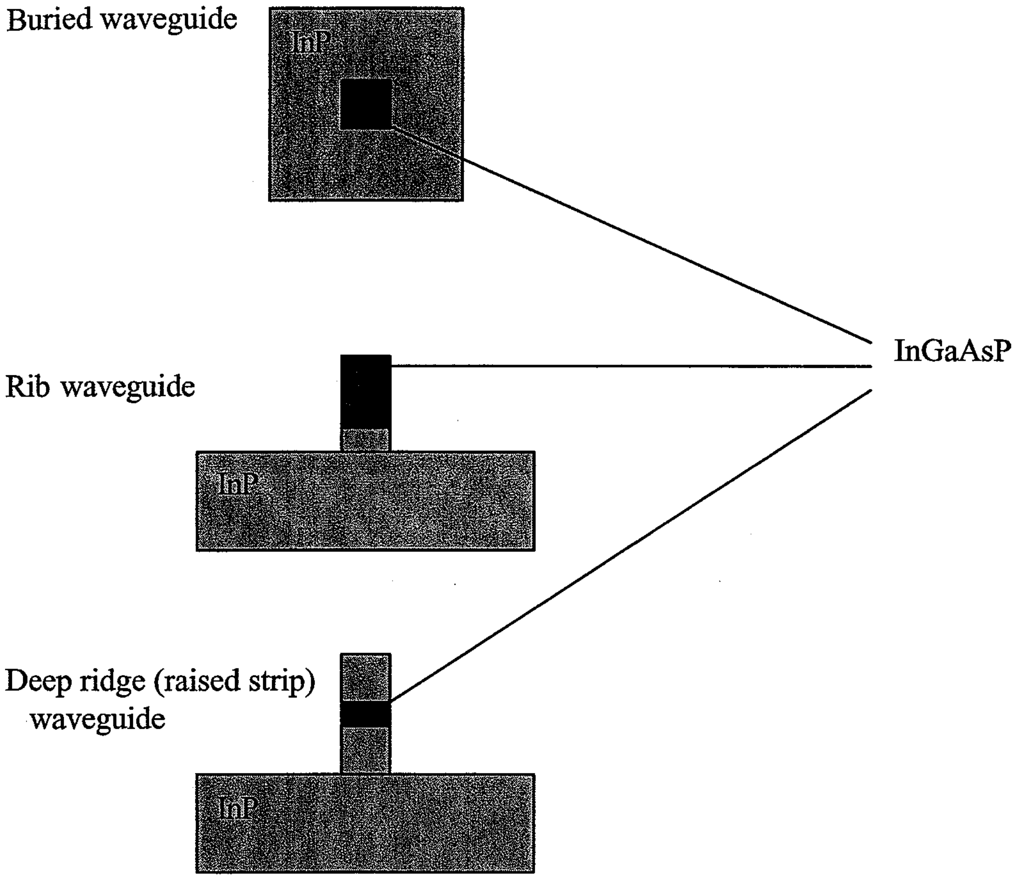

Fig 1.3. Typical InP based waveguide structures

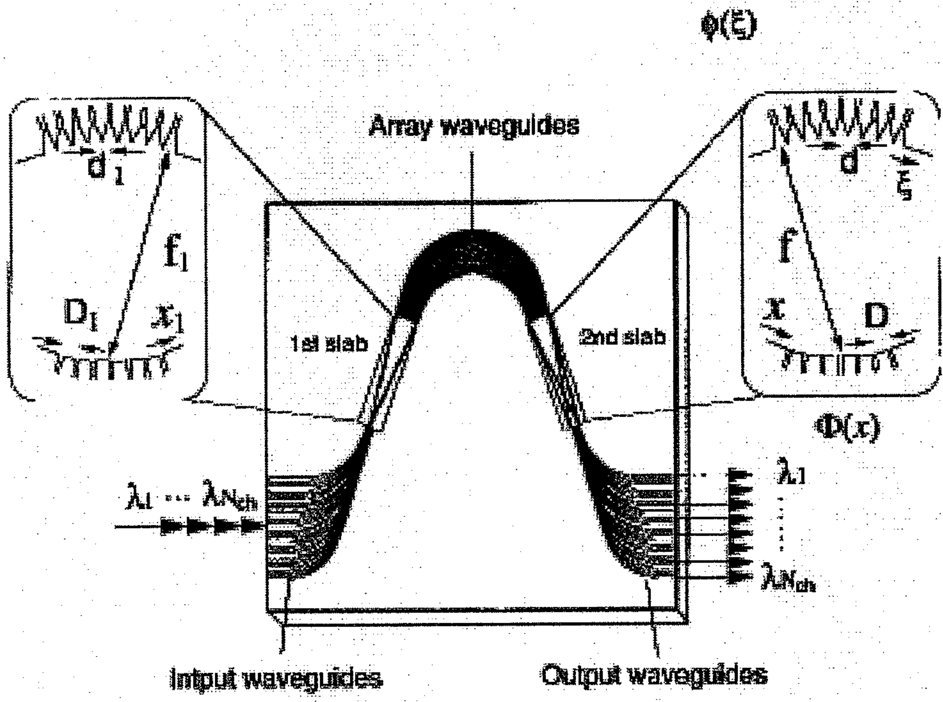

Fig. 1.4. Schematic configuration of AWG demultiplexer

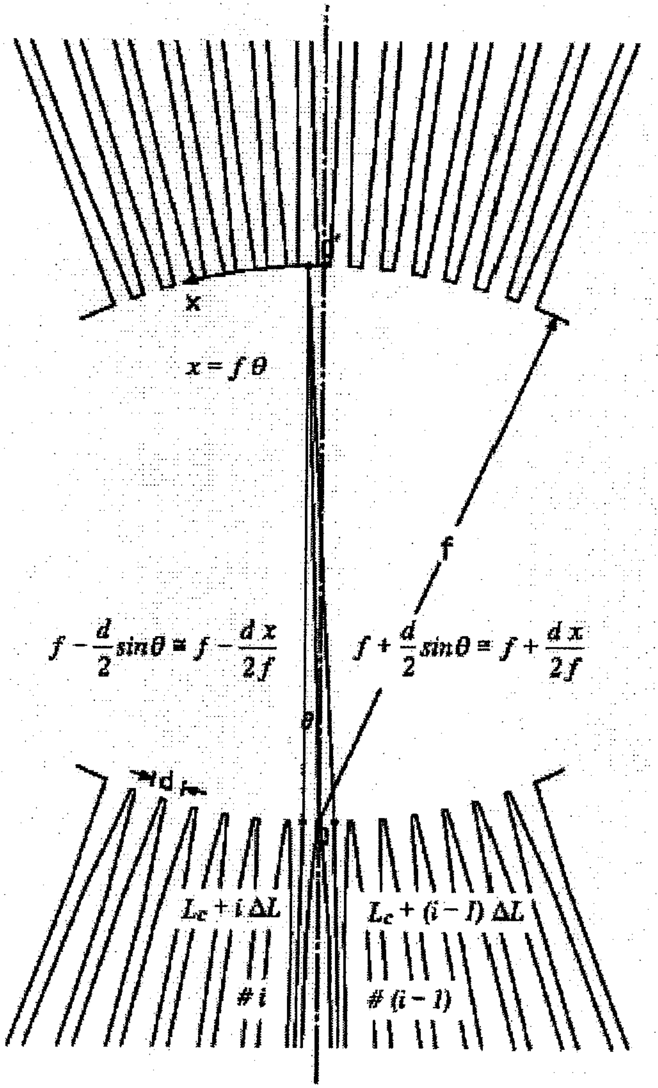

Fig. 1.5. Enlarged view of the second slab region

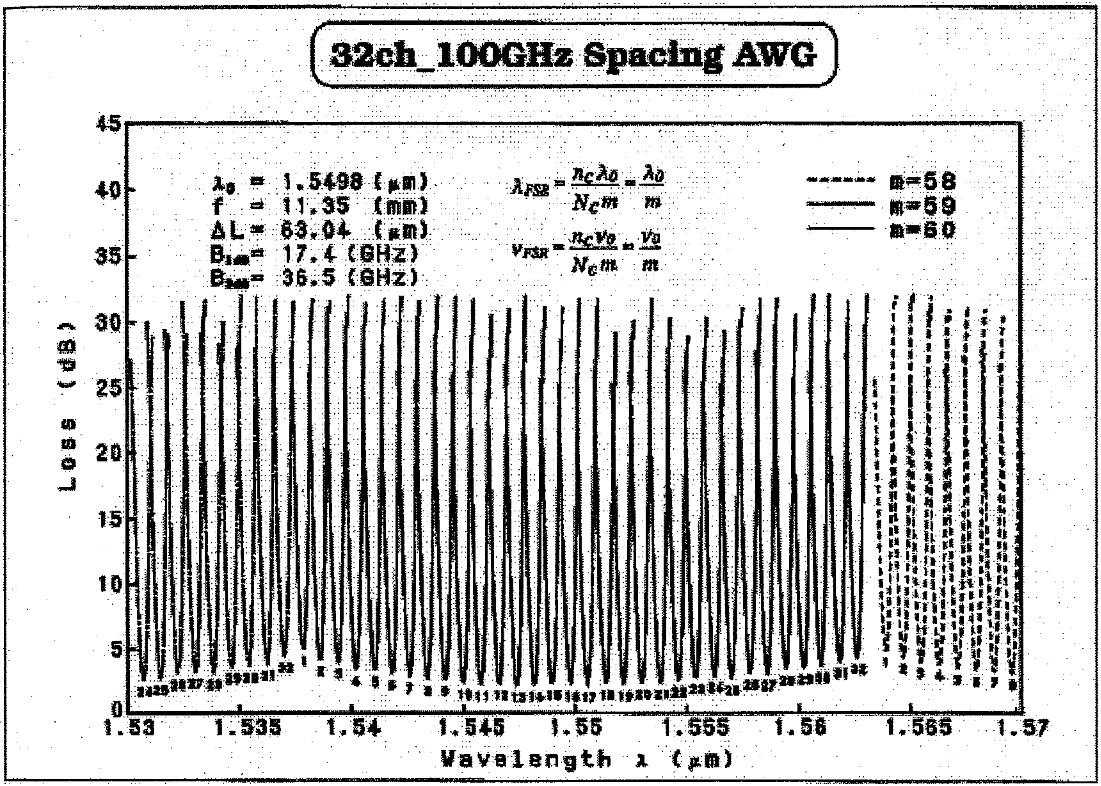

Fig. 1.6. An experimental result of transmission spectrum (from [12])

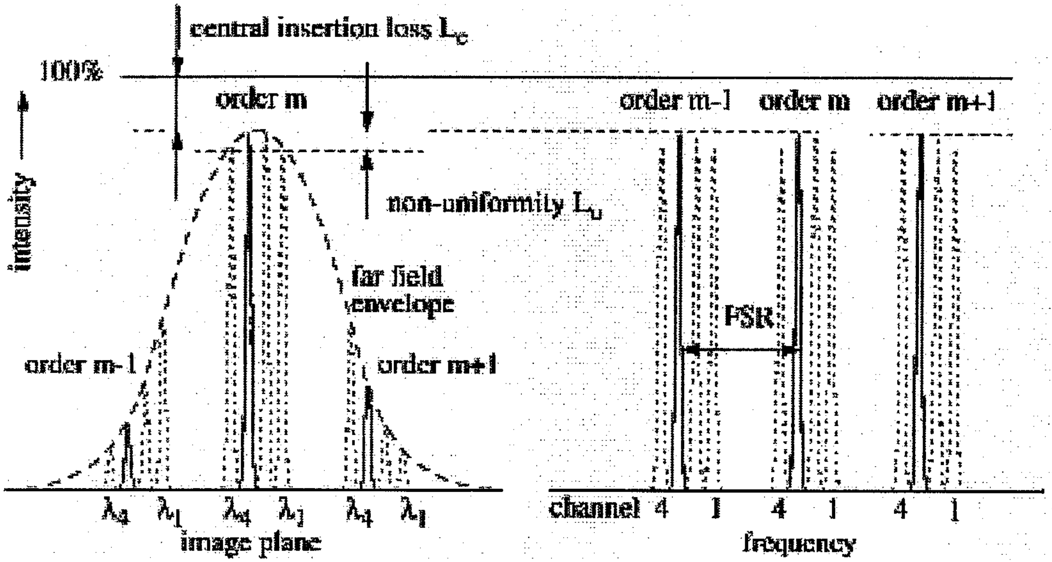

Fig. 1.7. Approximation graphs of field distribution on the image plane for four wavelengths and the corresponding transmission spectrum, in which central insertion loss, nonuniformity and FSR are shown (from [29])

2. METHOD OF IRREGULARLY-SAMPLED ZERO-CROSSINGS

In this chapter, we will discuss the proposed method of irregular-sampling zero-crossing (ISZC). At first the one-image-only digital holography is briefly reviewed. Then in section 2.2, the two-dimensional (2D) model is described and the focusing and demultiplexing properties are analyzed. The ISZC method is formulated in section 2.3 step by step. Finally we discuss theoretically the advantage of irregular sampling together with choice of zero-crossing. Simulation results and some comments are left to the next chapter.

2.1 One-Image-Only Digital Holography

The proposed method originates from the method by Ersoy in [48] to generate hologram that reconstructs only one visible image. The method is based on the recognition that the pairs of images are due to the mirror symmetry of the two spaces on either side of the hologram plane. The symmetry can be changed either by choosing a hologram surface that is not planar, or a reference wave that is not a plane-perpendicular wave. However, using off-axis plane wave only distorts the symmetry and results in images that are at different positions than before. An attractive choice is a spherical reference wave combined with an encoding technique of digital holography developed by Ersoy [49]. The analysis of image formation shows that it is possible to focus one particular order at a time. If some conditions are satisfied, all the images of other orders become defocused and out of view in the far distance where the desired image is. It was theoretically and experimentally shown that this method could reconstruct only one image.

2.2 Virtual Model

2.2.1 Introduction

Our ISZC method originates from the basic idea of one-image-only digital holography. This method is in regard to the design of a novel wavelength demultiplexer that has a very similar structure to the conventional AWG. The most prominent advantage of the proposed device is that each demultiplexed wavelength has only one active effective order on the image plane. In contrast, several images of adjacent orders will show up (please refer to Fig. 1.7) in conventional AWG. Therefore, the number of operating wavelength channels is not restricted due to the limited distance between neighboring orders, the FXR in Eq. (1.12), even though other tradeoff limitations do exist. This is achieved by introducing a special type of phase change (in addition to the pure linear phase change induced by the arrayed waveguides in conventional AWG) at the zero-crossing sampling points, where the arrayed waveguides are located. It is found that other order diffraction beams tend to be defocused and appear as background noise at the far-distance image plane where the beam of the desired order is located. In particular, we discuss how to obtain the desired phase shift by means of a spherical reference wave and the zero-crossing locating algorithm.

2.2.2 Model analysis

Our virtual model in 2-D geometry is shown in Fig. 2.1, assuming that y-coordinates are constants and thus omitted. The derivation follows [51]. The coordinates are denoted by (x,z). Based on the discussion in [48][49], the position of each hologram aperture (x_i, 0) for one-image-only hologram using spherical reference wave is chosen according to

$$\varphi(x_i,0)+kr_{oi}=2q_i\pi+\varphi_0 \tag{2.1}$$

where $\varphi(x_i,0)$ is the phase shift caused by the wave propagation from the source of the spherical reference wave (x_c,z_c) to the i-th aperture $(x_i,0)$, φ_0 is the desired phase at the object point (x_o,z_o), kr_{oi} is the phase shift caused by the wave propagation from the aperture $(x_i,0)$ to the object point (x_o,z_o), and q is an integer.

The general equation used in our model is given as

$$\varphi(x_i,0)+\theta(x_i,0)+kr_{oi}=2q_i\pi+\varphi_0 \tag{2.2}$$

In our virtual model, x_i also corresponds to the position of each arrayed waveguides. $\theta(x_i,0)$ is added for the purpose of demultiplexing. It can be realized like in the conventional AWG by $\theta(x_i,0) = k_c l_i$, k_c is the wave number in the arrayed waveguide, l_i is the physical length of the ith arrayed waveguide, which is written as $l_i = l_0 + \alpha x_i$. In order to transform this virtual model to the real AWG structure, $\varphi(x_i,0)$ and kr_{oi} should use the wave number in slab region k_s.

Eq.(2.2) is changed into:

$$k_s r_{ci} + k_c(l_0 + x_i\alpha) + k_s r_{oi} = 2q_i\pi + \varphi_0 \qquad (2.3)$$

Making use of paraxial approximations, we can get:

$$\begin{aligned} r_{oi} &= \sqrt{(x_0 - x_i)^2 + z_0^2} = z_0 + \frac{x_0^2 + x_i^2}{2z_0} - \frac{x_0 x_i}{z_0} \\ r_{ci} &= \sqrt{(x_c - x_i)^2 + z_c^2} = z_c + \frac{x_c^2 + x_i^2}{2z_c} - \frac{x_c x_i}{z_c} \end{aligned} \qquad (2.4)$$

Substituting Eq.(2.4) into Eq.(2.3) and neglecting those constant phase result in:

$$x_i\delta - n_s x_i\left(\frac{x_c}{z_c} + \frac{x_o}{z_o}\right) + n_s\frac{x_i^2}{2}\left(\frac{1}{z_0} + \frac{1}{z_c}\right) = q_i\lambda \qquad (2.5)$$

where $\delta = n_c\alpha$. The reason that the constant phases could be omitted is that we are only interested in the intensity distribution on the image plane and the constructive interference is desired for λ. While the exact phase information is less important since it is not sort of image reconstruction problem in the holography. It should be noted that Eq.(2.5) must be satisfied for each arrayed waveguide.

Now Eq.(2.5) is applied to another wavelength λ', the focus of which is (x_0', z_0').

$$x_i\delta - n_s x_i\left(\frac{x_c}{z_c} + \frac{x_o'}{z_o'}\right) + n_s\frac{x_i^2}{2}\left(\frac{1}{z_o'} + \frac{1}{z_c}\right) = q_i\lambda' \qquad (2.6)$$

Taking ratio of the above two equations, we can get:

$$\frac{x_i\delta - n_s x_i\left(\frac{x_c}{z_c} + \frac{x_o'}{z_o'}\right) + n_s\frac{x_i^2}{2}\left(\frac{1}{z_o'} + \frac{1}{z_c}\right)}{x_i\delta - n_s x_i\left(\frac{x_c}{z_c} + \frac{x_o}{z_o}\right) + n_s\frac{x_i^2}{2}\left(\frac{1}{z_o} + \frac{1}{z_c}\right)} = \frac{\lambda'}{\lambda} = r \qquad (2.7)$$

The new focal point (x_0', z_0') is obtained by solving the above equation and noticing that it should be satisfied for any x_i,

$$z_o' = \frac{1}{\frac{r-1}{z_c} + \frac{r}{z_o}}$$

$$x_o' = \frac{r\frac{x_o}{z_o} - (r-1)(\frac{\delta}{n_s} - \frac{x_c}{z_c})}{\frac{r-1}{z_c} + \frac{r}{z_o}} \tag{2.8}$$

If we assume that

$$\frac{r-1}{z_c} << \frac{r}{z_o}, \tag{2.9}$$

Eq.(2.8) can be simplified as

$$z_o' = \frac{z_o}{r}$$

$$x_o' = x_o - z_o\frac{r-1}{r}(\frac{\delta}{n_s} - \frac{x_c}{z_c}) \tag{2.10}$$

The above derivations show that the focal point z-coordinates of different wavelengths are very close to z_0. In other words, the focal points for different wavelength components tend to be on the same vertical image plane perpendicular to the z-direction, as we want for the output waveguide arrangement. On that image plane, the dispersion relation in x-direction can be obtained as

$$\Delta x = x_o' - x_o = -z_o\frac{r-1}{r}(\frac{\delta}{n_s} - \frac{x_c}{z_c})$$

$$= -z_o\frac{\lambda' - \lambda}{\lambda'}(\frac{\delta}{n_s} - \frac{x_c}{z_c}) \approx -z_o\frac{\Delta\lambda}{\lambda}(\frac{\delta}{n_s} - \frac{x_c}{z_c}) \tag{2.11}$$

$$\frac{\Delta x}{\Delta\lambda} = -z_o\frac{1}{\lambda}(\frac{\delta}{n_s} - \frac{x_c}{z_c})$$

The angular dispersion in far-field region can also be derived as

$$\Delta\theta = \frac{\Delta x}{z_o} = -\frac{\Delta\lambda}{\lambda}(\frac{\delta}{n_s} - \frac{x_c}{z_c})$$

$$\frac{\Delta\theta}{\Delta\lambda} = -\frac{1}{\lambda}(\frac{\delta}{n_s} - \frac{x_c}{z_c}) \tag{2.12}$$

We find that the dispersion is dependent on two terms, δ/n_s and x_c/z_c. If x_c/z_c is not taken into account, the following derivation can relate Eq. (2.12) and Eq.(1.8) and prove they are equivalent.

From Eq. (2.12), we get

$$\frac{\Delta\theta}{\Delta\lambda} = -\frac{1}{\lambda}\frac{\delta}{n_s} = -\frac{1}{\lambda}\frac{n_c\alpha}{n_s} = -\frac{1}{\lambda}\frac{n_c}{n_s}\frac{\Delta l_i}{\Delta x_i} \tag{2.13}$$

From Eq. (1.8), we get

$$\frac{\Delta\theta}{\Delta\lambda} = \frac{\Delta x}{f} = \frac{n_g \Delta L}{n_s d\lambda_0} \tag{2.14}$$

Eq. (2.13) and Eq. (2.14) are identical except the different notations and sign definition used in our virtual model and the conventional AWG.

The second term x_c/z_c is produced by the spherical reference wave. When the assumption made in Eq.2.9 is valid, z_c should be large enough that the spherical reference wave turns into a plane wave of an off-axis angle whose direction cosine is x_c/z_c. It can be easily understood by thinking of the plane wave incident wave to a normal uniform grating.

2.2.3 Average diffraction order

In the above subsection, δ is a very important parameter we introduce and use for the convenience of analysis and simulation. In comparison to the diffraction order m defined in Chpater 1, we name δ as diffraction coefficient. Their relation is as follows,

$$\delta = n_c\alpha, \quad \Delta l_i = \alpha\Delta x_i,$$
$$m_i = \frac{n_c\alpha\Delta x_i}{\lambda_0} = \frac{\delta\Delta x_i}{\lambda_0(1.55\mu m)} \tag{2.15}$$

In regular AWG, Δx_i is a constant, thus m is also invariant. However, the proposed new device has variant Δx_i's as we shall see in the next section. Therefore, m is defined as average diffraction order calculated by Eq. (2.15) with average Δx_i plug in.

This section talks about the virtual model evolving from the ideas of one-image-only digital holography as well as its demultiplexing properties. It is called "virtual model" because it is not the real model directly determining the design parameters of our R-AWG, instead, a sort of tool helping us greatly in terms of theoretical and computational investigation. How to transfer the virtual model into real device design is an important issue addressed in Chapter 4.

2.3 Irregularly-Sampled Zero-Crossings Algorithm

The derivation in previous section is based on the general equation Eq. (2.5), which involves the concept of zero-crossings from a viewpoint of signal processing. As a matter of fact, x_i's, the hologram point locations, or the corresponding arrayed waveguide positions, are the zero-crossing points in this system, in which they spatially sample the input lightwave and reconstruct it. Besides zero-crossings, the other indispensable concept used in the algorithm is irregular sampling. Together they can essentially reduce the other diffraction orders (harmonics). More explanations related to zero-crossings and irregular sampling will be found in the next section. While in this section, the irregular-sampling zero-crossing (ISZC) method is formulated in three steps after an explanation of the parameters.

Max_X: the range in x-direction (starting from 0) for the location of the arrayed waveguides

M: Number of arrayed waveguides

DX: The average interval that each array waveguide occupies (=Max_X/M)

RandX: The parameter in the [0,1] interval, which is used to estimate the degree of randomness in nonuniform sampling

X(i) (i=1..M): x-coordinates of the arrayed waveguides, the nonuniform-sampling zero-crossing points that we want and use later for the design

Xe(i) (i=1..M): x-coordinates of the nonuniform-distributed points that are not zero-crossing, intermediate parameters

Xu(i) (i=1..M): x-coordinates of the initial uniformly distributed points, intermediate parameters

Step 1

Initializing Xu(i) by

$$Xu(i)=(i-0.5)\bullet DX,\ i=1..M \qquad (2.16)$$

Actually Xu(i) is the center point of each unit interval [(i-1)•DX , i•DX].

Step 2

Producing Xe(i) by adding Xu(i) with a displacement, which is a random variable uniformly distributed in the range of [-0.5•DX•RandX , 0.5•DX•RandX]

$$Xe(i) = Xu(i)\ \text{(from step1)} + \text{random displacement for nonuniform-sampling},\ i=1..M \tag{2.17}$$

Step 3

Calculating X(i) by adding Xe(i) with a correction term that is solved by the algorithm given in Appendix B:

$$X(i) = Xe(i) + \text{correction term for zero-crossings},\ i=1..M \tag{2.18}$$

The final results of X(i)'s by implementing the above method are essentially equivalent to the x_i's used in the previous theoretical derivations.

2.4 Discussion of Irregular Sampling

The demultiplexing properties of our virtual model have been proved in section 2.2. Another important aspect that should also be examined before transforming the virtual model to real R-AWG design is regarding the reduction of undesired order harmonics. As mentioned before, the most prominent advantage of our novel R-AWG is eliminating or reducing those harmonic diffraction beams so that they cannot be focused on the image plane. Therefore those places that were occupied by harmonics before are free for new wavelength channels now. In other words, as for conventional AWG, FSR limits the number of wavelength channels since the focal point of m-order harmonic beam of one wavelength could be overlapped with that of the m+1 or m-1 order of another wavelength. The crosstalk is not tolerable. While in our proposed device, such problems do not exist; the number of channels may be still limited by other factors though.

The approach we use to deal with undesired order harmonics is irregular sampling and zero crossing. Based on our method of irregularly-sampled zero-crossings formulated in the previous subsection, it is shown that the irregular sampling is realized by choosing the initial irregularly distributed points first and then calculating the closest zero-crossing points accordingly. In this method, one important parameter determining the degree of randomness is RandX. The larger RandX is, the more nonuniformly are the points distributed, the larger are the irregularity that those points follow. Now let's see how RandX matters.

In Fig. 2.2, the index number for the arrayed waveguides is still represented by i. Their coordinate in x-direction and the angle to z-axis are represented by x_i and θ_i respectively. θ is a constant denoting the angular distance between adjacent waveguides in the conventional AWG. u is a random variable that has a uniform distribution in the interval of [-1/2, 1/2]. RandX in the formulation of the NSZC method is still used here. The development is adopted from [51]. RandX is chosen as

$$\theta_i = i \cdot \theta + RandX \cdot u \cdot \theta \tag{2.19}$$

When RandX=0, the device becomes the conventional one with all the arrayed waveguides uniformly spaced on the Rowland circle. In our proposed R-AWG, RandX is in the interval (0,1].

E(X) is the total field at X on the image plane. It should be the vector sum of the light waves that propagate out of each arrayed waveguide. The assumption made here is that they have unit amplitude (neglecting the Gaussian profile) and common initial phase (as a result of the characteristic of zero-crossings). Then we can write E(X) as

$$E(X) = \sum_{i=1}^{M} \exp(jk_s r_i) \tag{2.20}$$

where k_s is the wave number in the output slab region, and r_i is calculated as

$$\begin{aligned} r_i(X) &= \sqrt{(X + R\sin\theta_i)^2 + (R\cos\theta_i)^2} = \sqrt{X^2 + 2XR\sin\theta_i + R^2} \\ &= R\sqrt{1 + \frac{X^2 + 2XR\sin\theta_i}{R^2}} \approx R\left(1 + \frac{1}{2}\frac{X^2 + 2XR\sin\theta_i}{R^2}\right) = R + r_i^{'}(X) \\ where \quad & r_i^{'}(X) = \frac{1}{2R}(X^2 + 2XR\sin\theta_i) \end{aligned} \tag{2.21}$$

$$\begin{aligned} E(X) &= \sum_{i=1}^{M} \exp(jk_s r_i) = \exp(jk_s R)\sum_{i=1}^{M} \exp(jk_s r'(X)) \\ &= \exp(jk_s R)\sum_{i=1}^{M} \exp(j\frac{k_s}{2R}(X^2 + 2XR\sin\theta_i) \\ &= \exp(jk_s(R + \frac{X^2}{2R}))\sum_{i=1}^{M} \exp(jk_s X \sin\theta_i) \end{aligned}$$

$$Power \quad P(X) = a|E(X)|^2 = a\left|\sum_{i=1}^{M} \exp(jk_s X \sin\theta_i)\right|^2 \approx a\left|\sum_{i=1}^{M} \exp(jk_s X\theta_i)\right|^2 \tag{2.22}$$

where a is a constant relating power and amplitude.

For the conventional AWG, Eq.(2.19) is changed into

$$\theta_i = i \cdot \theta \tag{2.23}$$

Phase matching condition for the m-th order diffraction is

$$k_s X(\theta_i - \theta_{i-1}) = k_s X\theta = 2m\pi \tag{2.24}$$

$$X_m = \frac{2m\pi}{k_s\theta} \tag{2.25}$$

$$P_{reg}(X_m) = aM^2 \tag{2.26}$$

Now let's investigate what happens to the position of X_m when we introduce random sampling by setting a non-zero RandX.

Letting $$Q_i = \exp(jk_s X\theta_i), \tag{2.27}$$

they are identically independently distributed random variables.

$$\begin{aligned} E[P_{ran}(X_m)] &= aE[|\sum_{i=1}^{M} Q_i|^2] = a(\sum_{i=1}^{M} E[Q_i Q_i^*] + \sum_{i=1}^{M}\sum_{j=1, j\neq i}^{M} E[Q_i]E[Q_j^*]) \\ &= a(M + (M^2 - M)E[Q_i]E[Q_i^*]) \end{aligned} \tag{2.28}$$

$$
\begin{aligned}
Q_i &= \exp(jk_s X_m \theta_i) = \exp(jk_s X_m (i\cdot\theta + RandX\cdot u\cdot\theta)) \\
&= \exp(jk_s \frac{2m\pi}{k_s\theta}(i\cdot\theta + RandX\cdot u\cdot\theta)) = \exp(j2m\pi\cdot RandX\cdot u) \\
E(Q_i) &= \int_{-\frac{1}{2}}^{\frac{1}{2}} \exp(j2m\pi\cdot RandX\cdot u)du = \frac{1}{j2m\pi\cdot RandX}(e^{jm\pi\cdot RandX} - e^{-jm\pi\cdot RandX}) \\
E(Q_i^*) &= \frac{1}{-j2m\pi\cdot RandX}(e^{-jm\pi\cdot RandX} - e^{jm\pi\cdot RandX}) \\
E(Q_i)E(Q_i^*) &= \frac{1}{4\pi^2 m^2 RandX^2}(2-2\cos(2m\pi RandX)) = \frac{1-\cos(2m\pi RandX)}{2\pi^2 m^2 RandX^2} \\
&= \frac{\sin^2(\pi m RandX)}{\pi^2 m^2 RandX^2} = \sin c^2(\pi m RandX)
\end{aligned}
\tag{2.29}
$$

$$
\begin{aligned}
E[P_{ran}(X_m)] &= a(M + (M^2 - M)E[Q_i]E[Q_i^*]) \\
&= a(M + (M^2 - M)\sin c^2(m\pi RandX))
\end{aligned}
\tag{2.30}
$$

When RandX=0, it is regular AWG, $E[P_{ran}(X_m)] = aM^2 = P_{reg}(X_m)$, same as Eq. (2.25)

When RandX>0, it is our proposed device R-AWG, $E[P_{ran}(X_m)] < aM^2 = P_{reg}(X_m)$. It proves that harmonics are reduced.

Thus, irregular sampling reduces the power in regular harmonics due to sampling?. However, nonlinear encoding of phase also generates harmonics. The choice of zero-crossings together with spherical reference wave greatly reduces the harmonics on the image plane as discussed by Ersoy [49].

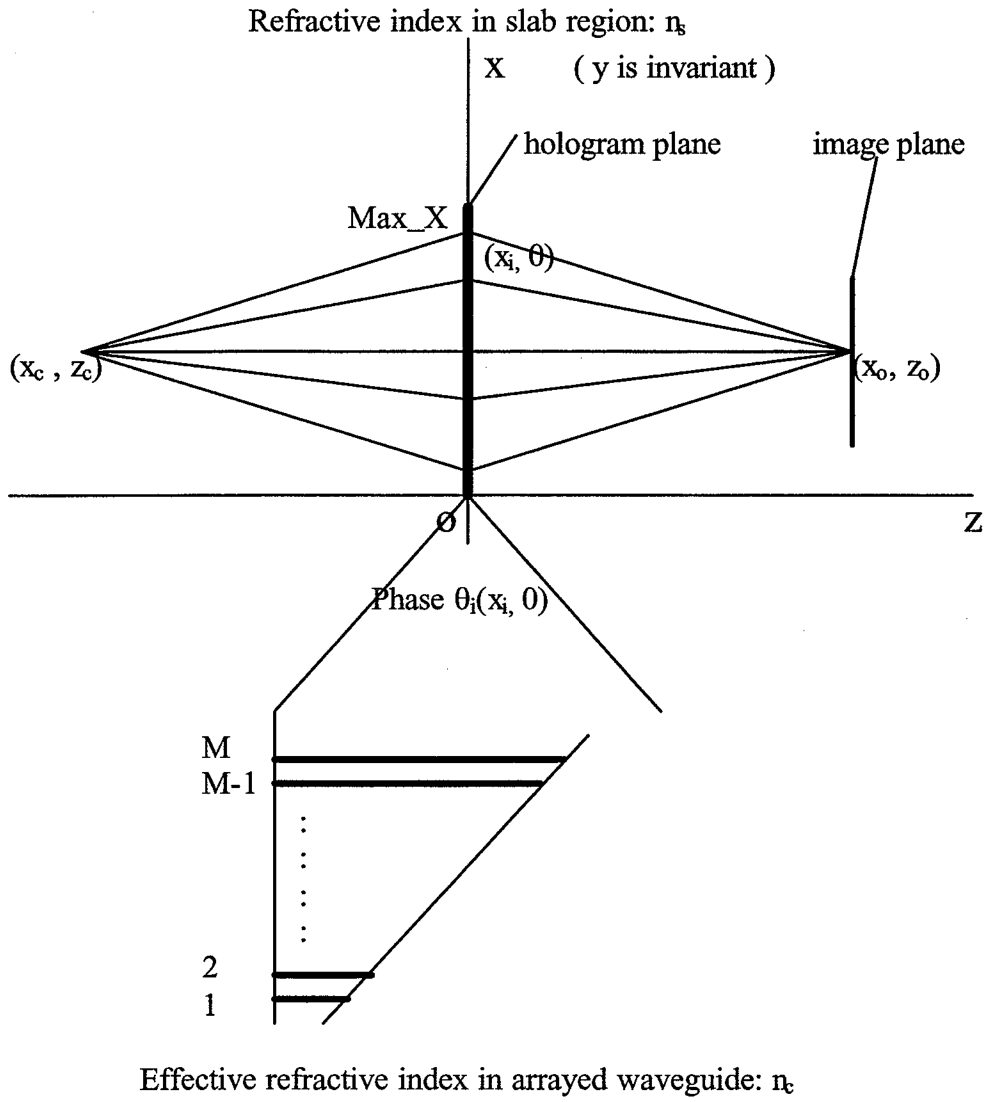

Fig. 2.1. The 2D schematic diagram for the virtual model

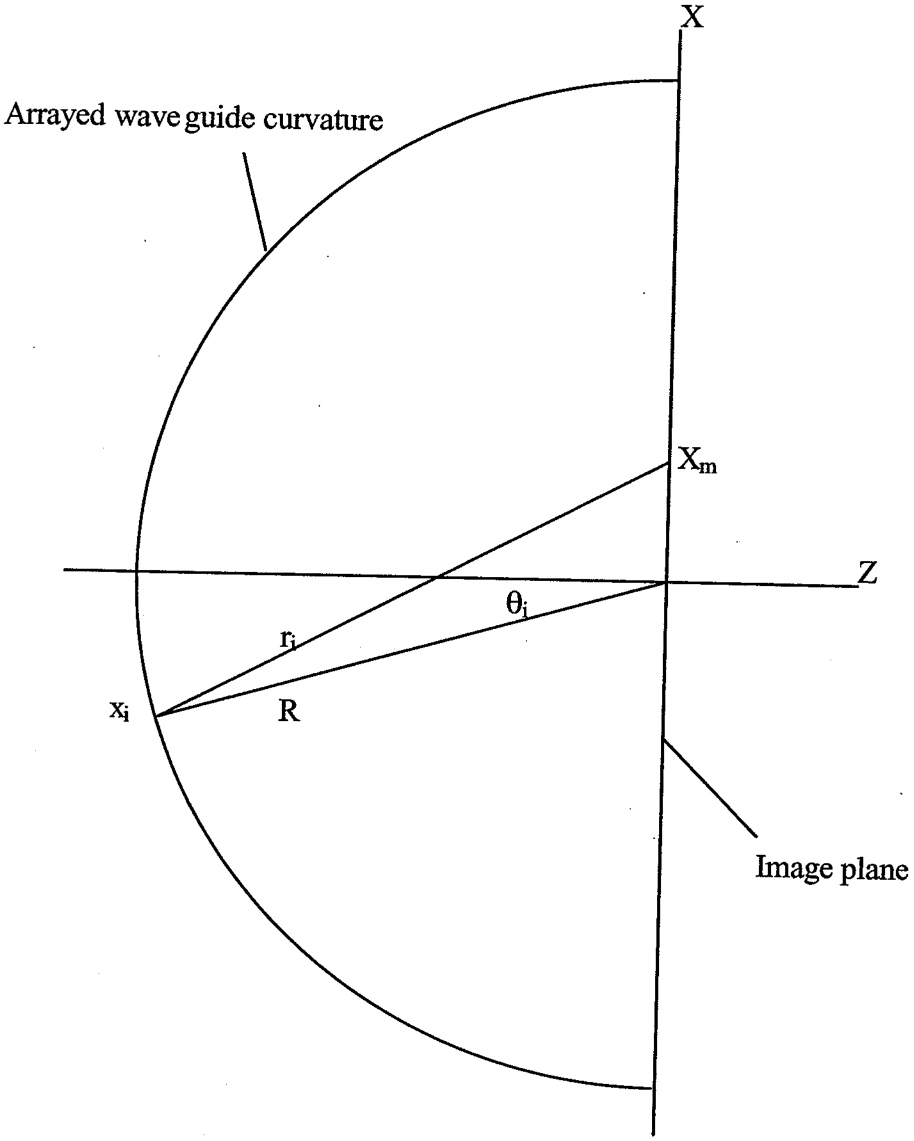

Fig. 2.2. Part of output star coupler and the image plane

3. SIMULATIONS AND DISCUSSION

3.1 Simulation Techniques

Matlab is utilized for our computational tasks. The basic principle of our simulation is based on the elementary electro-magnetic field theory, the total electric field is determined by the superposition of the field components (complex term with amplitude and phase) contributed by each individual arrayed waveguide (please refer to Eq. (2.19)). Basically our attention is focused on the output star coupler. The virtual model shown in section 2.2 is investigated and the method of irregular-sampling zero-crossings described in section 2.3 is applied. Furthermore, the far-field radiation characteristics of Gaussian mode discussed in Chapter 1 and Appendix A is also incorporated into the calculation. Compared to those more accurate computation techniques extensively used in electro-magnetics and optics community, such as Beam Propagation Method (BPM), Finite Difference Time Domain (FDTD) Method, our simulation method is quite simple and direct. Nevertheless, it can approximately generate some typical results, such as the total field distribution on X-Z plane (2-D colored graph), the total field distribution on the image plane (1-D cross-section-view graph), the transmission spectrum, the arrayed waveguide location diagram, etc. As a matter of fact, they are good enough for us to approximately investigate the properties of the R-AWG. More accurate simulation method and results will be addressed in the next chapter.

3.2 Results and Discussion

In this section, the simulations are implemented by Matlab codes and the results are given. Based on a simple example of demultiplexing four wavelengths, we testify the dispersion relation derived in the previous chapter and the function of irregular sampling with zero-crossing to eliminating the harmonics. Then, we investigate the influences to the performance arising from the degree of irregular sampling, the number of the arrayed waveguides, the power profile, as well as the phase (length) error tolerance. Finally we give the results of multi-channel operation.

3.2.1 An example of four wavelength channels

Fig. 3.1-4 show the four typical simulation results mentioned in the above paragraph, based on the parameters listed below, where w_0 represents the effective mode width of each individual arrayed waveguide.

$M=100, N=4, RandX=1, \delta=10, m=129, n_s=1, \Delta\lambda=0.8nm,$

$Max\_X=2mm, x_c=x_o=1mm, z_c=z_o=20mm, w_0=3\mu m$

The focal points spacing of two adjacent wavelengths is obtained from Eq. (2.11)

$$|\Delta x| = z_o \frac{|\Delta\lambda|}{\lambda}(\delta - \frac{x_c}{z_c}) = 20mm \times \frac{0.8nm}{1550nm} \times (10 - \frac{1mm}{20mm}) = 102.7\mu m$$

This value is very close to $\Delta x \cong 101\mu m$, the average of the spacings between adjacent wavelengths' focal points on the z_o=20mm image plane, which is estimated from Fig. 3.3.

3.2.2 Dispersion relation verification

In order to further testify our dispersion relation Eq. (2.11), we make a scan of different $\Delta\lambda$ and produce a Δx vs. $\Delta\lambda$ graph based on the same parameters used above. After that, we make another scan of different δ, different m accordingly and produce a Δx vs. δ graph, also with the same parameters. The two graphs are Fig. 3.5 (a) and (b), respectively. The slopes calculated by using Eq. (2.11) are perfectly matched up with the values achieved by linearly fitting the points on those two graphs. From the results, it is easily found that the diffraction coefficient δ or the corresponding diffraction order m determines the space that adjacent wavelengths are separated on the image plane provided other parameters are the same.

3.2.3 Function of irregular sampling

Now we are going to find how the value of RandX influences the results. Fig. 3.6-9 show the results with the same parameters as in 3.2.1, except RandX is chosen as 1.0, 0.5, 0.25, 0, respectively. For the convenience of comparisons, we put Fig. 3.1 and 3.2 together to form a new figure, Fig. 3.6. The larger the RandX is, the more nonuniformly are the points distributed, the larger are the irregularity that those points would follow.

When RandX decreases, the beams of different order are increasingly showing up on the image plane. At the same time, the device is more like the conventional device, and the noise level is more reduced. It is clearly shown that the function of irregular sampling is to reduce the harmonics. If the regularity of the sampling points is destroyed enough to a certain degree, the undesired order harmonic beams tend to be defocused, and appear as noise on the image plane.

3.2.4 Number of arrayed waveguides

The influence by number of arrayed waveguides is shown in Fig. 3.10-11. Changing the number of waveguides is equivalent to changing the average grating pitch (DX) if the focal length, the divergent angle of the array region and thus the array range (Max_X) are also all fixed. Two sets of parameters investigated here are M=200, DX=10μm, m=64.5 and M=50, DX=40μm, m=258 compared to M=100, DX=20μm, m=129 in section 3.2.1. In accordance with the theory of diffraction gratings, adding more grating waveguides improves the crosstalk performance, as shown in these two figures. However, increasing the waveguide number not only requires larger chip size but also introduce more unavoidable phase and amplitude errors caused by the imperfect optical properties of waveguides, e.g., variations of material index, waveguide core size, etc. An optimal number should be determined experimentally with the consideration of device yield per wafer and fabrication technologies [40].

3.2.5 Power profile

By using a limited number of grating waveguides at the input slab region, the AWG can only collect a fraction of the input optical power. This leads to the power truncation issue. Fig. 3.12-13 show the results of power profile influence on the crosstalk. The values of grating pitch and focal length are fixed parameters here for this investigation. The change in the number of waveguides changes the divergent angle and therefore the amount of collected power from the input slab region as well, which is often quoted as a percentage ratio between the outmost waveguide and the center waveguide. We can notice that the crosstalk read from the figures is getting slightly better when the number of waveguides increases. Another significant point is that the transmission peak for each operation wavelength is sharper, that is, the width of the peak is smaller for larger number of waveguides. This can be explained by the diffractive optics theory that involves the interference analysis. Such characteristics are especially important for demultiplexing densely spaced WDM wavelengths.

3.2.6 Waveguide path length error

Performance of AWG is largely affected by the phase errors induced by the path-length errors of the arrayed waveguides. Several causes are shown in Table 1.3 with their equivalent path-length errors. In [40], an assumption is made that the path-length errors are Gaussian-distributed with assigned standard deviation and the effect of path-length errors to the crosstalk performance of regular AWG is investigated. Likewise, in our approach, the typical values of standard deviation of path length error, 25nm, 50nm, 75nm, 100nm are introduced into the simulation of our virtual-model device. Table 3.1 shows that the crosstalk property is not considerably affected by the phase errors, as compared to the regular AWG. We conclude that the reason is that the non-uniform and random characteristics of device structure essentially improve the error tolerance.

Table 3.1
Crosstalk Deviation due to Path Length Error

STDEV of path length error (nm)	0	25	50	75	100
Regular AWG (dB)	-36	-28	-16	-18	-16
R-AWG (dB)	-18	-17	-15	-13	-12

3.2.7 32/64/128-channel simulation

Based on the experience and knowledge mentioned above, we choose different combination of device parameters to achieve the virtual model designs of the 32CH-100G(0.8nm), 64CH-50G(0.4nm) and 128CH-25G(0.2nm) demultiplexers and obtain the corresponding simulation figures as shown in Fig 3.14-16, respectively.

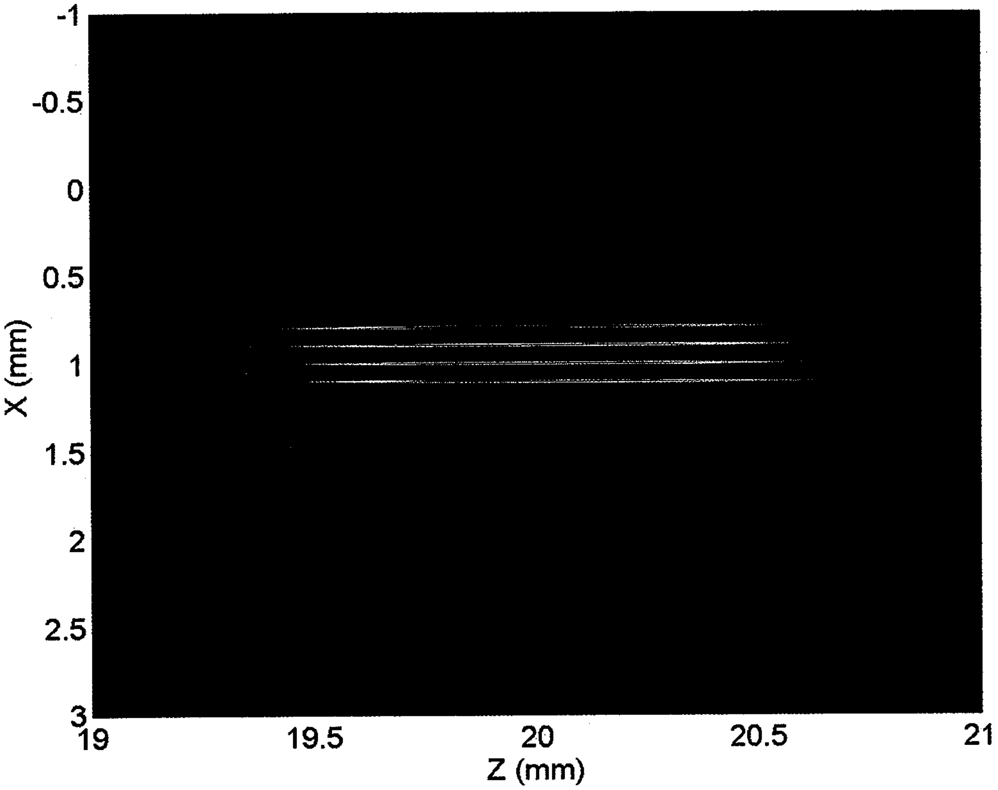

Fig. 3.1. Total field distribution on the X-Z plane (m=129)

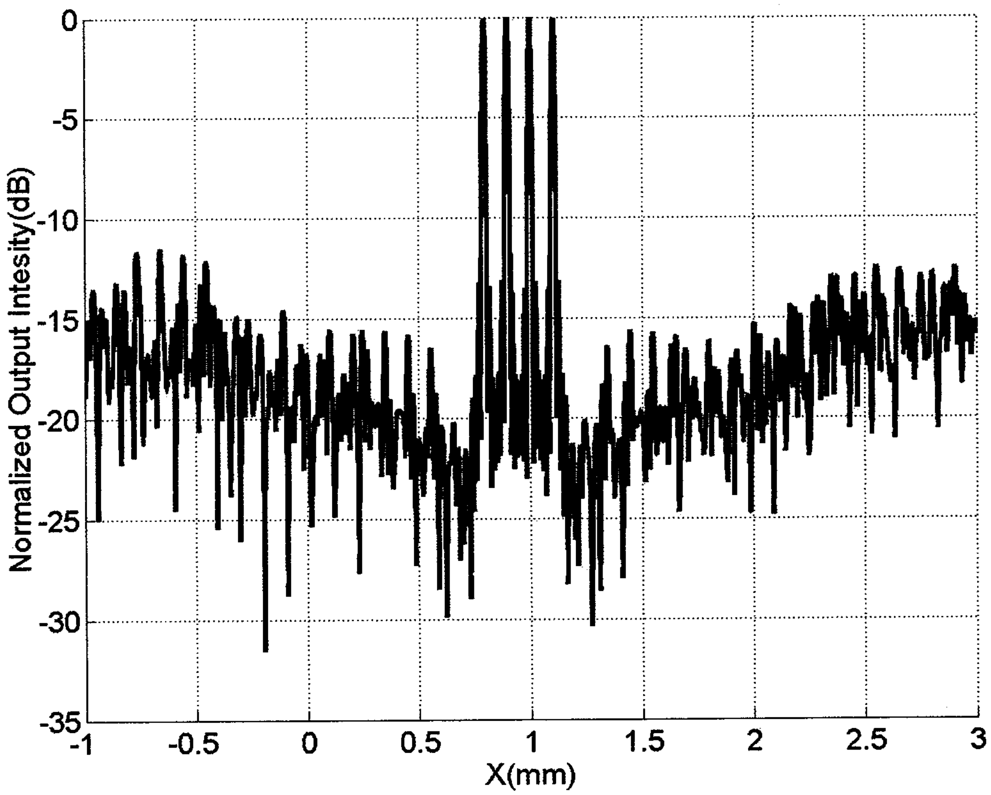

Fig. 3.2. Normalized field intensity on the image plane
(X-Y plane at $z=z_o$, x is variant, y is constant, m=129)

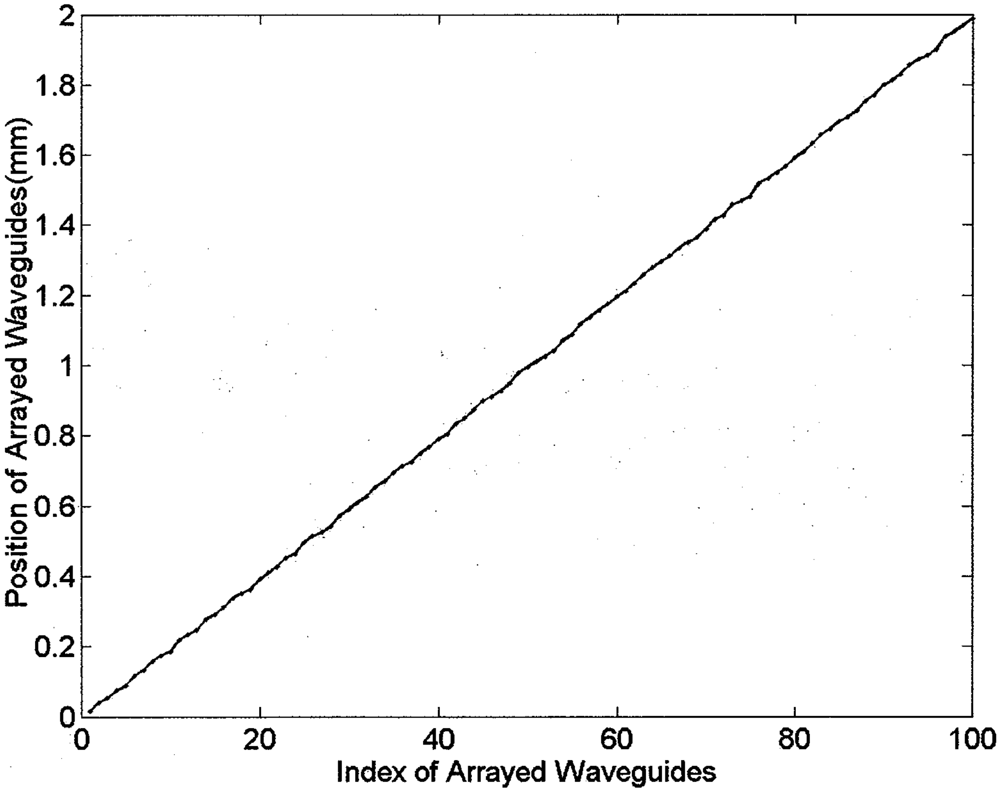

Fig. 3.3. Arrayed waveguide distribution (m=129)

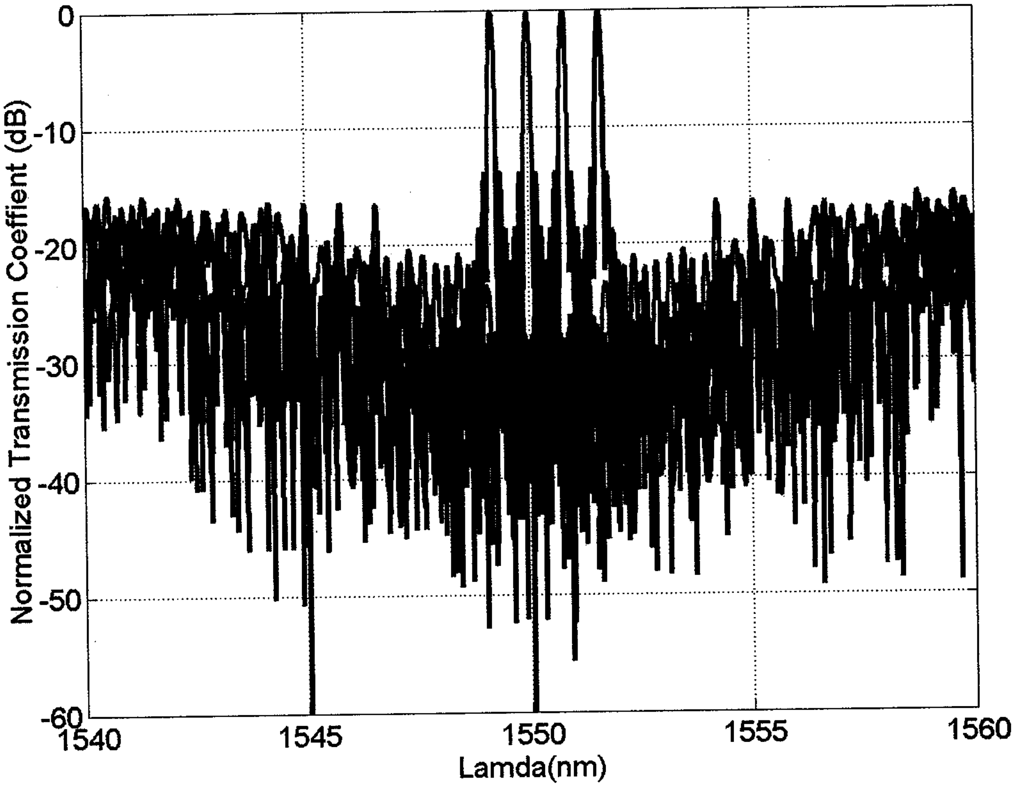

Fig. 3.4. Transmission spectrum (wavelength response), m=129

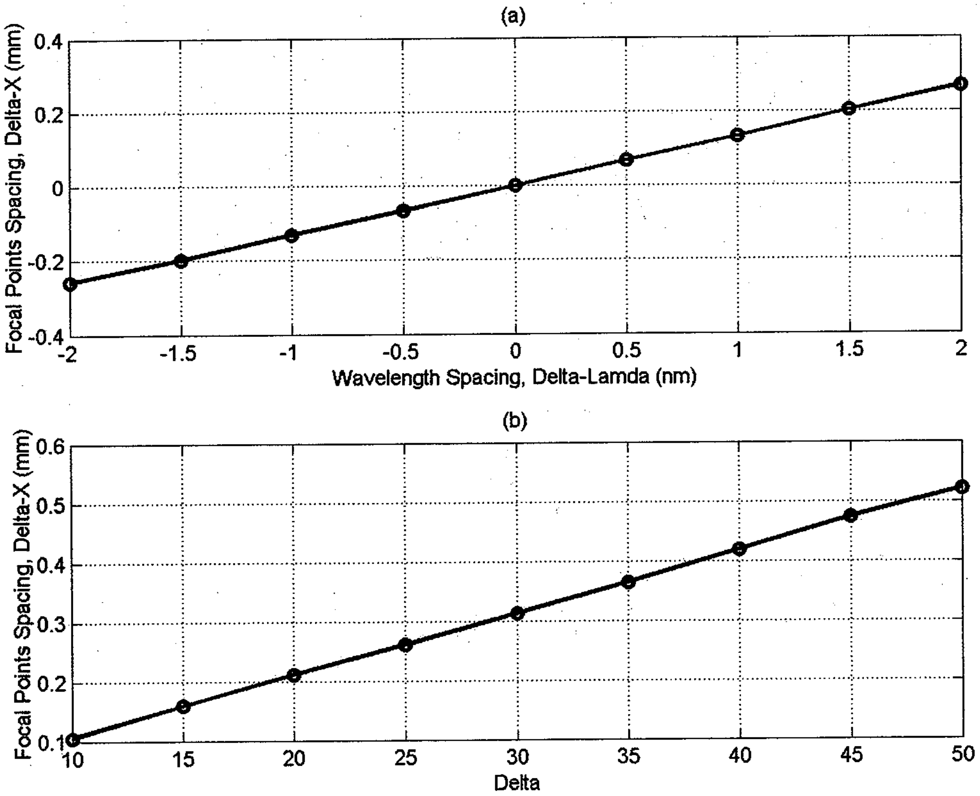

Fig. 3.5. Dispersion relation
(a) Δx vs. Δλ (m=129) (b) Δx vs. δ (∝m)

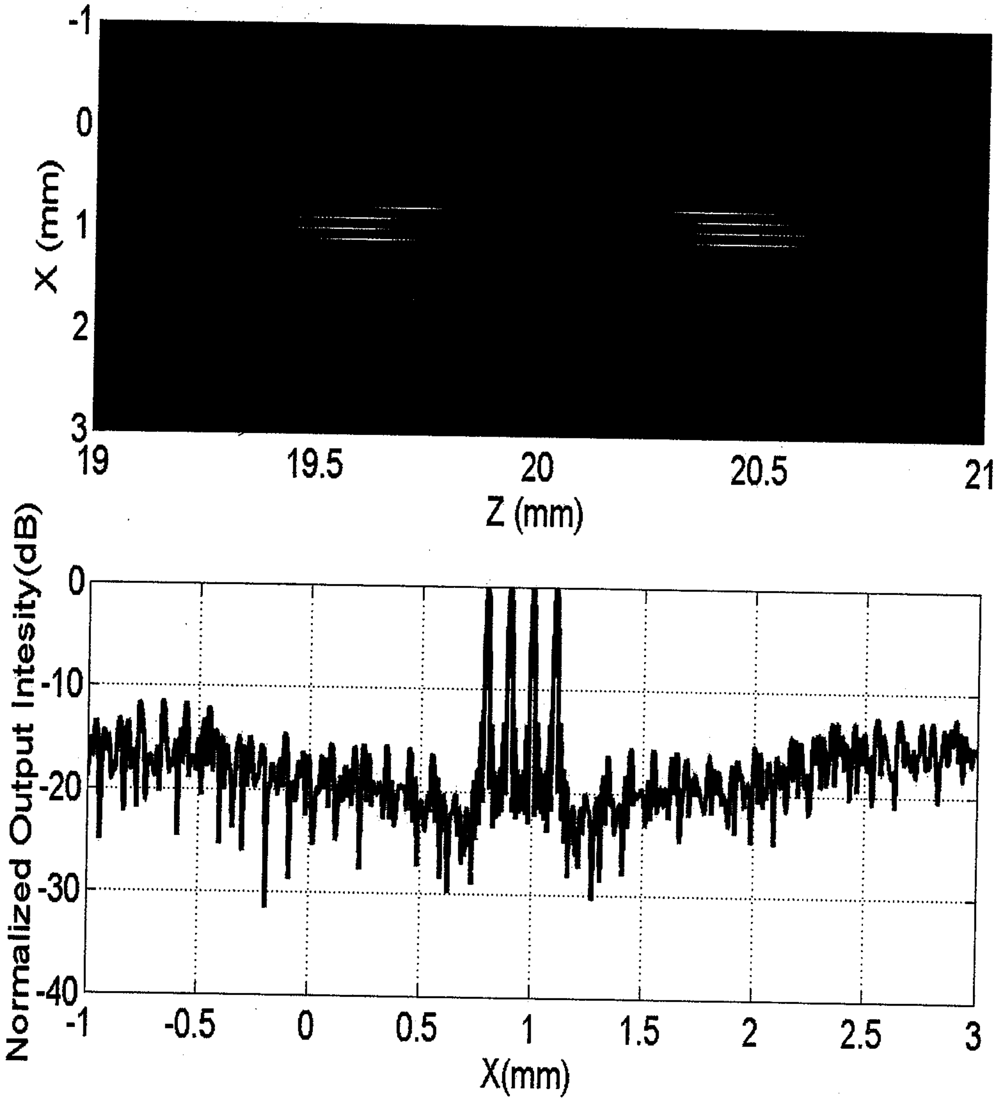

Fig. 3.6. Combination of Fig. 3.1 and Fig. 3.2
RandX=1.0 (same parameters as in Fig. 3.1-4.)

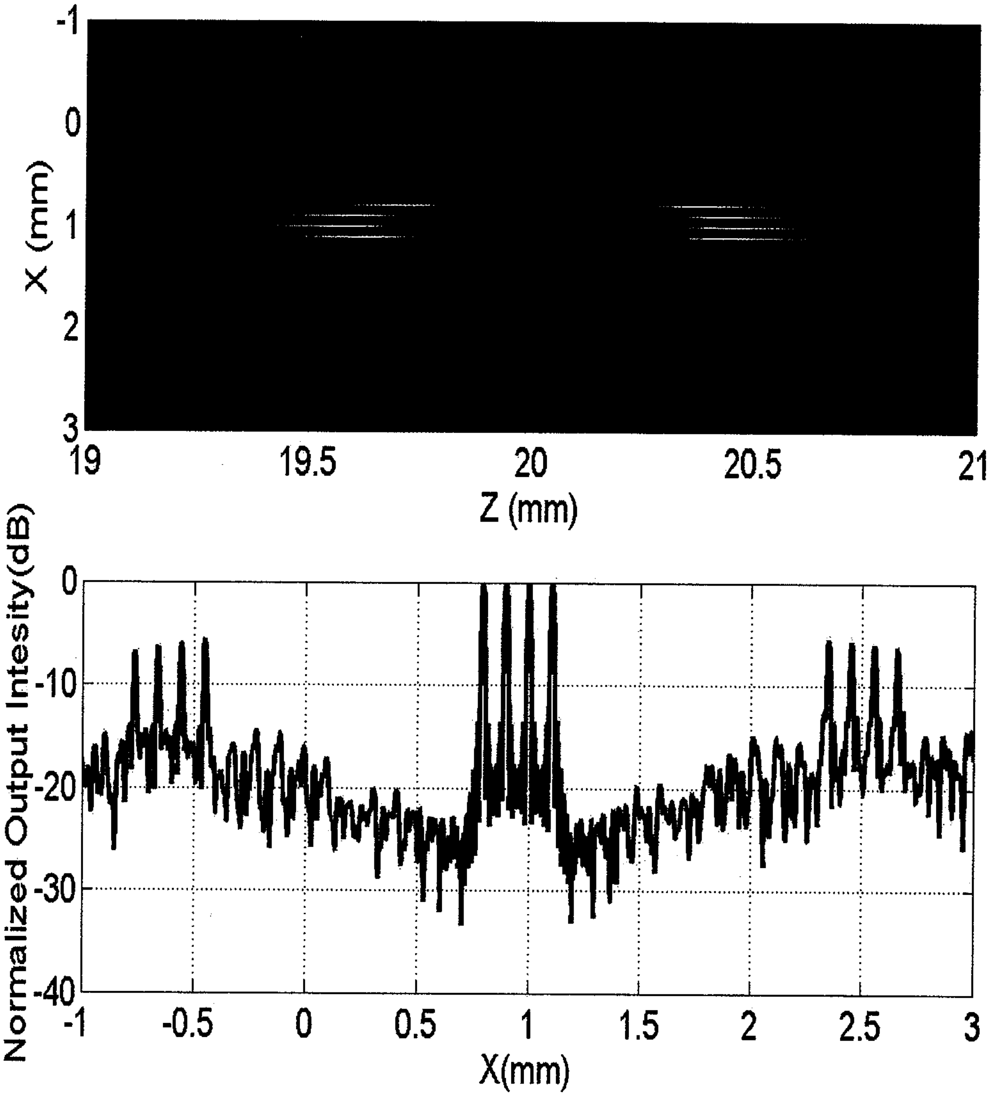

Fig. 3.7. RandX=0.5 (other parameters are same as those used in Fig. 3.6)

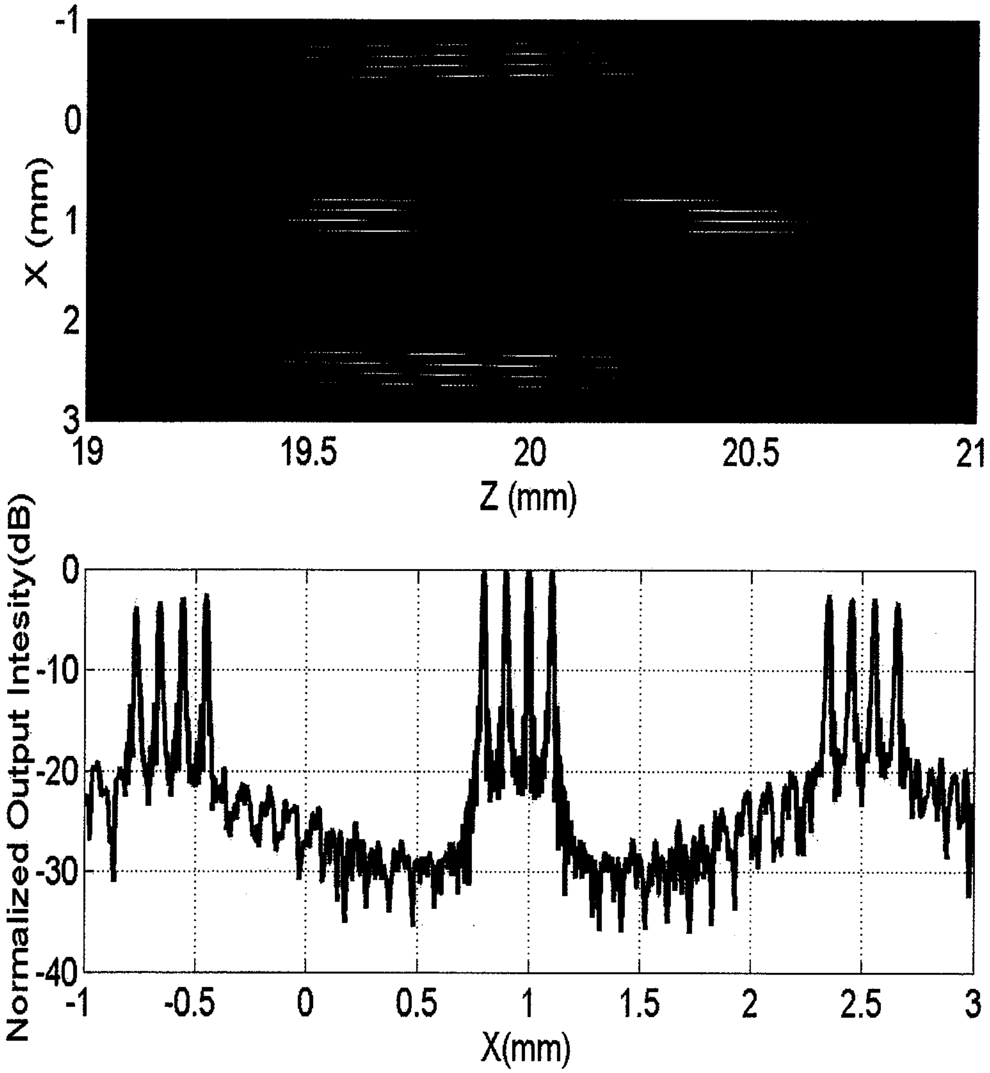

Fig. 3.8. RandX=0.25 (other parameters are same as those used in Fig. 3.6)

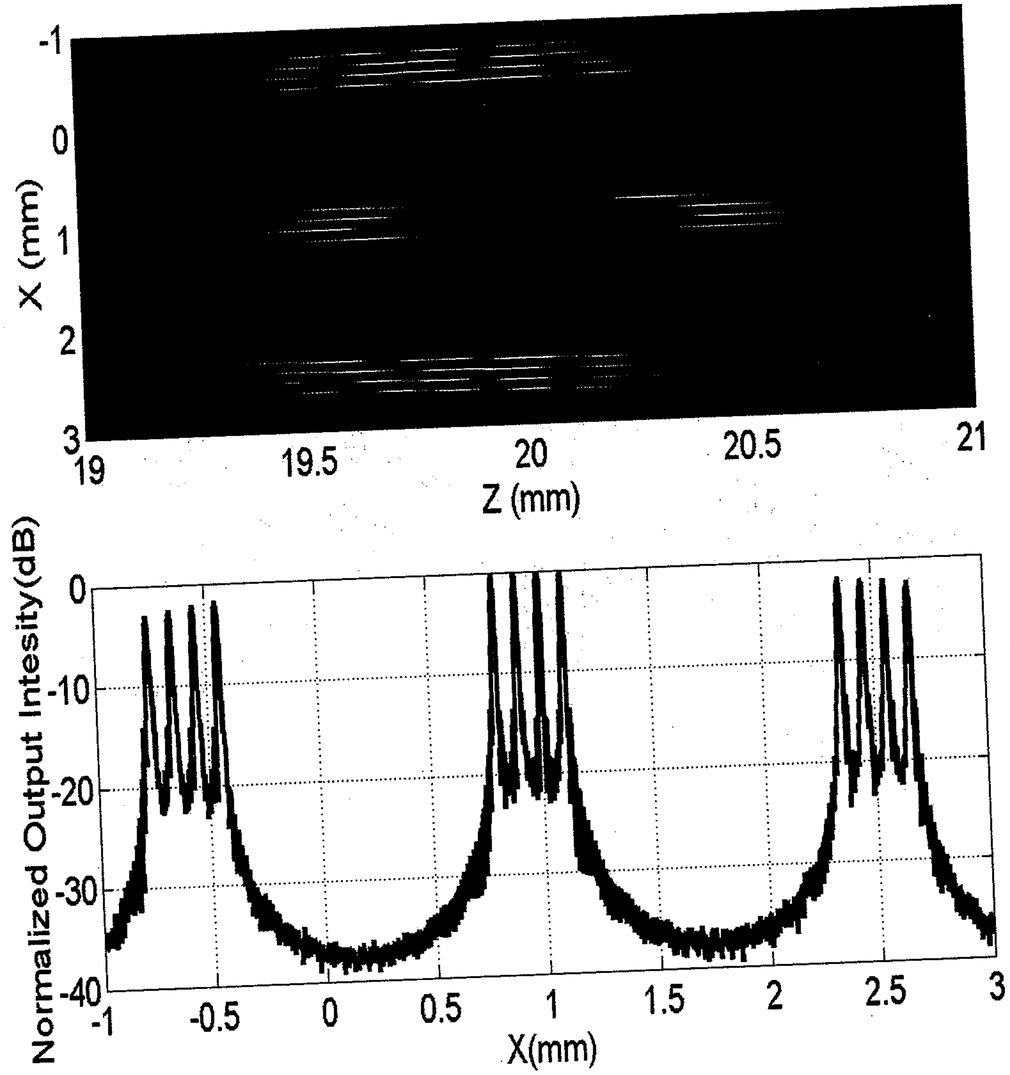

Fig. 3.9. RandX=0 (other parameters are same as those used in Fig. 3.6)

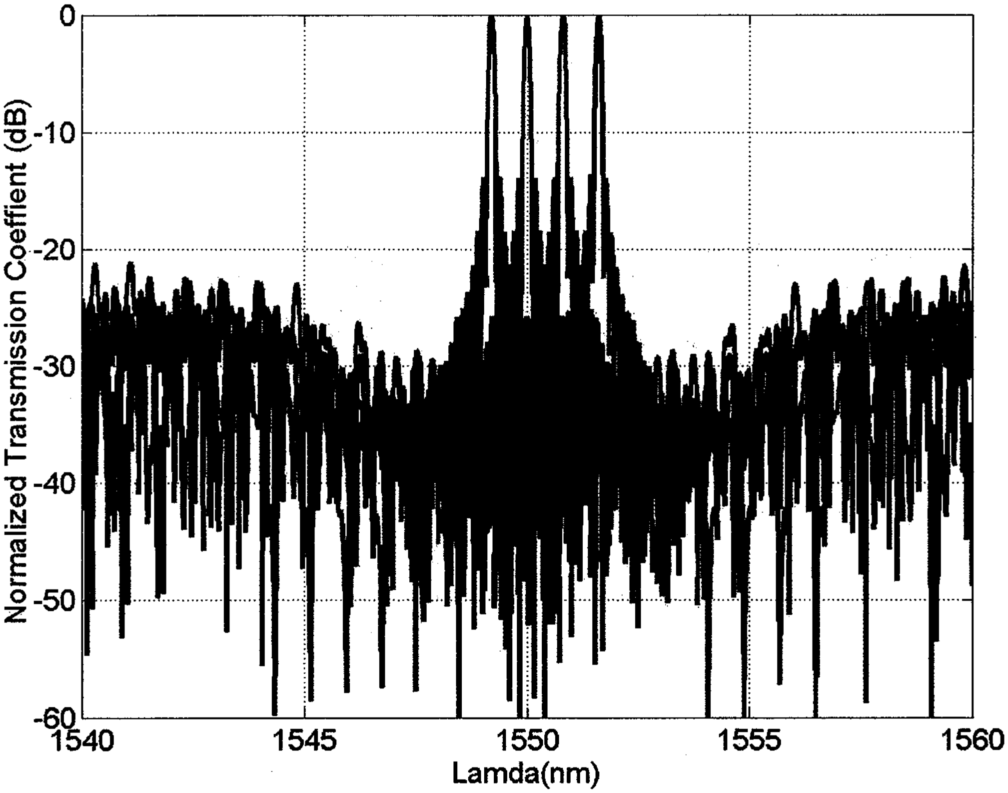

Fig. 3.10. M=200, DX=10μm, m=64.5
(other parameters are same as those used in Fig. 3.6)

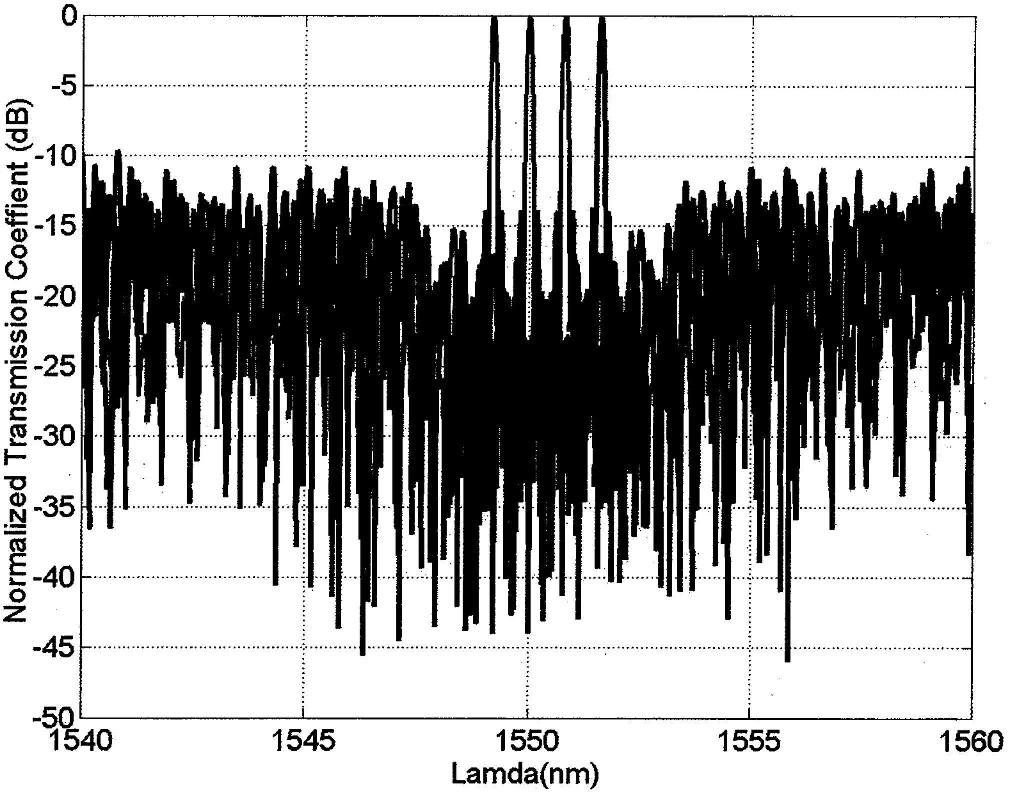

Fig. 3.11. M=50, DX=40μm, m=258
(other parameters are same as those used in Fig. 3.6)

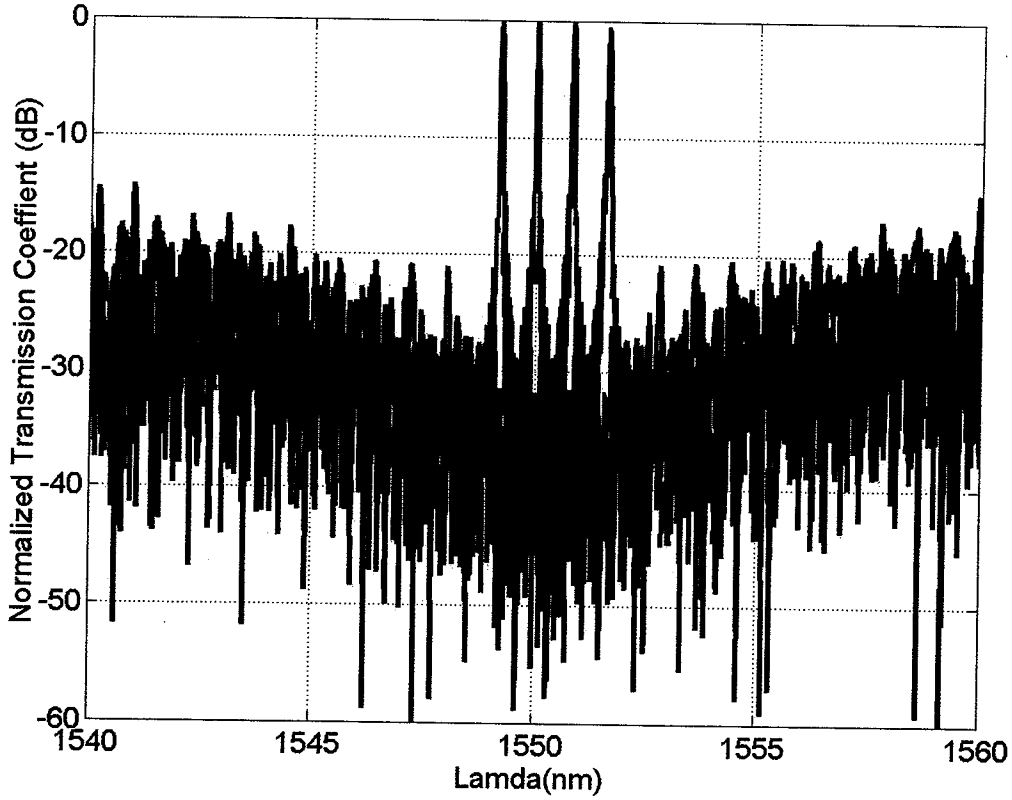

Fig. 3.12. M=200, Max_X=4mm, m=129
(other parameters are same as those used in Fig. 3.6)

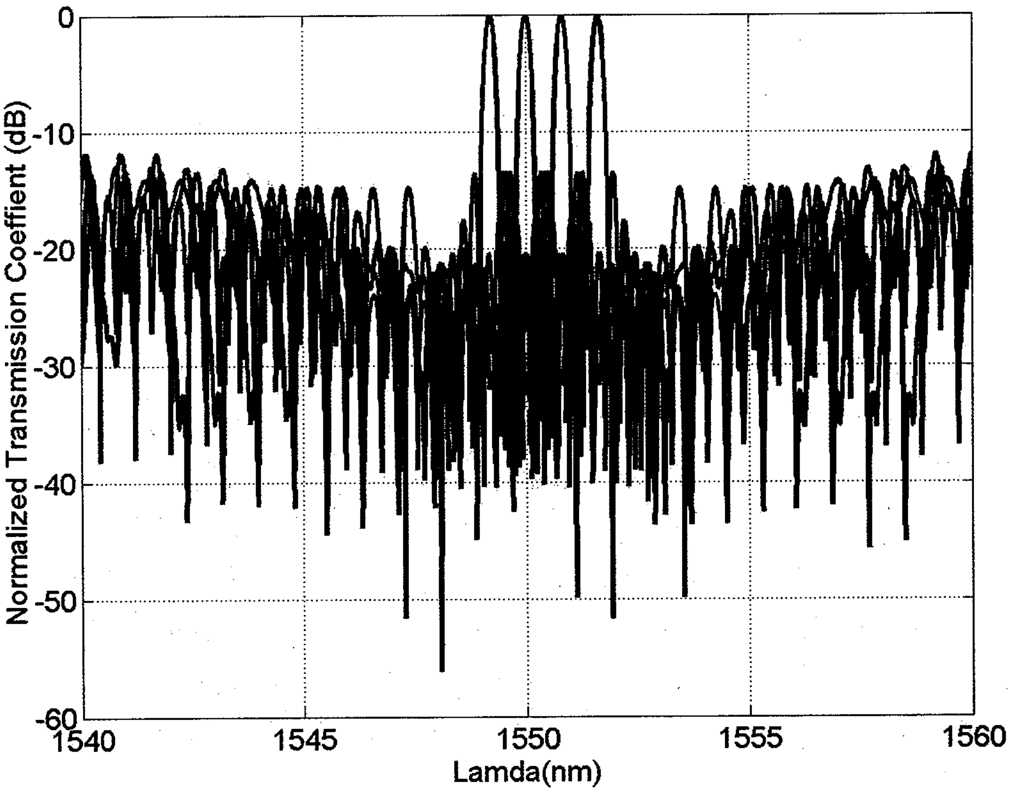

Fig. 3.13. M=50, Max_X=1mm, m=129
(other parameters are same as those used in Fig. 3.6)

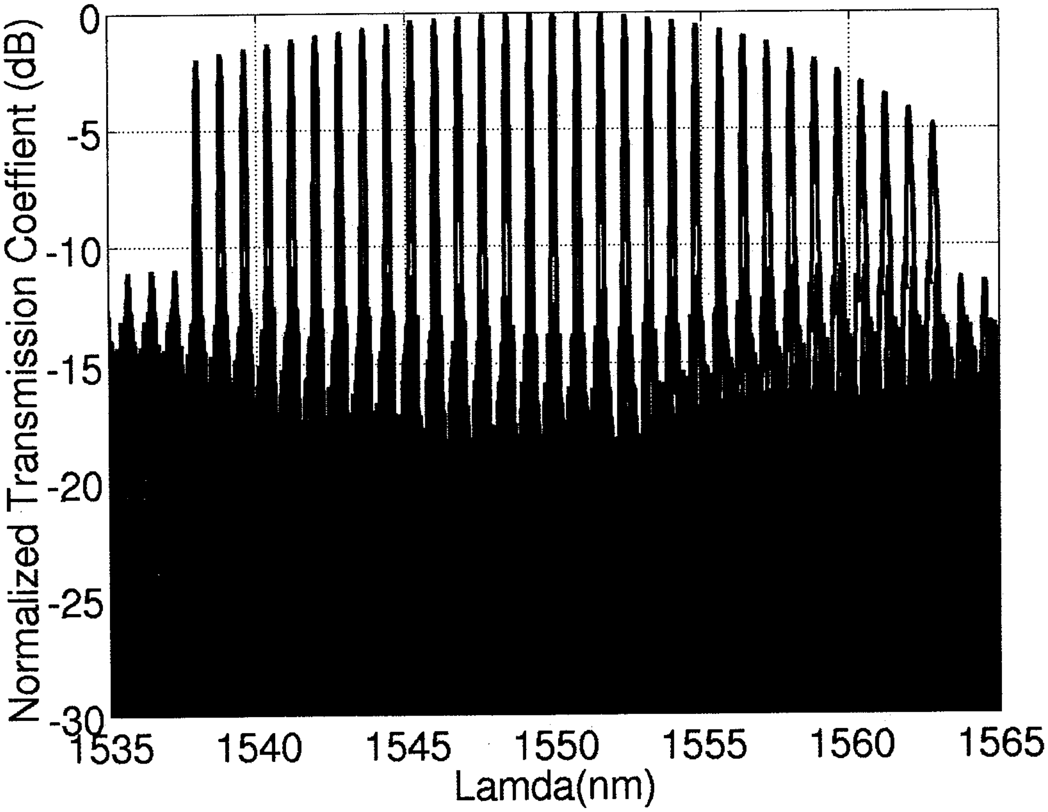

Fig. 3.14. Transmission spectrum for 32 channels with 0.8nm spacing (m=64.5)

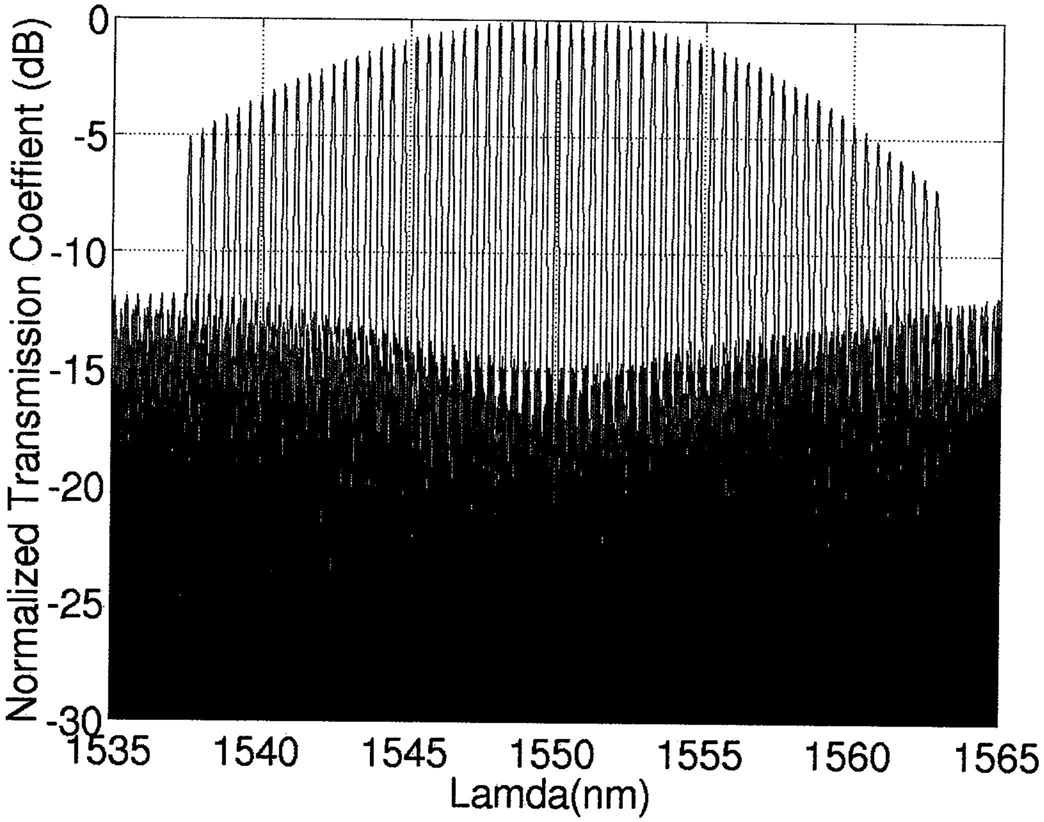

Fig. 3.15. Transmission spectrum for 64 channels with 0.4nm spacing (m=64.5)

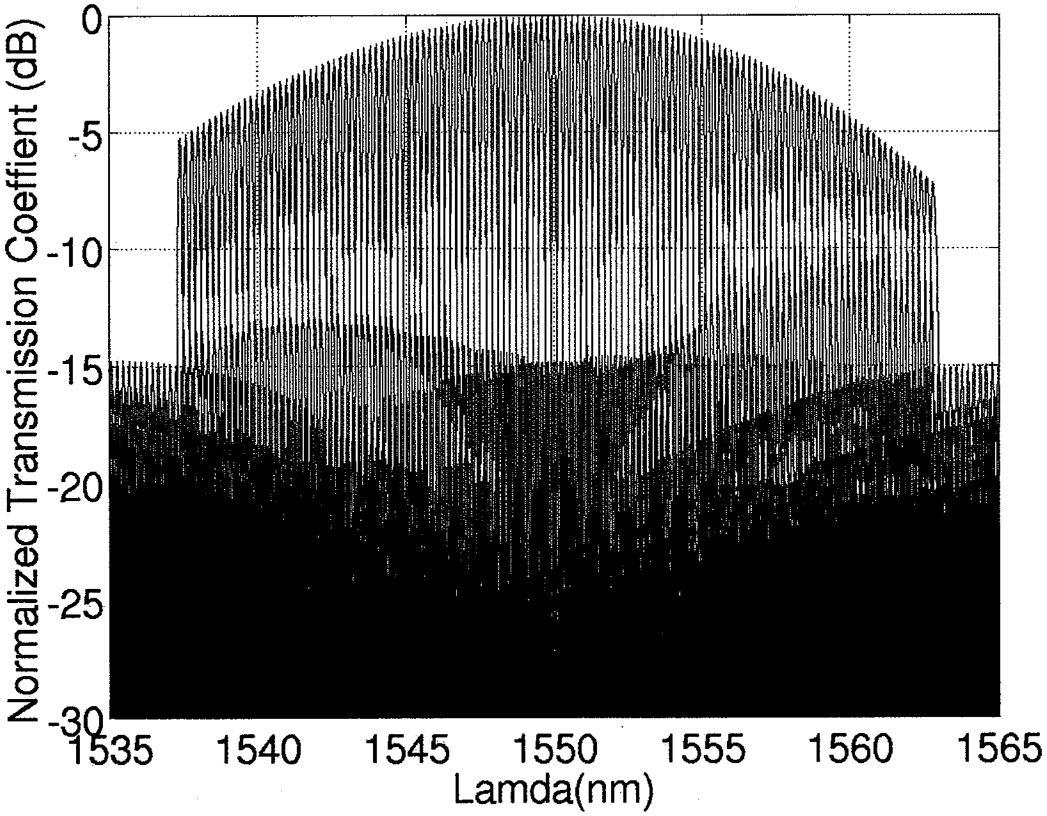

Fig. 3.16. Transmission spectrum for 128 channels with 0.2nm spacing (m=64.5)

4. DESIGN AND SIMULATION OF R-AWG IN *BEAMPROP*

In the previous chapter, we discuss the virtual model of R-AWG by introducing the irregular-sampling zero-crossing (ISZC) method. The simulations based on the virtual model are implemented by Matlab. This chapter focuses on how to generate the data required by the design of our novel device from Matlab simulations and then incorporate the data into the waveguide layout design. Thereafter, beam propagation method (BPM) is utilized to simulate our proposed R-AWG. The design and simulation are accomplished by making use of BeamPROP, a research and development oriented software provided by Rsoft Inc.

4.1 Design Method for R-AWG

4.1.1 Introduction to BeamPROP 4.0 and BeamPROP^{TM} AWG Utility 2.1

BeamPROP is a highly integrated CAD/simulation program for design of photonic devices and photonic integrated circuits. The software incorporates advanced finite-difference beam propagation techniques for simulation, and a modern graphic user interface for ease of circuit layout and analysis. The main program contains a complete CAD layout system for design of waveguide devices and circuits, and controls simulation features such as numerical parameters, input field, and display and analysis options. The simulation program, which can be executed within the main program or standalone, performs the actual simulation and provides a graphic display of field and other quantities of interest for analysis. The computation core is based on a finite difference beam propagation method. This technique uses finite difference methods to solve the well-known parabolic or paraxial approximation of Helmholtz equation. In addition, the program uses "transparent" boundary conditions [50].

The included AWG utility is intended to allow the users of BeamPROP to more easily set up the design and simulation of arrayed waveguide grating (AWG) devices. The utility is broken into two parts: the WDM Router Layout Utility and the WDM Router Simulation Utility. The WDM Router Layout Utility designs the input and output star coupler for the simulation. It also designs two comprehensive layouts for mask exporting purpose only. The Router Simulation Utility sets up the simulation of AWG including the two star couplers by creating a series of script files to run the simulations. First, the input star coupler is simulated by BPM. Next, a program called PHASECOR simulates the phase differences that each arm induces. Finally, the output star coupler is simulated by BPM with the inputs from each of the arrays. A data file and a plot file are then created to show the wavelength response of the AWG.

The lens element that constitutes the body of input star coupler is constructed from the geometry shown in Fig. 4.1, the well-known Rowland circle geometry. The design is essentially identical for the output star, except that the light will be incident on the arc swept by R_o rather than R_i. The body of the star coupler is formed between ARC AB, ARC CD, LINE BC and LINE AD.

The essential part of the array design is that the path length difference between each successive waveguide as designed is rigorously followed. In order to accomplish this, some sort of geometric layout must be introduced so that the arrays can physically align with the star coupler. Some of these designs are shown in Fig. 4.2. The BeamPROP AWG utility generates the design shown in Fig. 4.2(b), as well as an additional design similar to (b) except that the arc is cut in the middle and a straight segment is introduced instead. The details related to these two layouts are left to the next subsection.

4.1.2 Layout geometry for regular AWG

This subsection illustrates the approach that BeamPROP utilizes to design the geometry of conventional devices. As mentioned before, the Design Utility also lays out the entire design for mask purposes using two different designs for the array bends. The utility makes two designs, the full layout and the flat layout that are schematically shown in Fig. 4.3 respectively. The following variables are important with respect to the full router layout:

A	central angle of star couplers with respect to z axis
Rin/Rout	radius of input/output waveguide bends
Rz	minimum radius of arrayed waveguide bends
Lg	length along z of arrayed waveguide structure
Lextra	additional length added to Lg
Lin/Lout	straight length of input/output waveguides
Sin/Sout	lateral separation if input/output waveguides

In the current version, for some parameters the CAD layout can sometimes have a discontinuity between the star couplers and the arrayed waveguides. In this case, it is helpful to add some length to the design (*e.g.* a few 1000 µm). You can do this by changing the variable Lextra (default = 0 µm) or you could also do this by increasing Rz. Note that Li, Sin, Rin, Lin have corresponding output parameters Lo, Sout, Rout, Lout that may be specified independently.

Fig. 4.4 and 5 are the input star coupler and the bottom half of the array; only the first and the i^{th} waveguide (WG) in the array are shown for clarity. Also, the variable definitions are spread between the figures. The key function of the WG array is to progressively increase the path length of each WG by dL from the previous WG. The first WG has a radius of Rz (=zR1) and an initial angle of A0 (=zAa1). Each subsequent WG (M of them), has a radius zRi and an initial angle zAai, where i denotes the i^{th} WG in the array. The path length difference between WG(i) and WG(1) is given by

$$zLi + (zAai \bullet zRi) - (A0 \bullet Rz) = (i-1) \bullet dL/2 \qquad (4.1)$$

where 2 in the denominator is because we are dealing with just the bottom half of the array. This is enforced in the layout by noting that the distance from z=0 to the half-way point of the array must be the same for all the WG's in the array. This is reflected in the following equation:

$$zRi \bullet \sin(zAai) + (\mathrm{Re}\,nd + zLi) \bullet \cos(zAai) = Rz \bullet \sin(A0) + \mathrm{Re}\,nd \bullet \cos(A0) \qquad (4.2)$$

where $Rend = Ro + Lo$. Since Rz is a design variable and A0 is based on the design variables Do and M, and also on Ro, which is calculated from design variables, the right-hand side of Eq. (4.2) is known. From Eq. (4.1) and (4.2), expressions can be generated for zLi and zRi. Some algebraic manipulation is needed to get the final forms of these expressions that are used in the router layouts generated by BeamPROP. Some intermediate variables are also used to facilitate these manipulations.

4.1.3 Design data generation

Our proposed R-AWG still follows the basic structure of conventional AWG. It also consists of three parts, the input star coupler, an array of waveguide grating, and the output star coupler. The locations of the I-O waveguides and the arrayed waveguides are also based on the Rowland circle construction. Nevertheless, the structure difference between conventional AWG and our R-AWG are as follows:

First, the positions of the arrayed waveguides in conventional device are uniformly distributed on the Rowland circle. However, they are nonuniformly distributed in our proposed device. Second, in conventional device, the phase differences between propagation through adjacent arrayed waveguides are identical ($2m\pi$, m is a constant defined as diffraction order) since the lengths of arrayed waveguides follow the equation $L_k=L_c+\Delta L\times(k-1)$. In contrast, m is variant in our devices, even though the zero-crossing property makes sure that they are still multiple times of 2π. Accordingly, the length differences of neighboring waveguides are also varying. That is the reason why only average diffraction order can be meaningful and defined in random AWG.

It is shown that the waveguide layout design method for regular AWG is still applicable in our case. The design equations Eq. (4.1) and (4.2) can be used if we feed them with our own design information, and solve for the corresponding values of zLi and zRi for our own layout. Two types of design data are basically required, the arrayed waveguide locations zAai and their physical length differences dLi (in conventional devices, *dLi=(i-1)*dL*).

In our approach, locations zAai can be obtained via values of x_i (i=1..M) from the Matlab simulation by changing them into angular displacements. As for the physical (real) arrayed waveguide length differences dLi, we transfer the phase of each path in the virtual model into the phase induced by each arrayed waveguide in our devices. In other words, the designed physical lengths Li are calculated by making sure the corresponding optical lengths in the virtual model and real device are equivalent:

$$n_s \cdot r_{ci} + n_s \cdot r_{oi} + \delta \cdot x_i = n_s \cdot L_i, \qquad i = 1..M \tag{4.3}$$

Here the key operation is the equivalent phase transfer from virtual model into real structure. Eq. (4.3) is schematically shown in Fig. 4.6. Actually the left-hand side of Eq. (4.3) has included the information of x_i, as well as its corresponding spherical phase term, and linear phase term. Therefore the function of irregularly-sampling zero-crossing method is automatically incorporated into the real device by this procedure. Furthermore, the most important information is not the absolute values of waveguide lengths, but the length differences among arrayed waveguides instead. They are simply obtained by Eq. (4.4) below:

$$dL_i = L_i - L_1 \tag{4.4}$$

Please note that dL_i does not maintain a linear relationship with respect to the index i as in the conventional AWG device. Besides the simulation results, our Matlab code will also generate two .txt files for zAai and dL_i respectively.

4.1.4 Design process

Now the task is to design our own waveguide layout by modifying and then employing the BeamPROP^{TM} AWG Utility Version 2.1, according to the design data generated by our Matlab codes.

In BeamPROP^{TM} AWG Utility Version 2.1, an executable file called STARGEN.exe is included for users' convenience. The STARGEN utility is used to generate a CAD file for the input and output couplers, as well as the two full router layouts. This executable file can be used from MS-DOS prompt or run line in MS-Windows. The C source code stargen.c is also given. Intensive work has been done to make modifications to stargen.c to meet our needs. The modified stargen.c should function as reading the two .txt data files (for zAai and dL_i), using them for the design by solving Eq. (4.1) and (4.2) for zLi and zRi, and then generating the layout .ind files accordingly.

It should be noted that the layout design, whether in regular device or our novel device, poses very rigorous limitation to the parameter values that are used to define the structure, such as the star coupler radii, the diffraction order, the angular distance between adjacent waveguides on the Rowland circle, etc. For regular AWG, BeamPROP can automatically select appropriate values to meet the requirements. The design parameters for our proposed R-AWG should be very close to those for the regular AWG if the two are made to be operating at the same conditions. Otherwise some problems arise and the layout design fails. Therefore, the basic structure parameters should be extracted from the regular AWG design at first, and then put into our design process. For example, the default value of diffraction order m in original BeamPROP program is set to 40. Here for the modified design method, we still keep this value unchanged throughout our design and simulation for the random AWG as it is very reasonable in terms of fabrication techniques.

As a brief summary, the basic procedures of our design are shown below, taking an example of AWG consisting of one input waveguide, 64 output waveguides, 200 arrayed waveguides, which is for routing 64 wavelength channels centered at 1550 nm and spaced by 0.8nm.

Step1: Using original BeamPROP Utility program for conventional device design

The WDM Router Layout Utility can be opened by selecting **Utility/WDM Router Layout…** from the top menu of the *BeamPROP* CAD window. When this is selected, a dialog window will come up. This window allows the user to create the layout of the AWG device. After we fill in the boxes with those design parameters mentioned above, the Utility would then generate the structures for the input star coupler, the output star coupler, the full layout of the array, the flat layout of the array. The design results are shown in Fig. 4.7.

Step2: Running Matlab program for preliminary simulation results and design data files

Some important structure parameters of the conventional device designed above are extracted and then put into our Matlab codes. The program simulates the virtual model using our NSZC method, as well as bridges the virtual model with real device by generating some data files that are required by the next step.

Step3: Using modified BeamPROP Utility program for our proposed device R-AWG

The modified stargen.exe will read the data files from Matlab codes, and then generate the structures (index files) for the input coupler, output coupler and full layout of the array of R-AWG. The designed layout is shown in Fig. 4.8.

4.2 Simulation Techniques and Results

4.2.1 Overview of the simulation procedures

Once the design files (.ind layout files) have been created, the proposed devices can be simulated. This is done in several steps. First the simulation scripts need to be created. The scripts run the following automated tasks:

1. The Input Star Coupler is simulated and a mode list file is outputted
2. The mode list file is modified due to the arrays by PHASECOR.exe.
3. The new mode list file is converted to a field file by FIELDGEN.exe.
4. The new field file is launched into the output star coupler.
5. The output star coupler is simulated by appropriate BPM method.
6. The last line of the monitor file is extracted by TAILMON.exe and this piece of data is appended onto a data file.
7. WinPLOT is called at the end of a wavelength scan and the data file is plotted and displayed.

The WDM Router Simulation Utility can be accessed by going to the top menu of *BeamPROP* and selecting **Utility/WDM Router Simulation...** When this is selected, a dialog box will come up. When we fill in the appropriate values and click ok, the automatic simulation task will be running. A key program of the simulation utility is an executable file PHASECOR.exe used in step 2. The Phasecor program simulates the phase change in the arrayed waveguide part. By default, the phase change has the two following parts:

(1) Phase correction due to the fact that in BeamPROP the simulation ends at constant Z position. Therefore, for each output array waveguide(i) at the output end of input star coupler with x coordinate and angle a (in reference to z axis), the correction is: DeltaZ(i)=x × (1-cos(a))/sin(a) (the assumption made here is that every waveguide

converges to a point with x=0, z=arbitrary). And this correction needs to be taken into account twice as same correction is needed for 2nd star coupler.

(2) Constant path length difference DL between adjacent paths

Combine (1) and (2), total phase change for ith path should be Phasechange(i)= (2pi/lambda)×Neff(lambda)×(DL×(i-1)-DeltaZ(i)×2). Phasecor will take the output mode list file from first star coupler, make the above phase changes, then create the mode list file for the input of the second star coupler.

The above simulation method is applied to the regular AWG that is designed in subsection 4.1.4 and shown in Fig. 4.7. The result is shown in Fig. 4.9.

4.2.2 Simulation approach and results for the R-AWG

Actually the above description is for the regular device. Due to the particular irregular structure, some changes should be made to implement the simulation of R-AWG. In the BeamPROP simulation utility, a user-defined file known as Design Info could be incorporated into the simulation according to user requirement. This field allows the user to specify additional design information in the WDM router simulations. This information includes the following: (1) extra power correction per arm (transmission, as power fraction); (2) extra phase change per arm (Phi, in degrees); (3) extra path length difference per arm (dL, in μ m). Such information does not replace, but adds to what BeamPROP would normally compute internally for each of these parameters to match the usual design goals and/or impairments. Defining a data file with such information, and specifying this data file in the dialog activates this feature. Besides the data file for the layout design, the Matlab codes also generates the data file for the simulation according to the format of this type of data files. Please note that the BPM is not applied in the simulation of the arrayed waveguide region in both devices. In our simulation, the Phasecore.exe combined with the data file does the simulation work to the array while in regular simulation only the Phasecore.exe does. The simulation result of our example device illustrated in subsection 4.1.4 and shown in Fig. 4.8 is given in Fig. 4.10.

The two simulation results for regular and our new device as shown in Fig. 4.9 and 4.10 respectively can be compared. In Fig. 4.9, some wavelength channels are unfortunately overlapped with other wavelengths of adjacent order. The crosstalk values in those output ports with signal overlaps are intolerable. There is, however, no such problem in our device even though the crosstalk property is worse than the regular one.

Geometric Parameters for Star Coupler

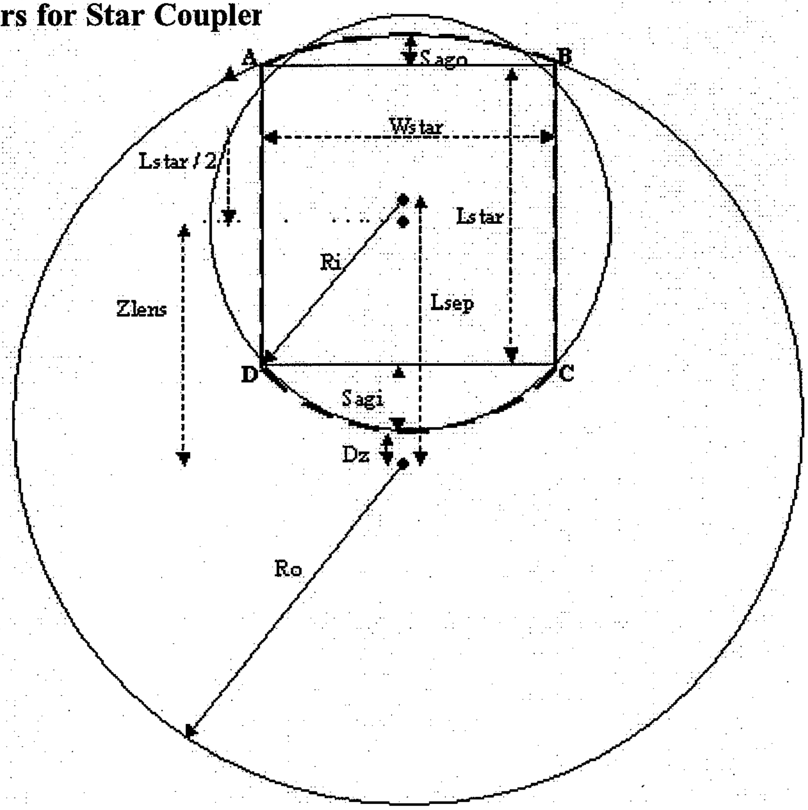

Fig. 4.1. Rowland Circle Geometry

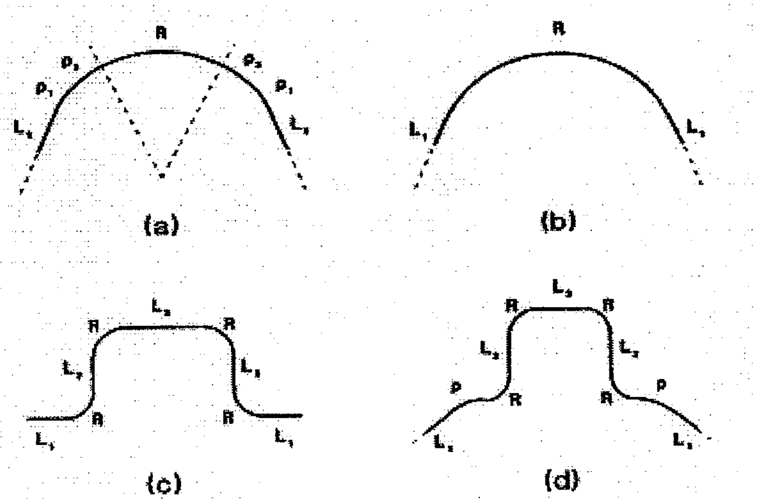

Fig 4.2. Examples of Layout Methods for Array Waveguides

Arrayed Waveguides
Two constraint options are generated when the layout is specified. Design, and some internal, parameters are shown. Parameter specifications are symmetric about cross section at the z midpoint, although their values may be different between the input and output sides. Parameters with a '1' on the end apply to only the 1st waveguide in the array. Similar parameters exist for the other waveguides as well.

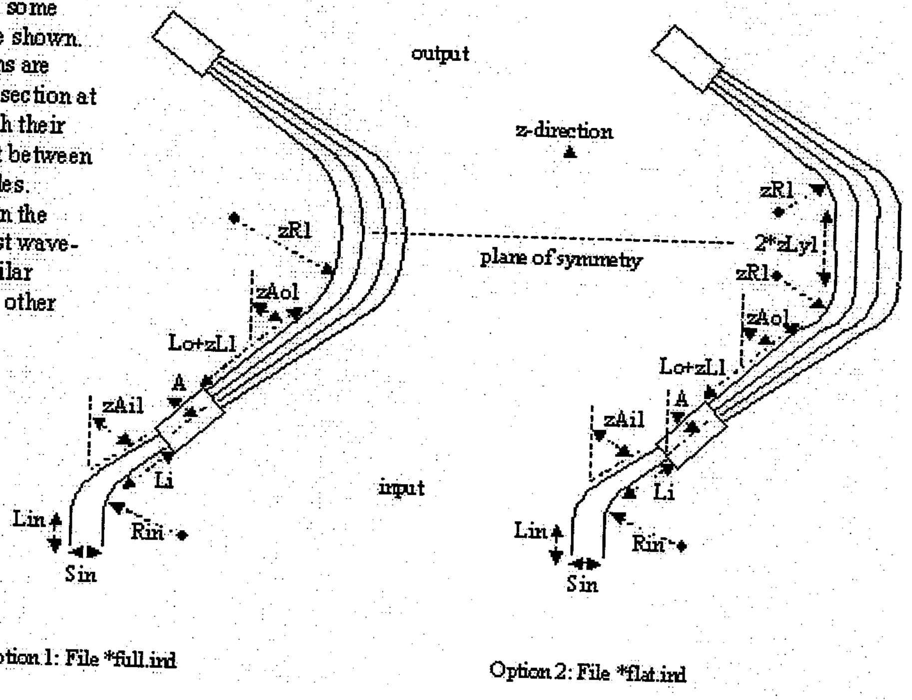

Option 1: File *full.ind

Option 2: File *flat.ind

Fig. 4.3. Layouts for Arrayed Waveguides

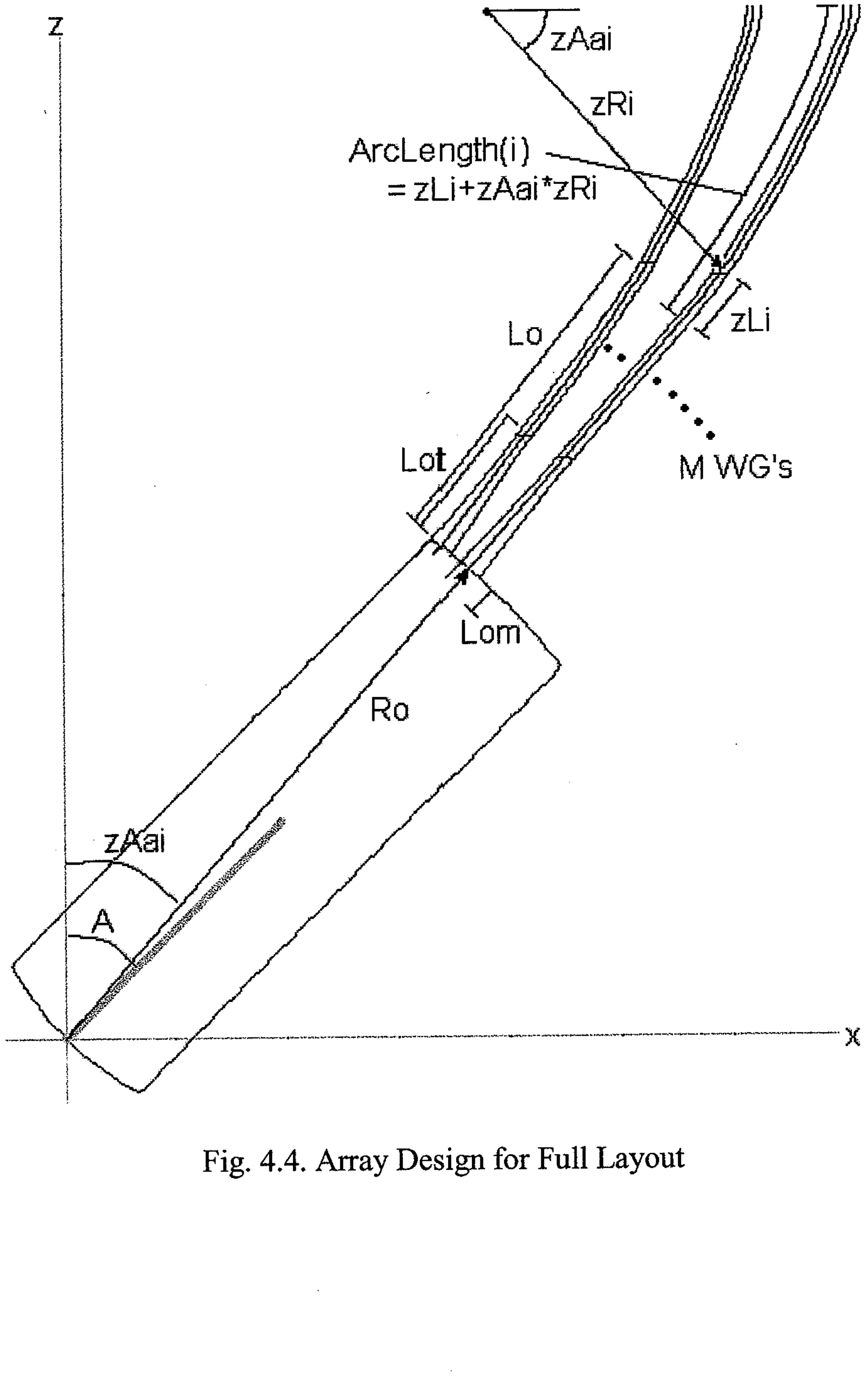

Fig. 4.4. Array Design for Full Layout

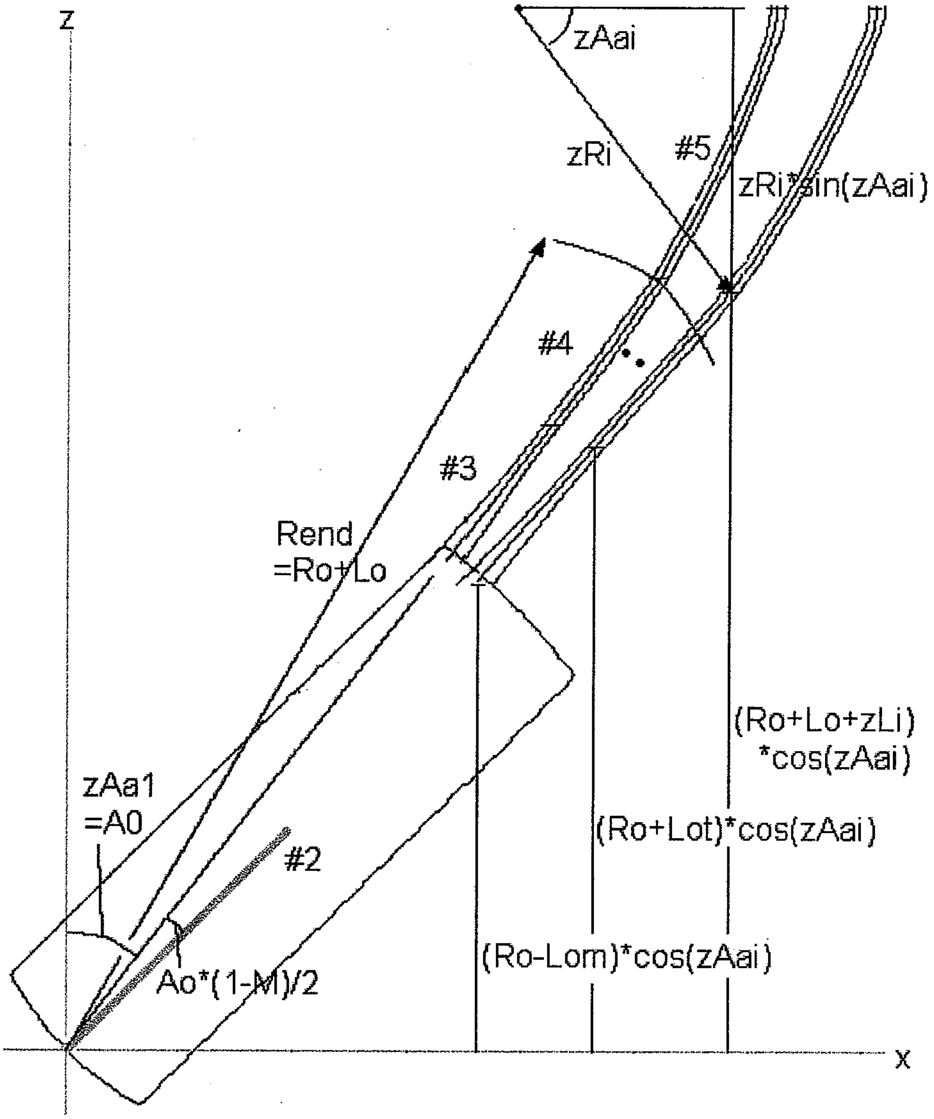

Fig. 4.5. Array Design for Full Layout

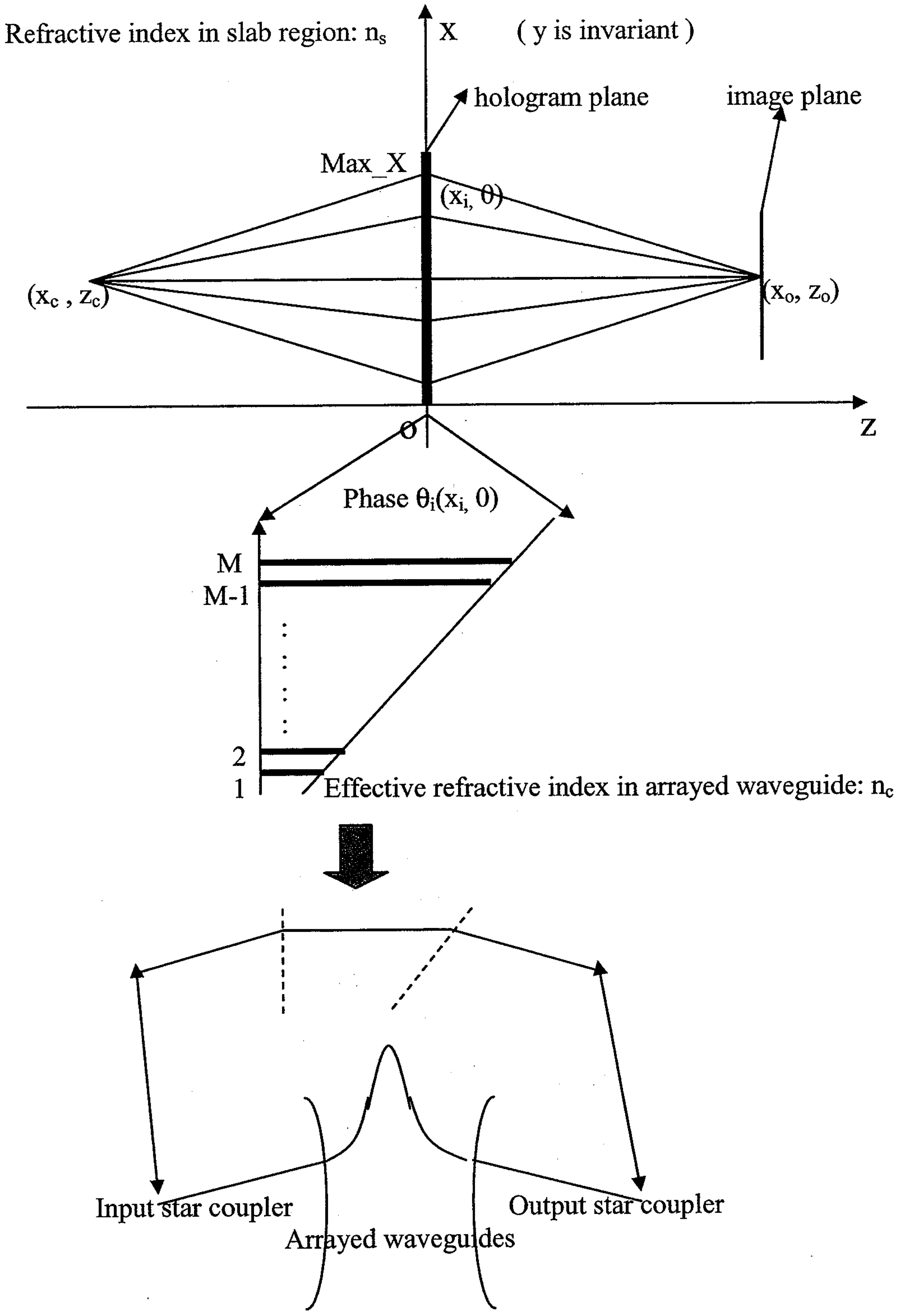

Fig. 4.6. Equivalent phase transfer from virtual model to real structure

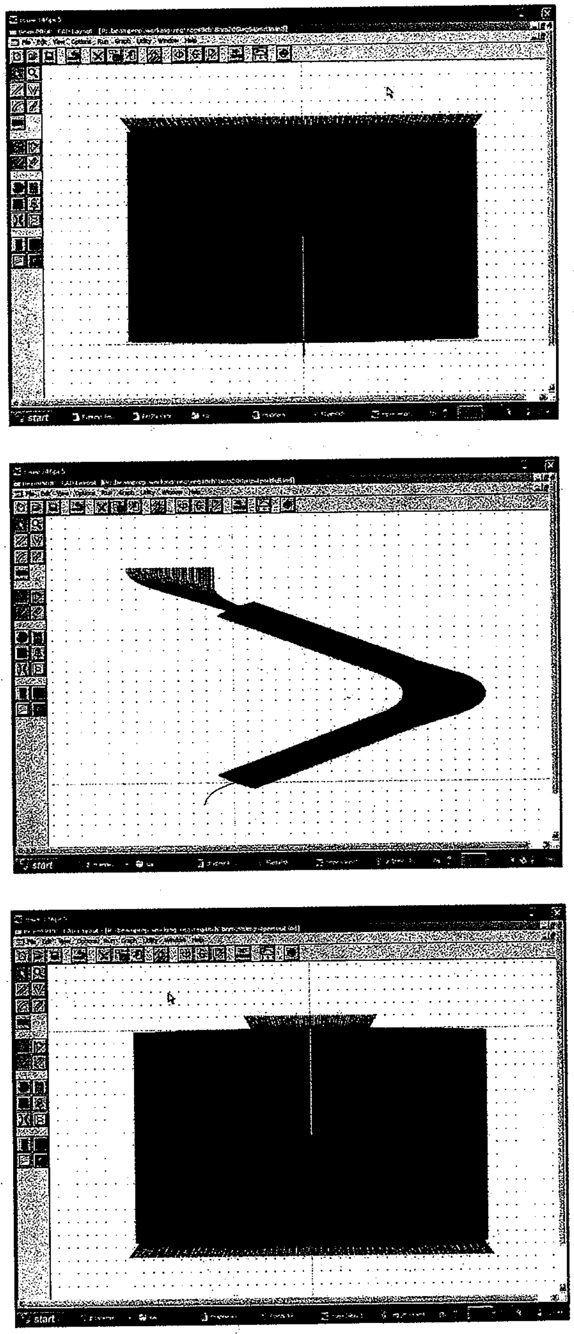

Fig. 4.7. Layout design for 64-channel regular AWG (m=40)
Input star coupler, arrayed waveguides, output star coupler

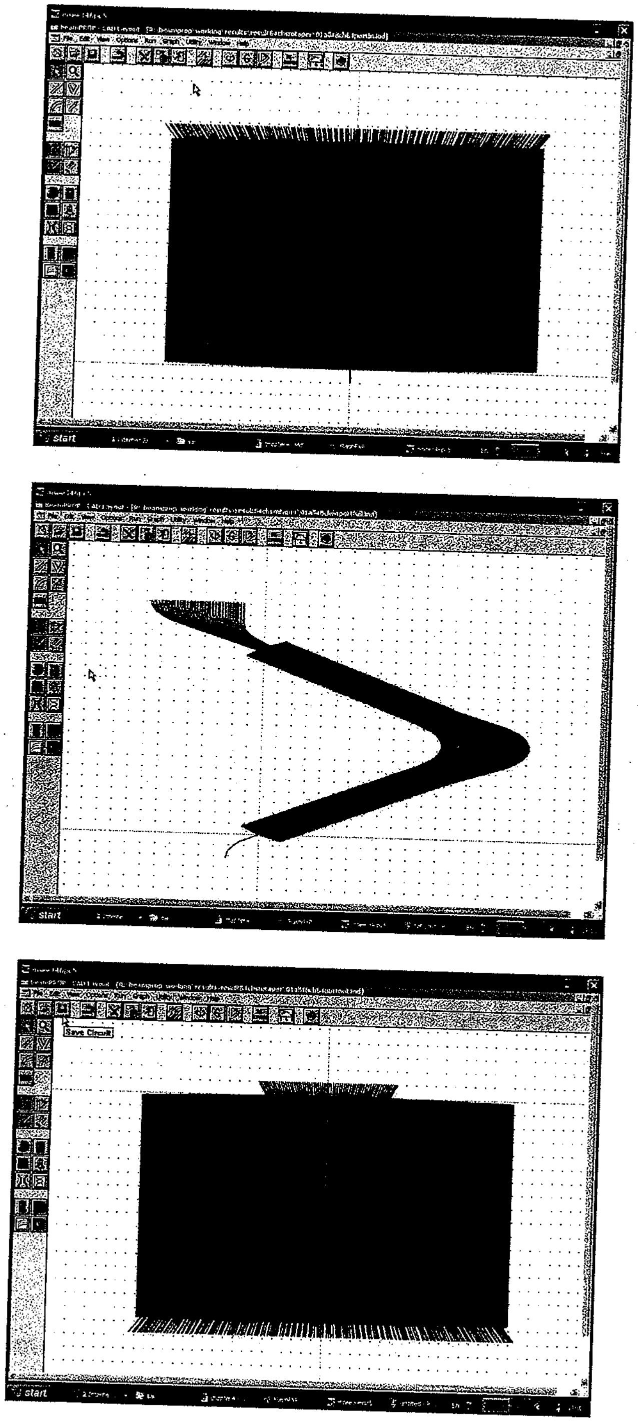

Fig. 4.8. Layout design for 64-channel random AWG (m=40)
Input star coupler, arrayed waveguides, output star coupler

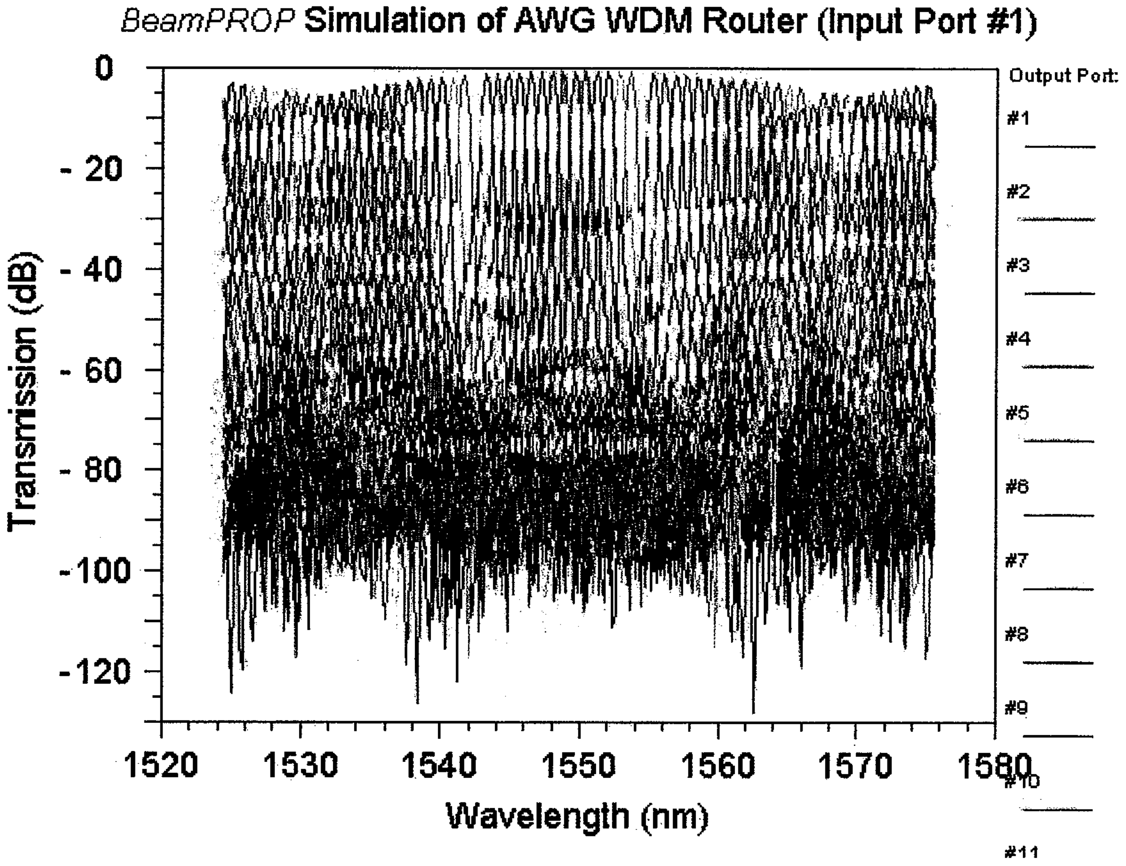

Fig 4.9. Simulation result for the regular AWG in Fig. 4.7 (m=40)

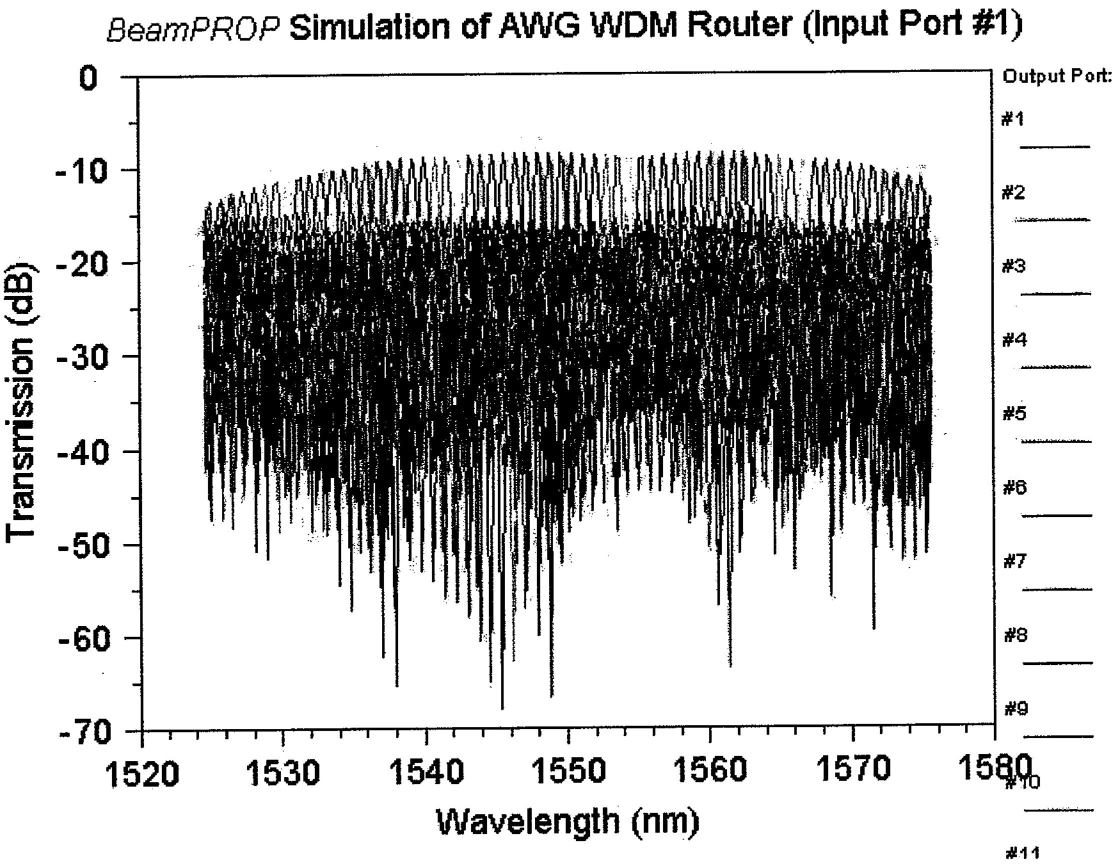

Fig 4.10. Simulation result for the random AWG in Fig. 4.8 (m=40)

5. ANALYSIS AND APPLICATION IN THREE-DIMENSIONAL GEOMETRY

In this chapter, our virtual model is extended to the three-dimensional (3D) case. That is, the sampling points are arranged on a 2D plane with both x and y coordinates varying, instead of on a 1D plane (only x coordinates are varying) in the previous discussion. The basic picture is almost the same as before, however, changed into a 3D version. We made slight changes to our irregular-sampling zero-crossing method to incorporate the y-related variables. At first we still choose the sampling points (the corresponding positions of waveguides) within many evenly divided rectangular grids in a semi-random manner. Then the alternative method of phase generation is applied to calculate the exact phase needed for zero-crossing points. The remaining question is how to realize the exact phases for each point in practice.

5.1 Dispersion Relations

The general equation used in the 3D model is given as

$$k_s r_{ci} + k_c (l_0 + x_i \alpha_x + y_i \alpha_y) + k_s r_{oi} = 2q\pi + \varphi_0 \tag{5.1}$$

Making use of paraxial approximations, we get

$$\begin{aligned} r_{oi} &= \sqrt{(x_0 - x_i)^2 + (y_0 - y_i)^2 + z_0^2} = z_0 + \frac{x_0^2 + x_i^2}{2z_0} - \frac{x_0 x_i}{z_0} + \frac{y_0^2 + y_i^2}{2z_0} - \frac{y_0 y_i}{z_0} \\ r_{ci} &= \sqrt{(x_c - x_i)^2 + (y_c - y_i)^2 + z_c^2} = z_c + \frac{x_c^2 + x_i^2}{2z_c} - \frac{x_c x_i}{z_c} + \frac{y_c^2 + y_i^2}{2z_c} - \frac{y_c y_i}{z_c} \end{aligned} \tag{5.2}$$

Substituting Eq.(5.2) into Eq.(5.1) and neglecting constant phase terms result in

$$x_i \delta_x - n_s x_i (\frac{x_c}{z_c} + \frac{x_o}{z_o}) + n_s \frac{x_i^2}{2} (\frac{1}{z_0} + \frac{1}{z_c}) = q_x \lambda \tag{5.3}$$

$$y_i \delta_y - n_s x_i (\frac{y_c}{z_c} + \frac{y_o}{z_o}) + n_s \frac{y_i^2}{2} (\frac{1}{z_0} + \frac{1}{z_c}) = q_y \lambda \tag{5.4}$$

where

$$\delta_x = n_c \alpha_x, \delta_y = n_c \alpha_y \tag{5.5}$$

It should be noted that Eq.(5.3) and (5.4) must be satisfied for each arrayed waveguide. Now they are applied to another wavelength λ', the focus of which is $(x_0', y_0'\ z_0')$.

$$x_i \delta - n_s x_i \left(\frac{x_c}{z_c} + \frac{x_o'}{z_o'}\right) + n_s \frac{x_i^2}{2}\left(\frac{1}{z_o'} + \frac{1}{z_c}\right) = q_x \lambda' \tag{5.6}$$

$$y_i \delta - n_s y_i \left(\frac{y_c}{z_c} + \frac{y_o'}{z_o'}\right) + n_s \frac{y_i^2}{2}\left(\frac{1}{z_o'} + \frac{1}{z_c}\right) = q_y \lambda' \tag{5.7}$$

Taking ratio of two pairs of equations for x-direction and y-direction, respectively, we can get:

$$\frac{x_i \delta - n_s x_i \left(\frac{x_c}{z_c} + \frac{x_o'}{z_o'}\right) + n_s \frac{x_i^2}{2}\left(\frac{1}{z_o'} + \frac{1}{z_c}\right)}{x_i \delta - n_s x_i \left(\frac{x_c}{z_c} + \frac{x_o}{z_o}\right) + n_s \frac{x_i^2}{2}\left(\frac{1}{z_o} + \frac{1}{z_c}\right)} = \frac{\lambda'}{\lambda} = r \tag{5.8}$$

$$\frac{y_i \delta - n_s y_i \left(\frac{y_c}{z_c} + \frac{y_o'}{z_o'}\right) + n_s \frac{y_i^2}{2}\left(\frac{1}{z_o'} + \frac{1}{z_c}\right)}{y_i \delta - n_s y_i \left(\frac{y_c}{z_c} + \frac{y_o}{z_o}\right) + n_s \frac{y_i^2}{2}\left(\frac{1}{z_o} + \frac{1}{z_c}\right)} = \frac{\lambda'}{\lambda} = r \tag{5.9}$$

The new focal point $(x_0', y_0'\ z_0')$ is obtained by solving the above equations and noticing that they should be satisfied for any x_i:

$$z_o' = \frac{1}{\dfrac{r-1}{z_c} + \dfrac{r}{z_o}}$$

$$x_o' = \frac{r\dfrac{x_o}{z_o} - (r-1)(\dfrac{\delta_x}{n_s} - \dfrac{x_c}{z_c})}{\dfrac{r-1}{z_c} + \dfrac{r}{z_o}}$$

$$y_o' = \frac{r\dfrac{y_o}{z_o} - (r-1)(\dfrac{\delta_y}{n_s} - \dfrac{y_c}{z_c})}{\dfrac{r-1}{z_c} + \dfrac{r}{z_o}}$$

(5.10)

If we assume that $\frac{r-1}{z_c} << \frac{r}{z_o}$, (5.11)

Eq.(5.10) can be simplified as

$$z_o' = \frac{z_o}{r}$$
$$x_o' = x_o - z_o \frac{r-1}{r}(\frac{\delta_x}{n_s} - \frac{x_c}{z_c}) \qquad (5.12)$$
$$y_o' = y_o - z_o \frac{r-1}{r}(\frac{\delta_y}{n_s} - \frac{y_c}{z_c})$$

The above derivations show that the focal point z-coordinates of different wavelengths are very close to z_o. In other words, the focal points for different wavelength components tend to be on the same vertical image plane perpendicular to the z-direction, as we want for the output waveguide arrangement. On that image plane, the dispersion relation in x-direction can be obtained as

$$\Delta x = x_o' - x_o = -z_o \frac{r-1}{r}(\frac{\delta}{n_s} - \frac{x_c}{z_c})$$
$$= -z_o \frac{\lambda' - \lambda}{\lambda'}(\frac{\delta}{n_s} - \frac{x_c}{z_c}) \approx -z_o \frac{\Delta\lambda}{\lambda}(\frac{\delta}{n_s} - \frac{x_c}{z_c}) \qquad (5.13)$$
$$\frac{\Delta x}{\Delta\lambda} = -z_o \frac{1}{\lambda}(\frac{\delta_x}{n_s} - \frac{x_c}{z_c})$$

Similarly, the dispersion relation in y-direction can be obtained as

$$\frac{\Delta y}{\Delta \lambda} = -z_o \frac{1}{\lambda}\left(\frac{\delta_y}{n_s} - \frac{y_c}{z_c}\right) \tag{5.14}$$

Two diffraction orders, both in x-direction and y-direction are defined in a similar way as

$$m_x = \delta_x \frac{\Delta x_i}{\lambda_0} \quad , \quad m_x = \delta_x \frac{\Delta x_i}{\lambda_0} \tag{5.15}$$

5.2 Method of Irregularly-Sampled Zero-Crossings Method in 3D

Algorithm 1

The whole holography plane is divided into small square regions (grids) whose dimensions are identical. In each grid, one initial point is chosen randomly by following a rule that its x-coordinate and y-coordinate are random variables that have uniform distribution in the corresponding x-interval and y-interval of that region, respectively. In other words, x-coordinates and y-coordinates should be independently identically distributed random variables (i.i.d.r.v.) except that their expected values are equally spaced. Afterwards, the chosen point is moved to a nearby point that is zero-crossing point.

Algorithm 2

An alternative algorithm of phase generation is developed and utilized here to transform these initial random sampling points into equivalent zero-crossing points. Instead of moving them by adding a correction displacement, we just give them the required phases with zero-crossing property. The algorithm is very simple. The total phase via the path of each initial point is calculate in 3D space, and then the phase module 2π is compensated for by physically generating the negative phase at each sampling point. Suppose the phase at an aperture point is X. Since $-X$ is equivalent to 2π-X in terms of phase, it can be realized by vertical arrangement of many 2D arrayed waveguide layers or phase generation by computer controlled electron beam scanning method. In practice, current fabrication technologies limit the precision of phase that can be generated and continuous phase generation is not easy to accomplish. Therefore the phase quantization method is usually employed to approximate the exact phase. The technology determines the availability and accuracy of the quantization levels. In principle, the more the quantization levels are available, the more precise the phase generation is, the better focusing and demultiplexing properties we would have.

Below we discuss simulation results both with the ideal case of exact phase and the approximate case of quantized phase, by using algorithm 2.

5.3 Simulation Results

5.3.1 Ideal case (exact zero-crossings)

The algorithm in ideal case is dependent on the assumption that the exact phase can be generated precisely as calculated. Fig 5.1-3 show the focusing and demultiplexing on the image plane (x-y plane of $z=z_o$). All the three simulations are based on 4 wavelengths, 1549.2nm, 1549.6nm, 1550nm, 1550.4nm that are spaced by 0.4nm(50GHz) and a 100×100 array of sampling points on a 2mm×2mm square plane.

Case 1 (Fig. 5.1):

The diffraction coefficient in x-direction δ_x is set to 5 (m_x=64.5), while in y-direction δ_y is zero (m_y=0). The four wavelengths are dispersed in x-direction.

Case 2 (Fig. 5.2):

The diffraction coefficient in y-direction δ_y is set to 5 (m_y=64.5), while in x-direction δ_x is zero (m_x=0). The four wavelengths are dispersed in y-direction.

Case 3 (Fig. 5.3):

The diffraction coefficients in both directions are set to δ_x=5, δ_y=2.5, respectively (m_x=64.5, m_y=32.25). The four wavelengths are dispersed in both x-direction and y-direction.

5.3.2 Real case (phase quantization method applied)

The following simulations are based on the same parameters used in the first simulation (Case 1) except that the phase quantization method is applied instead of exact phase generation.

Case 4 (Fig. 5.4): 4 quantization levels

Case 5 (Fig. 5.5): 16 quantization levels

Case 6 (Fig. 5.6): 256 quantization levels

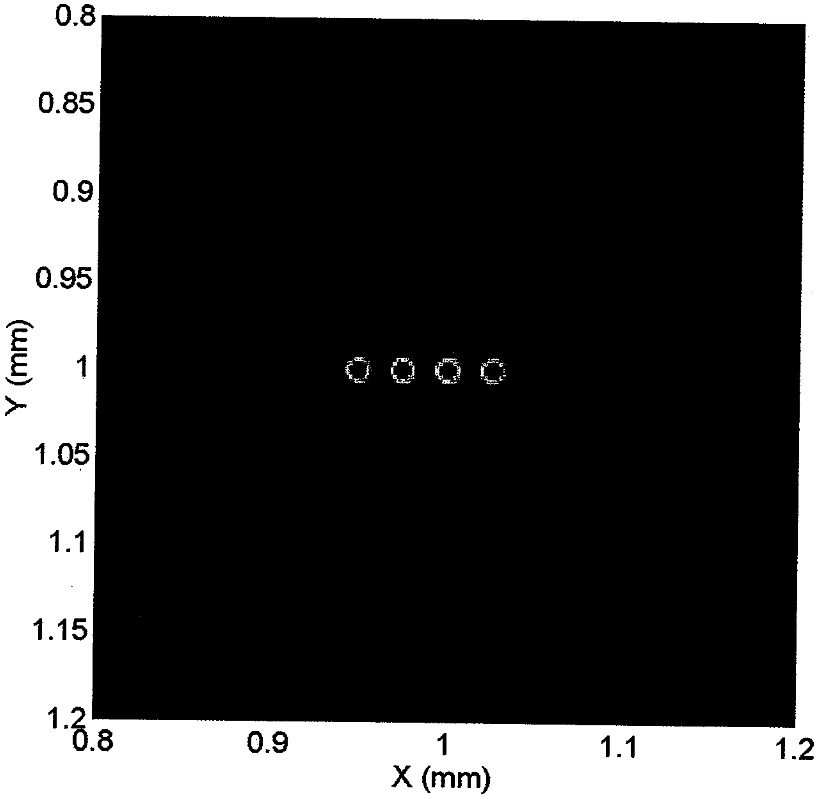

Fig 5.1. 3D model image plane: dispersion in x-direction (exact phase method, m_x=64.5, m_y=0)

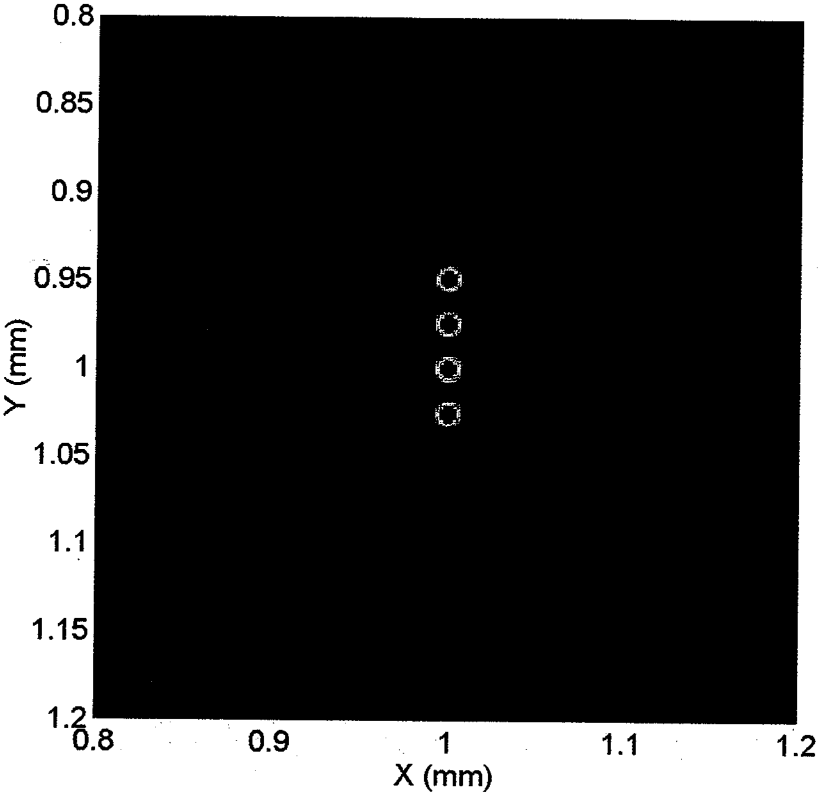

Fig 5.2. 3D model image plane: dispersion in y-direction (exact phase method, m_x=0, m_y=64.5)

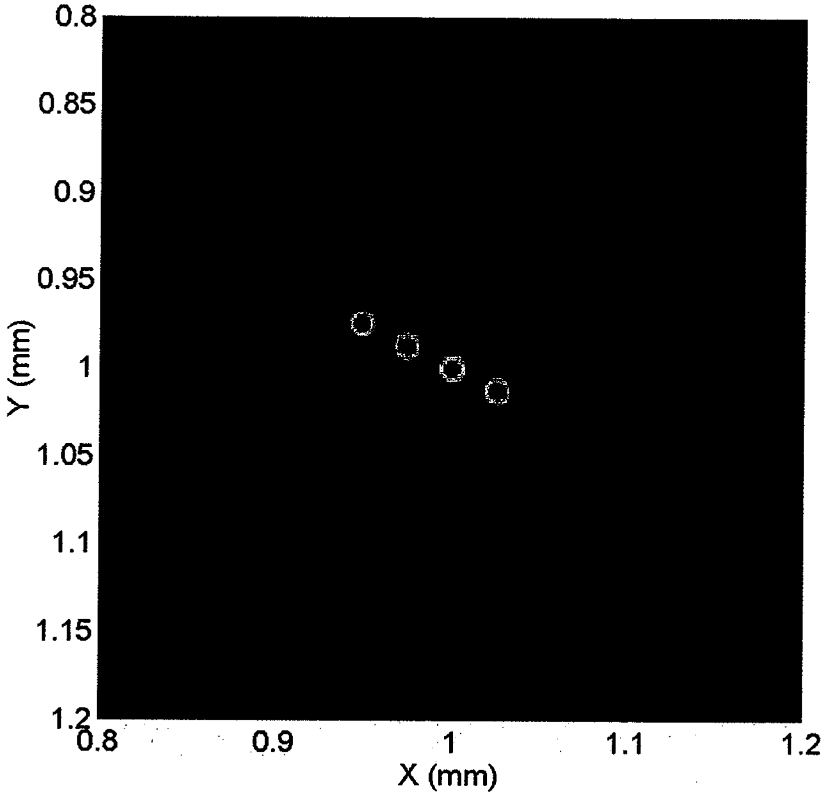

Fig 5.3. 3D model image plane: dispersion in both directions (exact phase method, m_x=64.5, m_y=32.25)

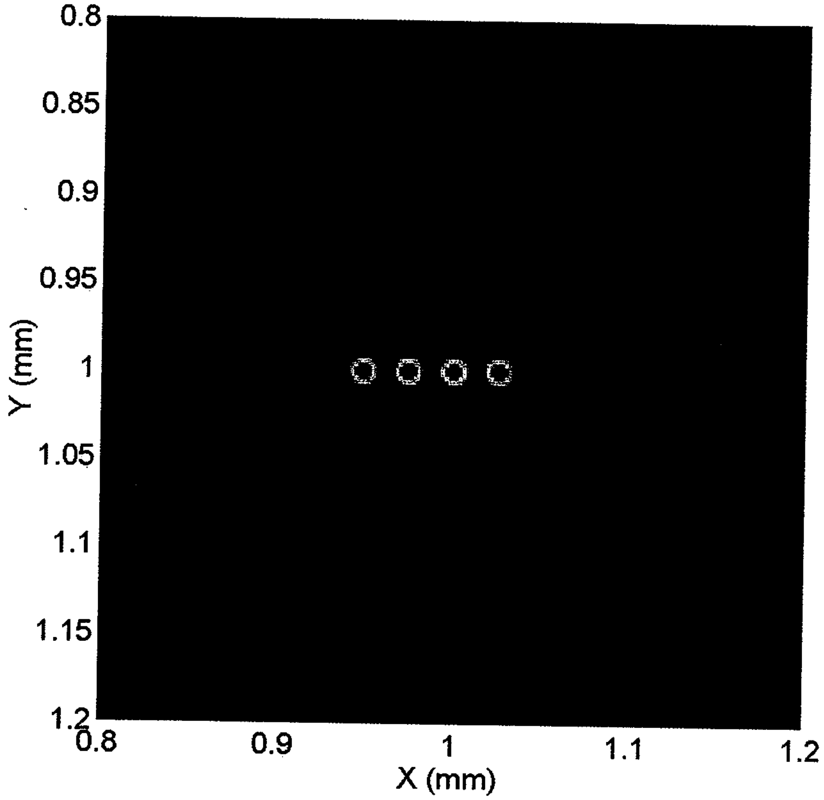

Fig 5.4. 3D model image plane: dispersion in x-directions
(4 quantization levels, m_x=64.5, m_y=0)

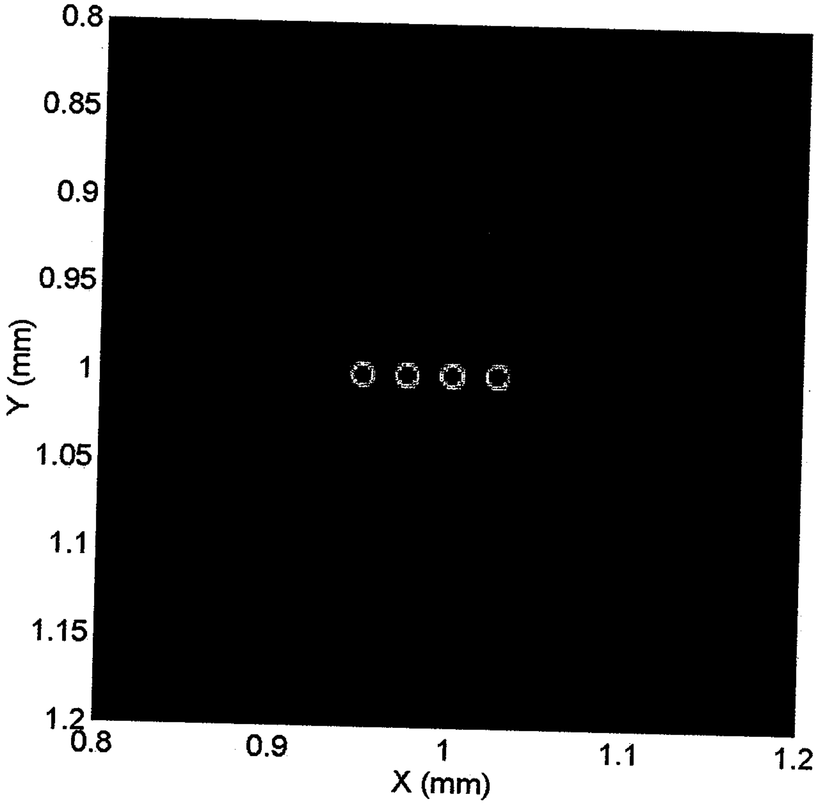

Fig 5.5. 3D model image plane: dispersion in x-directions (16 quantization levels, m_x=64.5, m_y=0)

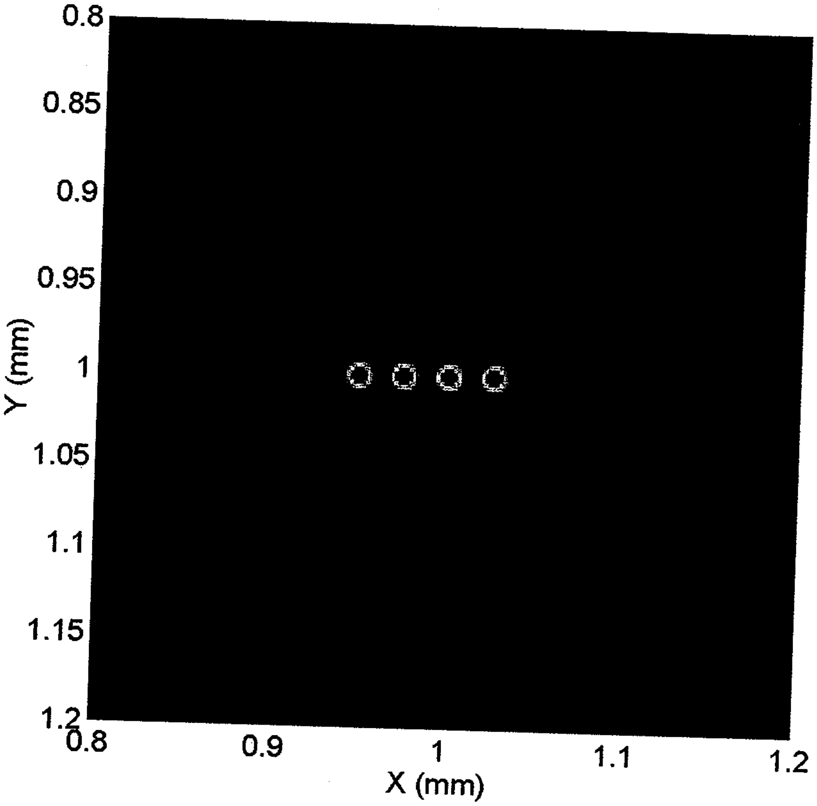

Fig 5.6. 3D model image plane: dispersion in x-directions (256 quantization levels, m_x=64.5, m_y=0)

6. SUMMARY AND FUTURE RESEARCH

The application of phasar-based devices is rapidly broadening. AWG's have proven to be flexible components that support realization of a broad class of functions for use in WDM networks. Silica-based devices offer the best performance and are presently being most widely used. Furthermore, although silica-based waveguides are simple circuit elements, various functional devices are fabricated by utilizing spatial multibeam or temporal multistage interference effects. InP-based devices are most promising for realization of active devices, such as lasers and receivers and, on the long term, for more complicated circuits containing large number of components, such as add-drops and optical crossconnects. The planar lightwave circuits (PLC) technologies supported by continuous improvements in waveguide fabrication, circuit design and device packaging will proceed to a higher level of integration of optics and electronics aiming at the next generation of telecommunication systems.

In this thesis, we first theoretically set up and examine a virtual model for novel demultiplexing devices by combining the ideas of one-image-only digital holography and conventional AWG. The irregular-sampling zero-crossing method is proposed and utilized in the model. The simulations by matlab are done to approximately investigate the performance and properties. Thereafter by employing the Rsoft BeamPROP software, the real device design (including the input star coupler, arrayed waveguide region, output star coupler) is realized based on the virtual model and then the BPM simulation results are obtained.

The novel demultiplexing device we propose here is named as R-AWG. It significantly reduces the undesired order harmonics so that new wavelength channels can be used for operation as being focused onto the freed spots that are no longer occupied by previously used wavelengths. It is exactly where the main advantage lies in. The main tradeoff is that the crosstalk values are higher compared to conventional device because the undesired order harmonics are expected to turn into background noise.

The problem related to insertion loss is not yet fully examined. Our matlab code is based on the most basic principles and simplest model of electromagnetics. It can only approximately deal with the crosstalk since crosstalk property is in a relative manner while insertion loss is in an abstract manner. BeamPROP does offer a way to examine the insertion loss and such effort is being done. Another possible improvement lies in the simulation methods. As mentioned in Chapter 4, BeamPROP and other professional software like Kymata are all treating the arrayed waveguide region as many individual straight waveguides. They are assumed to be straight with no bending loss and be separated enough with no interference. Such effects are more significant in the case of large number of waveguide and complicated layout. The accurate BPM simulation is not used here to take them into account. We are thinking if it is possible to implement BPM simulation to the arrayed waveguide region. The results should be more convincing, the computation load will be intense though.

Some research has been done in the field of irregular phased array in antenna and radar application. Some results from the previous work could possibly be incorporated to improve the performance and reduce the cost. However, our method is not only based on irregular sampling, but also on zero-crossings. Some theoretical approaches such as probabilistic and statistical methods might be helpful for in-depth research on our devices. In other words, the semi-random treatment in our irregular-sampling zero-crossing method might be improved with the results from statistical investigation. And iterative optimization methods are also expected to be useful for the same purpose. It is expected that the major concern of crosstalk and insertion loss could be essentially solved by such efforts.

We are also trying to fabricate our proposed device and characterize it by the experimental results. BeamPROP has the capability to transform the layout design to mask files that are directly useful to fabrication process. The final design can then be send to the fabrication house for manufacturing.

LIST OF REFERENCES

[1] C.A.Brackett, "Dense wavelength division multiplexing networks: Prinples and applications," *IEEE J. Select. Areas Commun.*, Vol. 8, pp. 948-64, 1990.

[2] C.A.Brackett, etc., "A scalable multiwavelength multihop optical network: A proposal for research on all-optical networks," *IEEE J. Lightwave Technol.*, Vol. 11, pp. 736-53, May/June 1993.

[3] H. Toba, "A 100-ch optical WDM transmission/distribution at 622 Mbits/s over 50km," *IEEE J. Lightwave Technol.*, Vol. 8, pp. 1396-1401, 1990.

[4] I.P.Kaminow, "A wideband all-optical WDM network," *IEEE J. Select. Areas Commun.*, Vol. 8, pp. 780-99, 1996.

[5] B.T. Doshi, etc., "Optical network design and restoration," *Bell Labs Technical Journal*, Vol. 4, No. 1, 1999.

[6] Y.Hibino, "Passive optical devices for photonic networks," *IEICE Trans. Commun.*, Vol. E-83B, No. 10, October 2000.

[7] M.A.Scobey and D.E.Spock, "Passive DWDM components using MicroPlasma optical interference filters," *OFC'96 Technical Digest*, pp. 242-43, 1996.

[8] K.O.Hill, etc., "Photosensitivity in optical fiber waveguides: Application to reflector filter fabrication," *Appl. Phys. Lett.*, Vol. 32, pp. 647-9, 1978.

[9] G.Meltz, etc., "Formation of Bragg gratings in optical fibers by a transverse holographic method," *Opt. Lett.*, Vol. 29, pp. 823-5, 1989.

[10] A.M.Vengsarkar, etc., "Long-period fiber-grating-based gain equalizers," *Opt. Lett.*, Vol. 21, pp. 336-8, 1996.

[11] J.J. Refi, "Optical fibers for optical networking," *Bell Labs Technical Journal*, Vol. 4, No. 1, 1999.

[12] K. Okamoto, "Recent progress of integrated optics planar lightwave circuits," *Opt. & Quantum Electron.*, Vol. 31, No. 2, pp. 107-29, Feb. 1999.

[13] M.K.Smit, "New focusing and dispersive planar component based on an optical phased array," *Electron. Lett.*, Vol. 24, No. 7, pp. 385-6, March 1988.

[14] A.R.Vellekoop and M.K.Smit, "Low-loss planar optical polarization splitter with small dimensions," *Electron. Lett.*, Vol. 25, pp. 946-7, 1989.

[15] A.R.Vellekoop and M.K.Smit, "Four-channel integrated-optic wavelength demultiplexer with weak polarization dependence," *IEEE J. Lightwave Technol.*, Vol. 9, No. 3, pp. 310-4, March 1991.

[16] H. Takahashi, etc., "Arrayed-waveguide grating for wavelength devision multi-demultiplexer with nanometer resolution," *Electron. Lett.*, Vol. 26, No. 2, pp. 87-8, Jan. 1990.

[17] H. Takahashi, etc., "10 GHz spacing optical frequency division multiplexer based on arrayed-waveguide grating," *Electron. Lett.*, Vol. 28, No. 4, pp. 380-2, Feb. 1992.

[18] S.Suzuki, etc., "High-density integrated 1×16 optical FDM multi/demultiplexer," LEOS'94, Vol. 2, pp. 263-4, 1994.

[19] P.C.Clemens, etc., "8-Channel optical demultiplexer realized as SiO2/Si flat-field spectrograph," *IEEE Phton. Technol. Lett.*, Vol. 6, pp. 1109-11, 1994.

[20] M.Fallahi, etc., "Grating demultiplexer integrated with MSM detector array in InGaAs/AlGaAs/GaAs for WDM," *IEEE Phton. Technol. Lett.*, Vol. 5, pp. 794-7, 1993.

[21] J.B.D.Soole, etc., "Monolithic InP/InGaAsP/InP grating spectrometer for the 1.48-1.56um wavelength range," *Appl. Phys. Lett.*, Vol. 58, pp.1949-51, 1991.

[22] C. Cremer, etc., "Grating spectrograph in InGaAsP/InP for dense wavelength division multiplexing," *Appl. Phys. Lett.*, Vol. 59, pp. 627-9, 1991.

[23] E.Gini, etc., "Polarization independent InP WDM multiplexer/demultiplexer module," *IEEE J. Lightwave Technol.*, Vol. 16, pp. 625-30, 1998.

[24] J.He, etc., "Monolithic integrated wavelength demultiplexer based on a waveguide Rowland circle grating in InGaAsP/InP," *IEEE J. Lightwave Technol.*, Vol.16, pp. 631-8, 1998.

[25] C.Dragone, "An N×N optical multiplexer using a planar arrangement of two star couplers," *IEEE Photon. Technol. Lett.*, Vol. 3, pp. 812-5, Sept. 1991.

[26] C.Dragone, "Integrated optics N×N multiplexer on silicon," *IEEE Photon. Technol. Lett.*, Vol. 3, pp. 896-9, Oct. 1991.

[27] H.Takahashi, "Transmission characteristics of arrayed waveguide N*N wavelength multiplexer," *IEEE J. Lightwave Technol.*, Vol.13, pp. 447-55, 1995.

[28] M.Kawachi, "Silica waveguides on silicon and their application to integrated components," *Opt. & Quantum Electron.*, Vol. 22, pp. 391-416, 1990.

[29] M.K.Smit and C.V.Dam, "Phasar-based WDM-devices: principles, design and applications," *IEEE Selected Topics in Quantum Electronics*, Vol. 2, No. 2, 1996.

[30] H.Bissessur, ect., "Small size, polarization-independent phased array demultiplexers on InP," *Electron. Lett.*, Vol. 31, No. 24, pp. 2118-20, Nov. 1995.

[31] H.Bissessur, etc., "Extremely small polarization independent phased-array demultiplexers on InP," *IEEE J. Lightwave Technol.*, Vol. 8, pp. 554-6, 1996.

[32] M.Kohtoku, etc., "InP-based 64-channel arrayed waveguide grating with 50 GHz channel spacing and up to −20dB crosstalk," *Electron. Lett.*, Vol. 33, No. 21, pp. 1786-7, Oct. 1997.

[33] J.Sarathy, ect., "Polarization insensitive waveguide grating routers in InP," *IEEE Photon. Technol. Lett.*, Vol. 10, pp. 1763-5, Dec. 1998.

[34] J.B.D.Soole, etc., "Polarization-independent InP arrayed waveguide filter using square cross-section waveguides," *Electron. Lett.*, Vol. 32, No. 4, pp. 323-4, Feb. 1996.

[35] M. Zirngibl, etc., "Demostration of a 15×15 arrayed waveguide demultiplexer on InP," *IEEE Photon. Technol. Lett.*, Vol. 4, pp. 1250-3, Nov. 1992.

[36] M. Zirngibl, etc., "Polarization independent 8×8 waveguide grating multiplexer on InP," *Electron. Lett.*, Vol. 29, No. 2, pp. 201-2, Jan. 1993.

[37] M. Zirngibl, etc., "Polarization compensated waveguide grating router on InP," *Electron. Lett.*, Vol. 31, No. 19, pp. 1662-4, Sept. 1995.

[38] R.Adar, "Broad-band array multiplexers made with silica waveguides on silicon," *IEEE J. Lightwave Technol.*, Vol. 11, pp. 212-9, 1993.

[39] J.C.Chen, etc., "A study of fiber-to-fiber losses in waveguide grating routers," *IEEE J. Lightwave Technol.*, Vol. 15, pp. 1895-9, 1997.

[40] C.D.Lee, "The role of photomask resolution on the performance of arrayed-waveguide graing devices," *IEEE J. Lightwave Technol.*, Vol. 19, pp. 1726-33, 2001.

[41] D.Marcuse, "Bending loss of the asymmetric slab waveguide," *Bell System Tech.*, Vol. 50, pp. 2551-61, Oct. 1971.

[42] K.Takada, etc., "Rayleigh backscattering measurement of 10m long silica-based waveguides," *Electron. Lett.*, Vol. 32, pp. 1665-7, Aug.1996.

[43] M.K.Smit, *Optical Phased Array in Integrated Optics In Silicon-Based Aluminum Oxide*, Ph.D.'s thesis, Delft Univ.of Technol., 1991.

[44] K. Takada, etc., "Measurement of phase error distributions in silica-based arrayed-waveguide-grating multiplexers by using Fourier transform spectroscopy," *Electron. Lett.*, Vol. 30, pp. 1671-72, 1994.

[45] K. Takada, etc., "Optical low coherence method for characterizing silica-based arrayed-waveguide grating multiplexers," *IEEE J. Lightwave Technol.*, Vol. 14, pp. 1677-89, July 1996.

[46] H.Yamada, etc., "10GHz-spaced arrayed waveguide grating multiplexer with phase-error-compensating thin-film heaters," *Electron. Lett.*, Vol. 31, pp. 360-61, 1995.

[47] K. Takada, etc., "Beam-adjustment-free crosstalk reduction in a 10 GHz-spaced arrayed-waveguide grating via photosensitivity under UV laser iiradiation through a metal mask," *Electron. Lett.*, Vol. 36, pp. 60-1, 2000.

[48] O. Ersoy, "One-image-only digital holography," *Optik*, Vol. 53, No. 1, pp. 47-62, 1979.

[49] O. Ersoy, "Construction of point images with the scanning electron microscope: a simple algorithm" *Optik*, Vol. 46, pp. 61-5, 1976.

[50] BeamPROP 4.0 and BeamPROP^{TM} AWG Utility 2.1 User Manuals, Rsoft Inc.

[51] Y. Lu, *Dense Wavelength Division Multiplexing/Demultiplexing by the Method of Irregularly Sampled Zero Crossings*, Ph.D.'s Thesis, School of Electrical and Computer Engineering, Purdue University, 2002.

APPENDICES

APPENDIX A

In AWG, the lightwave is coupled into the arrayed waveguides from the input star coupler and then coupled out of the arrayed waveguides into the output star coupler. Therefore the input and output characteristics of waveguides are of special interest. The radiation and excitation problems of fibers, which are much similar to those of waveguides (especially those fiber-matched silicon-based waveguides), are briefly discussed in this Appendix.

A cylindrical coordinate system (r,ϕ,z) is used to denote the points on a truncated fiber and a spherical coordinate system (R,Θ,Φ) for points outside the truncated fiber as shown in Fig. A.1. In terms of these variables, the Fresnel-Kirchhoff diffraction formula for radiation fields in the Fraunhofer zone or far field zone is given by

$$E_{FF}(R,\Theta,\Phi) \approx jk\frac{e^{-jkR}}{2\pi R}\frac{1+\cos\Theta}{2}\int_S E(r,\phi,0)e^{jkr\sin\Theta\cos(\Phi-\phi)}rdrd\phi \qquad \text{(A.1)}$$

where S is the aperture area on the z=0 plane. “FF” is used to denote the quantities or terms in the far field zone. The fields radiated by a truncated fiber are confined mainly in a small cone in the forward direction. Within this small cone, the inclination factor (1+cosΘ)/2 is approximately 1. Thus Eq. (A.1) can be simplified further as

$$E_{FF}(R,\Theta,\Phi) \approx jk\frac{e^{-jkR}}{2\pi R}\int_S E(r,\phi,0)e^{jkr\sin\Theta\cos(\Phi-\phi)}rdrd\phi \qquad \text{(A.2)}$$

For fiber’s V-parameter near or greater than 2.0, the transverse electric field of the fundamental mode can be accurately approximated by a Gaussian function. Suppose a Gaussian aperture field at z=0 plane is written as

$$E_{GB}(r,\phi,0) = \hat{x}E_0 e^{-r^2/w^2} \qquad \text{(A.3)}$$

where w is the waist radius of the Gaussian beam. From Eq. (A.2) and Eq. (A.3), we can get

$$E_{GB,FF}(R,\Theta,\Phi) = jkE_0\frac{e^{-jkR}}{R}\frac{w^2}{2}e^{-\frac{(kw\sin\theta)^2}{4}} \qquad \text{(A.4)}$$

The effective mode width w_e is defined as the width of a uniform intensity distribution with the same maximum intensity and power content as the modal field:

$$w_e = \frac{\int_0^\infty E(r)^2\, dr}{E(0)^2} = w\sqrt{\frac{\pi}{2}} \tag{A.5}$$

The width of the equivalent Gaussian far field is approximated from Eq. (A.4) as

$$\theta_0 = \frac{2}{kw} = \frac{\lambda}{\pi n_s w} = \frac{\lambda}{n_s w_e \sqrt{2\pi}} \tag{A.6}$$

Now we turn to the excitation problems. Consider waves impinging upon the interface z=0 normally as shown in Fig. A.2. Suppose the medium to the left of the truncated fiber is free space. Thus the incident waves for $z \leq 0$ are given by

$$\begin{aligned} E_{in} &= (e_{in,t} + \hat{z}e_{in,z})e^{-jkz} \\ H_{in} &= (h_{in,t} + \hat{z}h_{in,z})e^{-jkz} \end{aligned} \tag{A.7}$$

A portion of incident waves is reflected in the –z direction:

$$\begin{aligned} E_{rf} &= (e_{rf,t} + \hat{z}e_{rf,z})e^{+jkz} \\ H_{rf} &= (h_{rf,t} + \hat{z}h_{rf,z})e^{+jkz} \end{aligned} \tag{A.8}$$

For weakly guiding fibers, the index difference is very small. Furthermore the core area is much smaller than the cladding area. Thus we expect the reflected field is essentially the same as the waves reflected by a planar boundary separating air and a dielectric medium with an index of refraction n_{cl}. In other words,

$$e_{rf,t} \approx \frac{1-n_{cl}}{1+n_{cl}} e_{in,t} \tag{A.9}$$

We assume that the mode fields profile e_v and h_v and the propagation constant β_v of mode v are known. However, the mode amplitude c_v is to be determined. Let the fields in the step-index fiber launched by the incident waves be the summation of all possible guided modes:

$$\begin{aligned} E_{fb} &= \sum_v c_v (e_{v,t} + \hat{z}e_{v,z})e^{-j\beta_v z} \\ H_{rf} &= \sum_v c_v (h_{v,t} + \hat{z}h_{v,z})e^{-j\beta_v z} \end{aligned} \tag{A.10}$$

To determine c_v, we make use of the continuity of the tangential component of electric and magnetic fields at the truncated fiber surface, and also the orthogonality relation between two guided modes. Then we get the approximated value of c_v by using Eq. (A.9).

$$c_v = \frac{\int_s (e_{in,t} + e_{rf,t}) \times h_{v,t}^* \cdot \hat{z} ds}{\int_s e_{v,t} \times h_{v,t}^* \cdot \hat{z} ds} \approx \frac{2}{1+n_{cl}} \frac{\int_s e_{in,t} \times h_{v,t}^* \cdot \hat{z} ds}{\int_s e_{v,t} \times h_{v,t}^* \cdot \hat{z} ds} \tag{A.11}$$

Once c_v is known, the percentage of power coupled into mode ν is obtained as

$$c_v = \frac{4}{(1+n_{cl})^2} \frac{(\int_s e_{in,t} \times h_{v,t}^* \cdot \hat{z} ds)^2}{(\int_s e_{v,t} \times h_{v,t}^* \cdot \hat{z} ds)(\int_s e_{in,t} \times h_{in,t}^* \cdot \hat{z} ds)} \tag{A.12}$$

We focus on the Gaussian beam excitation problem. Let the input be an x-polarized Gaussian beam with beam waist w_0 at $z=0$:

$$\begin{aligned} e_{in} &= \hat{x} E_{in} e^{-r^2/w_0^2} \\ h_{in} &= \hat{y} \frac{E_{in}}{\eta} e^{-r^2/w_0^2} \end{aligned} \tag{A.13}$$

The modes in weakly guiding step-index fibers are approximated by

$$\begin{aligned} e_{in} &= \hat{x} E_0 e^{-r^2/w_{eff}^2} \\ h_{in} &= \hat{y} \frac{N E_0}{\eta} e^{-r^2/w_{eff}^2} \end{aligned} \tag{A.14}$$

Substituting the above equations into Eq. A.12, we can obtain

$$\eta_{GB} = \frac{4N}{(1+n_{cl})^2} \frac{4 w_0^2 w_{eff}^2}{(w_0^2 + w_{eff}^2)^2} \tag{A.15}$$

Clearly, the launching efficiency depends on the two waist radii, w_0 and w_{eff}. The maximum value appears when they are the same. The integral in the numerator of Eq. (A.12) is usually referred to as the overlap integral and its integrand contains both the exciting field and the excited field.

APPENDIX B

In section 2.3, we propose the nonuniform-sampling zero-crossing method that consists of three steps. In the third step, an appropriate algorithm is needed to calculate the correction value based on Xu(i) to find X(i). We will give the algorithm for calculating the corrections in this appendix [51].

The phase equation is given as

$$k_s r_{ci} + k_c(l_0 + x_i\alpha) + k_s r_{oi} = 2q\pi + \varphi_0$$

We first focus on the simple case that k_s is equal to the wave vector in free space ($2\pi/\lambda$). Then we get

$$r_{ci} + x_i\delta + r_{oi} = q\lambda + \frac{\varphi_0\lambda}{2\pi}, \qquad B = \frac{\varphi_0\lambda}{2\pi}$$

We already have

$$r_{oi} = \sqrt{(x_o - x_i)^2 + {z_o}^2}$$
$$r_{ci} = \sqrt{(x_c - x_i)^2 + {z_c}^2}$$

Now let x_i be a initial guess Xu(i), and $x_i' = x_i + \Delta$ be the corrected x_i value X(i). The goal is to determine the correction value Δ. We can write

$$r_{ci} + x_i\delta + r_{oi} = r_{ci}' + r_{oi}' + x_i'\delta + B$$

Let

$$Xc = x_c - x_i$$
$$Xo = x_o - x_i$$

Then, we expand as

$$r_{oi}' = \sqrt{(x_o - x_i')^2 + {z_o}^2} = \sqrt{(x_o - x_i - \Delta)^2 + {z_o}^2} = \sqrt{{r_{ci}}^2 - 2\Delta Xc + \Delta^2}$$
$$r_{ci}' = \sqrt{(x_c - x_i')^2 + {z_c}^2} = \sqrt{(x_c - x_i - \Delta)^2 + {z_c}^2} = \sqrt{{r_{oi}}^2 - 2\Delta Xo + \Delta^2}$$

So we have

$$r_{ci} + x_i\delta + r_{oi} = r_{ci}' + x_i'\delta + r_{oi}' + B$$

$$(r_{ci}' + r_{oi}')^2 = (r_{ci} - \delta\Delta + r_{oi} - B)^2$$

Let
$$\begin{aligned}LHS &= r_{ci}^{\ 2}-2\Delta X_c+\Delta^2+r_{oi}^{\ 2}-2\Delta X_o+\Delta^2+2\sqrt{\left(r_{oi}^{\ 2}-2\Delta X_o+\Delta^2\right)\left(r_{ci}^{\ 2}-2\Delta X_c+\Delta^2\right)}\\ &= r_{ci}^{\ 2}+r_{oi}^{\ 2}-2\Delta\left(X_c+X_o\right)+2\Delta^2+2\sqrt{\left(r_{oi}^{\ 2}-2\Delta X_o+\Delta^2\right)\left(r_{ci}^{\ 2}-2\Delta X_c+\Delta^2\right)}\end{aligned}$$

and
$$\begin{aligned}RHS &= \left(r_{ci}+r_{oi}-B\right)^2+\left(\delta\Delta\right)^2-2\left(r_{ci}+r_{oi}-B\right)\delta\Delta\\ &= r_{ci}^{\ 2}+r_{oi}^{\ 2}+2r_{ci}r_{oi}+B^2-2B(r_{ci}+r_{oi})+\left(\delta\Delta\right)^2-2\left(r_{ci}+r_{oi}-B\right)\delta\Delta\end{aligned}$$

By choosing LHS=RHS, we have

$$\begin{aligned}&2\sqrt{\left(r_{oi}^{\ 2}-2\Delta X_o+\Delta^2\right)\left(r_{ci}^{\ 2}-2\Delta X_c+\Delta^2\right)}\\ &\quad=2r_{ci}r_{oi}+B^2-2B(r_{ci}+r_{oi})+\left(\delta\Delta\right)^2-2\left(r_{ci}+r_{oi}-B\right)\delta\Delta\end{aligned}$$

Dividing by 2 and squaring both sides, we have

$$\begin{aligned}&\left(r_{oi}^{\ 2}-2\Delta X_o+\Delta^2\right)\left(r_{ci}^{\ 2}-2\Delta X_c+\Delta^2\right)\\ &\quad=\left[r_{ci}r_{oi}+\frac{B^2}{2}-B(rci+r_{oi})+\frac{\left(\delta\Delta\right)^2}{2}-\left(r_{ci}+r_{oi}-B\right)\delta\Delta\right]^2\end{aligned}$$

Let

$$LHS=\Delta^4+\Delta^3\left(-2Xc-2X_o\right)+\Delta^2\left(4X_cX_o+r_{oi}^{\ 2}+r_{ci}^{\ 2}\right)+\Delta\left(-2X_cr_{oi}^{\ 2}-2X_or_{ci}^{\ 2}\right)+r_{oi}^{\ 2}r_{ci}^{\ 2}$$

$$RHS=\left\{\Delta^2\left(\frac{\delta^2}{2}-1\right)+\Delta\left[-\left(r_{ci}+r_{oi}-B\right)\delta+\left(X_c+X_o\right)\right]+r_{ci}r_{oi}+\frac{B^2}{2}-B(r_{ci}+r_{oi})\right\}^2$$

with

$$\begin{aligned}G_1&=\left(\frac{\delta^2}{2}-1\right)\\ G_2&=-\left(r_{ci}+r_{oi}-B\right)\delta+\left(X_c+X_o\right)\\ G_3&=r_{ci}r_{oi}+\frac{B^2}{2}-B(r_{ci}+r_{oi})\end{aligned}$$

We have

$$\begin{aligned}RHS&=\left[\Delta^2G_1+\Delta G_2+G_3\right]^2\\ &=\Delta^4G_1^{\ 2}+\Delta^3\left(2G_1G_2\right)+\Delta^2\left(G_2^{\ 2}+2G_1G_3\right)+\Delta\left(2G_2G_3\right)+G_3^{\ 2}\end{aligned}$$

$$\begin{aligned}&RHS-LHS=0\\ &\Rightarrow\Delta^4\left(G_1^{\ 2}-1\right)+\Delta^3\left(2G_1G_2+2X_c+2X_o\right)+\Delta^2\left(G_2^{\ 2}+2G_1G_3-4X_cX_o-r_{oi}^{\ 2}-r_{ci}^{\ 2}\right)\\ &+\Delta\left(2G_2G_3+2X_cr_{oi}^{\ 2}+2X_or_{ci}^{\ 2}\right)+G_3^{\ 2}-r_{oi}^{\ 2}r_{ci}^{\ 2}\end{aligned}$$

So we can write

$$\Delta^4 C_4 + \Delta^3 C_3 + \Delta^2 C_2 + \Delta C_1 + C_0 = 0$$

where

$$\begin{aligned}
C_4 &= G_1^{\,2} - 1 \\
C_3 &= 2G_1 G_2 + 2X_c + 2X_o \\
C_2 &= G_2^{\,2} + 2G_1 G_3 - 4X_c X_o - r_{oi}^{\,2} - r_{ci}^{\,2} \\
C_1 &= 2G_2 G_3 + 2X_c r_{oi}^{\,2} + 2X_o r_{ci}^{\,2} \\
C_0 &= G_3^{\,2} - r_{oi}^{\,2} r_{ci}^{\,2}
\end{aligned}$$

The Newtom-Ralfton numerical algorithm is employed to solve this fourth order polynomial equation based on the above coefficients. The solution is exactly the correction to be added upon the initial guess Xu(i) to get X(i), thus, the correct locations for zero-crossings are found. The locations of the zero-crossing sampling points determine the positions of the arrayed waveguide apertures on the aperture plane.

For taking into account $k_s = \frac{2\pi}{\lambda} n_s$, we just make some slight changes to the equations and thus the coefficients of the fourth order polynomial, which is especially important in generating the data files for the BeamPROP utility.

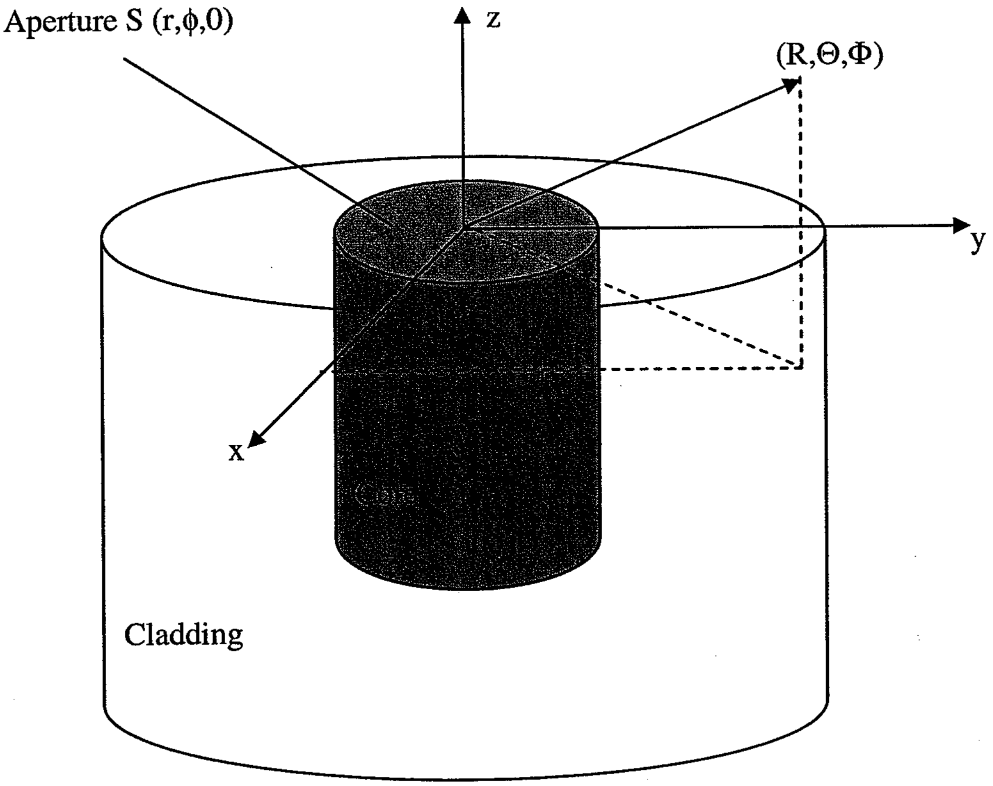

Fig. A.1. A truncated circular core fiber

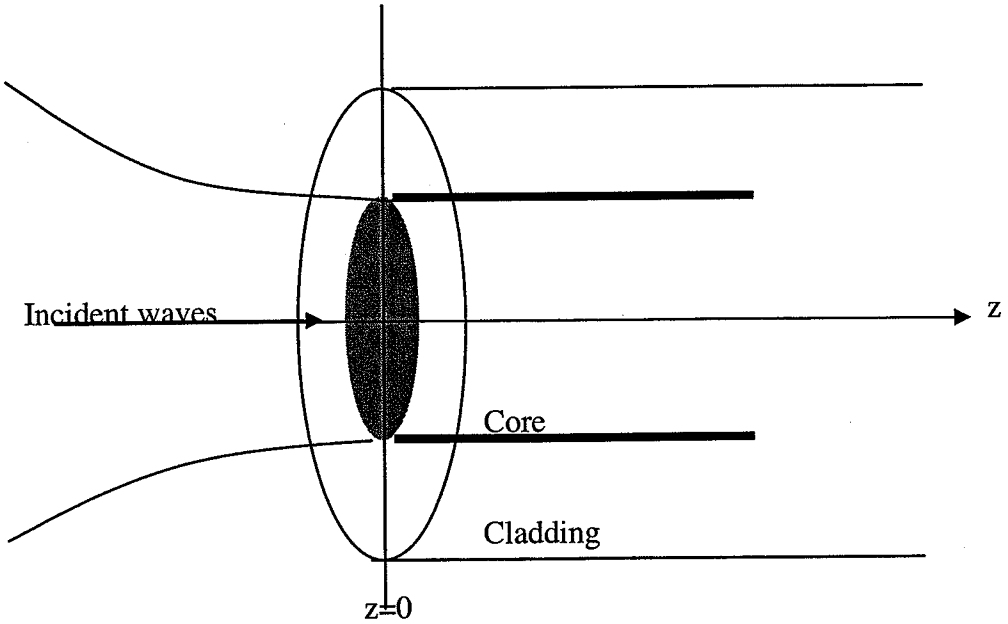

Fig. A.2. Waves incident normally upon a truncated fiber